Imaging Applications from a Laser Wakefield Accelerator

by

David Reboredo Gil

Thesis submitted for the degree of

Doctor of Philosophy in Physics

Physics Department, University of Strathclyde

Supervisors:

Prof. Dino A. Jaroszynski

Dr. Silvia Cipiccia

Signed: David Reboredo Gil

Date: 01/03/2018

Abstract

Laser-plasma wakefield acceleration (LWFA) is a promising technology that is attracting the attention of the scientific community. It is a new acceleration concept where electrons can be accelerated to very high energy (~150 MeV) in a very short distance (mm scale). Electrons “surf” plasma waves excited by the passage of a high power laser (~10^{18} Wcm^{-2}) through plasma.

Electrons in the LWFA can undergo transverse oscillation and emit synchrotron-like X-ray radiation, commonly known as betatron radiation, in a narrow cone along the laser propagation axis.

The properties of both the electrons and the X-rays produced by the LWFA make them excellent candidates for a wide range of applications. In this thesis, both betatron X-ray and bremsstrahlung sources from the ALPHA-X laboratory are used to carry out both conventional imaging and X-ray phase-contrast imaging experiments to explore the feasibility of real-world applications.

The characterisation of the betatron X-ray radiation produced by the LWFA in the ALPHA-X laboratory is presented. In the last Chapter, a brief discussion of the potential of LWFA technology for clinical applications is presented.

Acknowledgements

This work would have not been possible without the help and support of many people:

- My supervisor, Prof Dino Jaroszynski, for giving me the opportunity of working in this exciting field as well as giving me the necessary support and advice throughout these PhD years.
- My PhD examinors, Prof Marco Borghesi and Prof Erling Riis for helping me to improve this manuscript.
- Dr Silvia Cipiccia, for her advice and support inside the laboratory and more importantly outside the laboratory. For all the skype calls to give me advice when necessary (even late in the evening) and for her huge patience when working with me (a very huge one). Thank you Doctora.
- Dr Gregor Welsh, for his help and advice with the laser and the technical aspects of the experiments, for having the patience to answer the phone late in the evenings when we were having problems at the lab and more importantly for showing me how important organisation is at research. Thanks a lot Gregor.
- Dr Enrico Brunetti, for his technical advice inside the lab, for his brilliant analysis and programming skills and more importantly for his common sense. Thank you very much Enrico.
- David Clark and Tom McCanny for the technical support.
- Dr Dima Maneuski for the help and advice with the tomographies.
- Dr Maria Pia Anania for her help and sympathy in Frascati.
- My group colleagues: Gregory Vieux, Mark Wiggins, Adam Noble, Gaurav Raj, Ranaul Islam, Constantine Aniculaesei, Grace Manahan, David Grant, Yevgen Kravets, John Farmer, Panos Lepipas, Martin Mitchell, Cristian Ciocarlan, Anna Subiel, Bernhard Ersfeld, Sam Yoffe, Graeme Mckendrick for all the good moments shared during these years.

- Peter Grant and Paul Farrell for all the great moments we shared in Glasgow at the Black Bull. Special thanks to Fernando Martinez for his emotion.
- Amelia Beveridge for making me smile on the worst days of the PhD.
- My family, specially my mother. Please forgive me if I have not been there when I should have.
- My partner Ana Maria Botella Ivars, for supporting me in all the bad moments. If this work is considered to deserve the PhD award all the merit will correspond to Ana. Gracias rula.
- To Scotland in general, where I have never felt a foreign.

Thanks very much to you all.

Role of the author

The idea of using the betatron and bremsstrahlung X-rays produced by a laser wakefield accelerator for imaging applications was proposed by Prof. Dino Jaroszynski. In Chapter 3 the FLUENT simulations have been performed by Dr Enrico Brunetti. The author was responsible for planning, setting up and performing the experiments presented in Chapters 4 and 5 with the help of Dr Silvia Cipiccia, Dr Gregor Welsh, Dr Enrico Brunetti, Dr Anna Subiel, Mr Peter Grant, Mr David Grant, Mr Panos Lepipas and Mr Graeme Mckendrick. The detectors used in this work have been calibrated by the author, with the help of Dr Silvia Cipiccia. The analysis of the results has been undertaken by the author with the help of Dr Silvia Cipiccia, Dr Enrico Brunetti and Dr Dima Maneuski. The FLUKA Monte Carlo simulations presented in Chapter 4 have been performed by the author with the help of Dr Silvia Cipiccia who incorporated a refraction model based on Snell's law into the FLUKA code. The MAD-X simulations for electron beam transport presented in Chapter 5 have been performed by Dr Enrico Brunetti. Technical and engineering support during the experiments have been provided by Mr David Clark and Mr Tom McCanny.

List of publications

During the course of this thesis the author has contributed to the following publications:

1. A. Subiel, V. Moskvin, G. H. Welsh, S. Cipiccia, D. Reboredo, C. DesRosiers and D. A. Jaroszynski, "*Challenges of dosimetry of ultra-short pulsed very high energy electron beams*", Phy. Med. (2017).
2. G. Vieux, S. Cipiccia, D. W. Grant, N. Lemos, P. Grant, C. Ciocarlan, B. Ersfeld, M. S. Hur, P. Lepipas, G. Manahan, G. Raj, D. Reboredo Gil, A. Subiel, G. H. Welsh, S. M. Wiggins, S. R. Yoffe, J. P. Farmer, C. Aniculaesei, E. Brunetti, X. Yang, R. Heathcote, G. Nersisyan, C. L. S. Lewis, A. Pukhov, J. M. Dias and D. A. Jaroszynski, "*An ultra-high gain and efficient amplifier based on Raman amplification in plasma", Sci. Rep. 7,* (2017).
3. E. Brunetti, X. Yang, F. Y. Li, D. Reboredo Gil, G. H. Welsh, S. Cipiccia, B. Ersfeld, D. W. Grant, P. A. Grant, M. R. Islam, M. Shahzad, M. P. Tooley, G. Vieux, S. M. Wiggins, Z. M. Sheng and D. A. Jaroszynski, "*Wide-angle electron beams from laser-wakefield accelerators"*, Proc. SPIE 10240, Laser Acceleration of Electrons, Protons and Ions IV, (2017).
4. X. Yang, E. Brunetti, D. Reboredo Gil, G. H. Welsh, F.Y. Li, S. Cipiccia, B. Ersfeld, D. W. Grant, P. A. Grant, M. R. Islam, M. P. Tooley, G. Vieux, S. M. Wiggins, Z. M. Sheng, and D. A. Jaroszynski, *"Three beam acceleration from a laser-plasma wakefield accelerator and the energy apportioning question"*, Sci. Rep. 7, 43910 (2017).
5. D. A. Jaroszynski, B. Ersfeld, M. R. Islam, E. Brunetti, R. P. Shanks, P. A. Grant, M. P. Tooley, D. W. Grant, D. Reboredo Gil, P. Lepipas, G. McKendrick, S. Cipiccia, S. M. Wiggins, G. H.Welsh, G. Vieux, S. Chen, C. Aniculaesei, G. G. Manahan, M.-P. Anania, A. Noble, S. R. Yoffe, G. Raj, A. Subiel, X. Yang, Z. M. Sheng, B. Hidding, R. C. Issac, M.-H. Cho, and M. S. Hur, *"Coherent radiation sources based on laser driven plasma waves"*, Proc. 40th Int. Conf. IRMMW-THz, H2E-1 (2015).

6. D. Reboredo, S. Cipiccia, P. A. Grant, G. H. Welsh, D. W. Grant, G. McKendrick, A. Subiel, D. Maneuski, S. M. Wiggins, and D. A. Jaroszynski, *"Phase-contrast imaging using radiation sources based on laser-plasma wakefield accelerators: state of the art and future development"*, Proc. SPIE 9412, 94120J (2015).
7. S. Cipiccia, M. R. Islam, B. Ersfeld, G. H. Welsh, E. Brunetti, G. Vieux, X. Yang, S. M. Wiggins, P. Grant, D. Reboredo Gil, D. W. Grant, R. P. Shanks, R. C. Issac, M. P. Anania, D. Maneuski, R. Montgomery, G. Smith, M. Hoek, D. Hamilton, D. Symes, P. P Rajeev, V. O'Shea, J. M. Dias, N. R. C. Lemos, and D. A. Jaroszynski, *"Gamma-ray production from resonant betatron oscillations of accelerated electrons in a plasma wake"*, Proc. SPIE 9512, 95121A (2015).
8. S. Cipiccia, D. Reboredo, F. A. Vittoria, G. H. Welsh, P. Grant, D. W. Grant, E. Brunetti, S. M. Wiggins, A. Olivo, and D. A. Jaroszynski, *"Laser-wakefield accelerators for medical phase contrast imaging: Monte Carlo simulations and experimental studies"*, Proc. SPIE 9514, 951417 (2015).
9. S. M. Wiggins, M. P. Anania, G. H. Welsh, E. Brunetti, S. Cipiccia, P. A. Grant, D. Reboredo, G. G. Manahan, D. W. Grant, and D. A. Jaroszynski, *"Undulator radiation driven by laser-wakefield accelerator electron beams"*, Proc. SPIE 9509, 95090K (2015).
10. A. Subiel, V. Moskvin, G. H. Welsh, S. Cipiccia, D. Reboredo Gil, P. Evans, M. Partridge, C. DesRosiers, M. P. Anania, A. Cianchi, A. Mostacci, E. Chiadroni, D. Di Giovenale, F. Villa, R. Pompili, M. Ferrario, M. Belleveglia, G. Di Pirro, G. Gatti, C. Vaccarezza, B. Seitz, R. C. Isaac, E. Brunetti, S. M. Wiggins, B. Ersfeld, M. R. Islam, A. Sorensen, M. Boyd, and D. A. Jaroszynski, *"Dosimetry of Very High Energy Electrons (VHEE) for radiotherapy applications"*, Phys. Med. Biol. 59, 5811 (2014).

Table of contents

Chapter 6: Summary of results and outlook

List of tables

List of Figures

Chapter 1: Introduction

1.1 X-rays as a tool for imaging

X-rays are a form of very short wavelength electromagnetic radiation, with wavelengths ranging from 0.01 to 10 nm. The short wavelength of X-rays allows them to penetrate materials that are opaque to visible light. Because of this property X-rays have been used as a powerful imaging tool since Röntgen's time, when he discovered them in 1895 [1]. Moreover, when the wavelength is close to interatomic distances in crystals, they acts as diffraction gratings, which makes them suitable for X-ray crystallography. This has enabled the investigation of the atomic structure of matter (Figure 1.2), as first demonstrated by Laue and collaborators in 1911 [2].

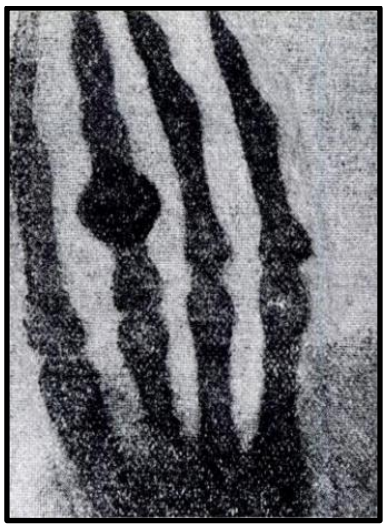

Figure 1.1. First radiography of Röntgen's wife hand. From [1].

Following their discovery, there has been a rapid growth in using X-rays in security, industrial and medical applications around the world. To give a few examples: in the 1960s X-ray screening machines were used for the first time together with metal detectors at airports for baggage security inspection. Since then, these devices have been installed gradually in virtually all airports around the world, and in many government buildings.

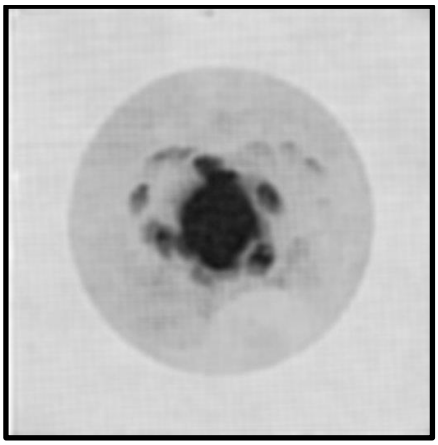

Figure 1.2. First diffraction pattern by Laue and collaborators in 1911. From [2].

X-rays and gamma rays are commonly used in industrial radiography to investigate the current status of equipment and structures, and have recently been proposed for nuclear waste inspection. They have become an indispensable tool for quality control in modern engineering. They are also used as a non-destructive method for examining the volume of a specimen to observe changes in thickness, defects or structure details that are impossible to see by eye.

The medical community has recognized the potential of X-rays for both diagnosis and therapy. In the years following Röntgen's discovery, several applications have shown the utility of X-rays for imaging the inside of the human body, without dissection, to observe internal organs and tissues. Over the years, several important improvements in X-ray techniques have been made, mainly through development of higher sensitivity recording films, modern electronic X-ray detectors and fast computers, and effective software for analysis.

The modern medical imaging era began in the 1970s with the development of the Computerised Axial Tomograph device (CAT scanner), e.g.:

- The image became digital and could be easily modified and analysed,
- An unprecedented improvement in the sensitivity to tissue density differences and

- The method provided cross-sectional views of the body, eventually providing 3D reconstruction of internal organs and tissues.

Table1.1. Some diagnostic imaging advances in the last century.

Year	Technology advance	Pioneer
1895	Discovery of X-rays	W. C. Röntgen
1896	Calcium tungstate screens	T. A. Edison
1896	Discovery of radioactivity	H. Becquerel
1913	Hot-cathode X-ray tube	W. D. Coolidge
1915	Bucky Potter grid	G. P. Bucky, H. E. Potter
1934	Conventional tomography	A. Vallebona, G. Z. DesPlantes
1948	Westinghouse image intensifier	J. W. Coltman
1951	Rectilinear scanner	B. Cassen
1951	Bistable US	G. Ludwig, J. Wild, D. Howry
1958	Scintillation camera	H. Anger
1962	Emission reconstruction tomography	D. Kuhl
1962	Gray-scale US	G. Kosoff
1972	CT	G. N. Hounsfield
1975	Positron emission tomography or PET	M. Ter-Pogossian
1976	Single photon emission CT or SPECT	J. Keyes

The milestones of X-ray discovery and its development as a tool for imaging are summarized in Table 1.1.

When an X-ray photon interacts with a sample, it can be absorbed, scattered in one or more interactions, or pass through the sample without interaction. In medical imaging applications, the energy of the X-rays used is normally between 10 and 200 keV. Three interaction processes of X-ray photon transport in tissues are particularly important: coherent Rayleigh scattering, photoelectric effect and incoherent Compton scattering. Nowadays, conventional attenuation-based methods dominate the clinical use of X-rays for medical tissue imaging.

The development of new compact synchrotron-like X-ray sources is having a huge impact in the X-ray imaging field. The high brightness, high transverse coherence and short duration pulses of these sources have the potential to develop new X-ray imaging techniques, based not only on the absorption process, such as phase contrast imaging, which may change the way clinical imaging is done.

1.2 Laser wakefield acceleration: a novel acceleration concept for industrial and medical applications

Conventional accelerators are based on radiofrequency (RF) technology, where charged particles are accelerated by the electric fields generated in conducting cavities. However, this technology is limited to a maximum field of around 100 MV/m by electrical breakdown, which makes conventional accelerators large and expensive devices.

However, plasma is a promising accelerating medium because it is already broken down and can support accelerating fields three orders of magnitude greater than in RF cavities, which reduces the size of the accelerator by a factor of more than 1000. This means that it is, in principle, possible to reduce kilometre size accelerator facilities to meter size devices. This makes possible a reduction in the size of synchrotrons from hundreds of meters to centimetres.

Figure 1.3. Left hand side: 3 km picture of the Stanford linear accelerator (SLAC) located in California, USA (from: www.flickr.com/photos/slaclab/28944688233/in/album-72157668567210712, ©SLAC National Accelerator Laboratory, 11/05/2009. Last accessed 31/07/2018). Right hand side: 4 cm, ALPHA-X 1 GeV plasma accelerator (from: silis.phys.strath.ac.uk, ©University of Strathclyde, 05/04/2010. Last accessed 31/07/2018).

In 1979, Tajima and Dawson [3] suggested that laser-driven plasma waves could be used to accelerate particles to high energies. They suggested the idea of using an intense laser pulse that is shorter than the plasma oscillation

period, to excite plasma waves. This scheme is known as the laser wakefield accelerator.

At that time, ultrashort intense laser pulses were not available. However, in 1985 Mourou and Strickland showed that it is possible to produce both high power and ultrashort pulses from laser systems based on chirped-pulse amplification (CPA) [4, 5].

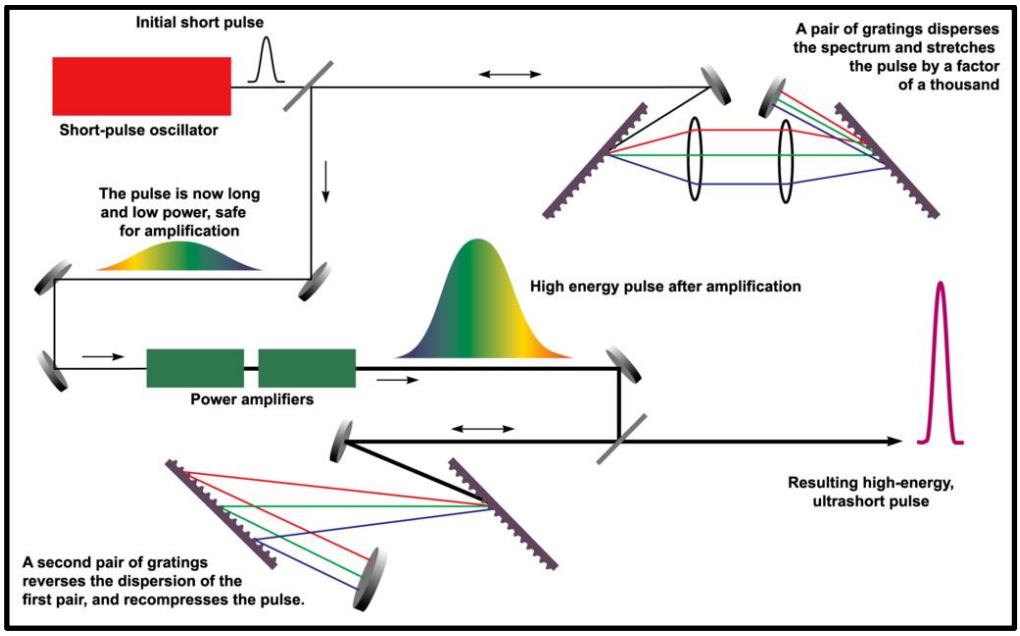

Figure 1.4. Schematic of CPA [6]. The laser pulse is stretched before being amplified by the power amplifiers. After amplification, the pulse is compressed to its original pulse length.

In CPA, an ultrashort laser pulse is stretched in time before amplification. Because the intensity of the stretched pulse is relatively low it can be safely amplified by the gain medium without damaging it and then finally compressed to its original pulse length (Figure 1.4).

The first proof-of-principle experiment to demonstrate the laser-plasma wakefield accelerator was performed in 1994 at Osaka University [7], where electrons were accelerated by only a few MeV. The first experiments demonstrating the production of a quasi mono-energetic electron beam in the range of 100 MeV were reported simultaneously in 2004 [8-10] by three groups, one in a project (ALPHA-X) led by the University of Strathclyde. In these experiments, laser pulses based on Ti:sapphire high power CPA laser

systems with energy between 0.5–1 J and pulse durations between 33–55 fs were focused onto helium supersonic gas jets to produce fully ionised plasma with densities of $n_e \approx 10^{19}$ cm^{-3}. In these experiments, electron beams with much narrower energy spread than previous experiments were observed, which showed for the first time that laser wakefield acceleration was able to produce quasi mono-energetic electron beams.

Soon after, Rousse et al., [11] showed that a synchrotron-like source is embedded in the LWFA, which emits bright X-ray radiation in the forward direction. While electrons are accelerated in the forward direction, their initial transverse momentum leads to transverse (betatron) oscillations, similar to that in a wiggler. These betatron oscillations produce broadband radiation at very short wavelengths [12, 13]. Their small source size (a few microns) guarantees the high level of spatial coherence needed for X-ray phase contrast imaging (XPCi), making it a perfect candidate for imaging applications.

The unique properties of both electron (high energy, high charge, low emittance) and X-ray beam (small source size, high energy, high flux) sources from a laser wakefield accelerator can be used in a wide range of applications. Some examples are the following:

- Very high energy electron radiotherapy [14, 15].
- Radioisotope production for PET and SPECT scans [16].
- Gamma radiography [17] for non-destructive inspection or material diagnosis.
- Ultrafast radiolysis studies in biology and chemistry [18].
- Both absorption [19] and phase contrast imaging [20] for medical and security applications.
- X-ray diffraction for crystal and large molecule structure characterisation.

LWFA can drive compact sources of radiation, and are a suitable candidate for driving a free-electron laser (FEL) [21]. In a FEL, positive feedback between an electron bunch and the radiation it generates as it passes through an undulator causes exponential growth of the radiation intensity via ‘micro-

bunching' of the electrons. In this case the peak brilliance is expected to jump by many orders of magnitude to 10^{32}-10^{33} photons/s/mrad^2/mm^2/0.1%BW. These are the standard units for the brilliance and it takes into account the spectral purity of the source. For a fixed photon flux, a narrow-band source will result in a higher brilliance.

Undulator radiation, both in the visible [21] and soft X-ray [22] spectral range, has been demonstrated by passing electron beams produced by a LWFA through magnetic undulators.

In the long term, and with further improvements in electron beam quality, plasma accelerators may provide an alternative to conventional accelerators in particle colliders.

The development of laser-driven plasma accelerators has been historically linked to the development of high power laser systems, which will continue in the future. Electron energies of around 1.0 GeV have been demonstrated several times and recently electron beams of 4.2 GeV with relative low energy spread have been produced [23]. The next challenge in the development of LWFAs will be to break the barrier of 10 GeV for which new laser amplification schemes may be required.

Raman amplification is a promising scheme for laser amplification, which could potentially replace current laser amplifiers in the future. In this scheme, two counter-propagating laser beams interact in plasma via stimulated Raman backscattering and a fraction of the energy of one laser beam (pump laser) is transferred to the other beam (probe beam). Several groups around the world are working on this technique. The University of Strathclyde team has recently demonstrated the potential of chirped pulse Raman amplification [24].

Another promising technique is optical parametric chirped pulse amplification (OPCPA). In this technique, optical parametric amplifiers are used instead of laser amplifiers [25]. Although further development is clearly still required, high power OPCPA laser systems have been developed and deliver laser pulses

with peak powers up to 16 TW [26]. A 560 TW laser system has also been developed delivering one shot every 30 s.

1.3 Thesis objectives and structure

This thesis explores the feasibility of using radiation sources from a LWFA (*i.e.* betatron X-rays and bremsstrahlung) for both phase-contrast and absorption imaging applications, focusing on the feasibility of the LWFA for tomography and 3D reconstruction for medical and industrial applications. FLUKA Monte Carlo simulations to investigate the requirements of a betatron source for real world applications such as imaging of micro-cracks in bone are presented.

The second Chapter discusses the theory behind LWFA, including laser-plasma interactions and the ponderomotive force. Limitations and LWFA configurations are described together with an introduction to both the bubble regime and betatron motion.

The third Chapter describes the experimental set up on the ALPHA-X (Advanced Laser-Plasma High Energy Accelerators Towards X-rays) particle accelerator at the University of Strathclyde. The laser system, plasma accelerator, ALPHA-X beam line and diagnostics used for this work are also described.

Chapter four presents the characterisation of the ALPHA-X betatron X-ray source as well as XPCi experiments using the ALPHA-X betatron X-rays. The X-ray detectors used for these experiments are also described. Microscopy and tomographic studies using the ALPHA-X betatron source are discussed and presented. In addition, an introduction to XPCi including basic concepts of phase-contrast imaging together with the most common XPCi configurations are presented.

The fifth Chapter gives a brief overview of bremsstrahlung. 3D reconstruction using a bremsstrahlung source is presented together with Monte Carlo simulations on the properties of the bremsstrahlung source.

In the sixth and last Chapter, results are discussed and future perspectives for LWFA as a compact source for imaging applications are underlined with a focus on clinical applications.

Chapter references:

1. Roentgen, W.C., *On a new kind of rays.* Nature, 1896(53): p. 274-276.
2. Laue, M., *Eine quantitative Prüfung der Theorie für die Interferenzerscheinungen bei Röntgenstrahlen.* Annalen der Physik, 1913. **346**(10): p. 989-1002.
3. Tajima, T. and J. Dawson, *Laser electron accelerator.* Physical Review Letters, 1979. **43**(4): p. 267.
4. Strickland, D. and G. Mourou, *Compression of amplified chirped optical pulses.* Optics Communications, 1985. **55**(6): p. 447-449.
5. Mourou, G.A., C.P. Barry, and M.D. Perry, *Ultrahigh-Intensity Lasers: Physics of the Extreme on a Tabletop.* Physics today, 2008. **51**(1): p. 22-28.
6. https://str.llnl.gov/str/pdfs/
7. Nakajima, K., et al., *A proof-of-principle experiment of laser wakefield acceleration.* Physica Scripta, 1994. **1994**(T52): p. 61.
8. Geddes, C., et al., *High-quality electron beams from a laser wakefield accelerator using plasma-channel guiding.* Nature, 2004. **431**(7008): p. 538-541.
9. Mangles, S., et al., *Monoenergetic beams of relativistic electrons from intense laser–plasma interactions.* Nature, 2004. **431**(7008): p. 535-538.
10. Faure, J., et al., *A laser–plasma accelerator producing monoenergetic electron beams.* Nature, 2004. **431**(7008): p. 541-544.
11. Rousse, A., et al., *Production of a keV X-Ray Beam from Synchrotron Radiation in Relativistic Laser-Plasma Interaction.* Physical Review Letters, 2004. **93**(13): p. 135005.

12. Kneip, S., et al., *Bright spatially coherent synchrotron X-rays from a table-top source.* Nature Physics, 2010. **6**(12): p. 980-983.
13. Cipiccia, S., et al., *Gamma-rays from harmonically resonant betatron oscillations in a plasma wake.* Nature Physics, 2011. **7**(11): p. 867-871.
14. Nakajima, K., et al., *Laser-Driven Very High Energy Electron/Photon Beam Radiation Therapy in Conjunction with a Robotic System.* Applied Sciences, 2015. **5**(1): p. 1.
15. Subiel, A., et al., *Dosimetry of very high energy electrons (VHEE) for radiotherapy applications: using radiochromic film measurements and Monte Carlo simulations.* Physics in Medicine and Biology, 2014. **59**(19): p. 5811.
16. Reed, S., et al., *Efficient initiation of photonuclear reactions using quasimonoenergetic electron beams from laser wakefield acceleration.* Journal of Applied Physics, 2007. **102**(7): p. 073103.
17. Ben-Ismaïl, A., et al., *Compact and high-quality gamma-ray source applied to 10 µm-range resolution radiography.* Applied Physics Letters, 2011. **98**(26): p. 264101.
18. Malka, V., J. Faure, and Y.A. Gauduel, *Ultra-short electron beams based spatio-temporal radiation biology and radiotherapy.* Mutation Research/Reviews in Mutation Research, 2010. **704**(1): p. 142-151.
19. Cipiccia, S., et al., *A tuneable ultra-compact high-power, ultra-short pulsed, bright gamma-ray source based on bremsstrahlung radiation from laser-plasma accelerated electrons.* Journal of Applied Physics, 2012. **111**(6): p. 063302.
20. Kneip, S., et al., *X-ray phase contrast imaging of biological specimens with femtosecond pulses of betatron radiation from a compact laser plasma wakefield accelerator.* Applied Physics Letters, 2011. **99**(9): p. 093701.
21. Schlenvoigt, H. P., et al., *A compact synchrotron radiation source driven by a laser-plasma wakefield accelerator.* Nature Physics, 2008. **4**(2): p. 130-133.

22. Fuchs, M., et al., *Laser-driven soft-X-ray undulator source.* Nature Physics, 2009. **5**(11): p. 826-829.
23. Leemans, W., et al., *Multi-GeV electron beams from capillary-discharge-guided subpetawatt laser pulses in the self-trapping regime.* Physical Review Letters, 2014. **113**(24): p. 245002.
24. Vieux, G., et al., *Chirped pulse Raman amplification in plasma.* New Journal of Physics, 2011. **13**(6): p. 063042.
25. Ross, I.N., et al., *The prospects for ultrashort pulse duration and ultrahigh intensity using optical parametric chirped pulse amplifiers.* Optics Communications, 1997. **144**(1): p. 125-133.
26. Herrmann, D., et al., *Generation of sub-three-cycle, 16 TW light pulses by using noncollinear optical parametric chirped-pulse amplification.* Optics Letters, 2009. **34**(16): p. 2459-2461.

Chapter 2: Laser-plasma acceleration basic concepts

2.1 Introduction

As mentioned in Chapter one, laser-driven particle accelerators were first proposed in 1979 by Tajima and Dawson [1]. Dawson also contributed to the development of the plasma beat-wave accelerator, the laser wakefield accelerator and the photon accelerator [2, 3]. Moreover, he was one of the first to develop particle-in-cell (PIC) codes that are currently used world-wide in laser plasma acceleration research [4-6].

The next step in this field occurred with the development of chirped pulse amplification (CPA) by Gerard Mourou and collaborators [7-10]. This has enabled the widespread use of high power and ultrashort laser pulses from compact solid-state laser systems that are capable of delivering intensities of $10^{18}\ \mathrm{Wcm^{-2}}$.

Prior to 2004, several groups reported [11-13] laser-plasma electron accelerators with energies up to 100 MeV and 1 nC charge, and acceleration gradients of 100 GV/m. These electron beams had a Maxwellian energy distribution with an effective temperature of 10 MeV and a tail reaching up to 100 MeV.

The quality of laser-plasma accelerated electrons advanced a step further in 2004. Three groups simultaneously in France, UK (led by the University of Strathclyde as part of the ALPHA-X project) and the US [14-16] produced high charge (100 pC) and high energy (100 MeV) electron bunches with low energy spread (few percent) and low divergence (few mrads). This improvement in the quality of the electron beam is mainly due to the improvement of laser technology and understanding of the physics of wakefield accelerators.

Although the accelerator community was initially sceptical about plasma acceleration, nowadays it is considered as the main alternative to conventional

accelerators. Petawatt lasers are becoming more and more widely available (CLPU, Berkeley, CLF), which will allow to take this field a step further. CERN is also developing the AWAKE [17] project, which is a proof-of-principle experiment where, for the first time a 400 GeV, a proton beam is used to drive a wakefield and accelerate electrons to GeV energies in 10 meters. The ELI project is also remarkable. It aims to build several petawatt-class lasers, including several 10 PW lasers for high-field studies, explore potential applications and develop new technologies.

The experiments reported in this thesis have been carried out with the laser-plasma wakefield accelerator (LWFA) at the University of Strathclyde.

Understanding the physics underlying this field is important in order to achieve high quality parameters of the accelerated electron beams.

This Chapter gives an overview of the principles and theory behind laser-plasma acceleration as well as betatron oscillations because the betatron X-rays are used in experiments performed for this thesis.

2.2 Laser-plasma interactions

Bound electrons in an atom oscillate at the same frequency as that of a low intensity infrared laser field. If the work done by the laser field on an electron, eEr_0, (where e is the electron charge and E the electric field of the laser) over a distance equal to the Bohr radius, r_0, is close to the Coulomb binding energy, (e^2/r_0), then the electron response becomes strongly non-linear. When the intensity of the laser is increased, electrons can be removed from the atom by either tunnelling or multiphoton ionisation. Plasma electrons will still oscillate at the laser frequency, but for laser intensities beyond $10^{17} - 10^{18}$ $\mathrm{Wcm^{-2}}$, for ≈1 μm wavelength, their quiver velocities v will approach the speed of light c and the term $(v \times B)$ in the Lorentz force equation can no longer be neglected:

$$\vec{F} = \frac{d(\gamma m\vec{v})}{dt} = e\vec{E} + e\left(\frac{\vec{v}}{c} \times \vec{B}\right), \tag{2.1}$$

where γ is the Lorentz factor and B the laser magnetic field.

An important parameter in the physics of laser-plasma interactions is the laser strength parameter a_0, defined as the peak amplitude of the normalised vector potential of the laser field [18]:

$$\vec{a} = \frac{e\vec{A}}{m_e c^2}, \tag{2.2}$$

where $\vec{A}$ is the vector potential and m_e the electron mass. The laser strength parameter is related to the peak laser intensity I_0 and power by [18]:

$$P = \frac{\pi r_0^2 I_0}{2}, \tag{2.3}$$

$$I_0 = \left(\frac{\pi c}{2}\right)\left(\frac{m_e c^2 a_0}{e\lambda}\right)^2, \tag{2.4}$$

which gives [18]:

$$a_0^2 \cong 7.3 \times 10^{-19}[\lambda(\mu\mathrm{m})]^2 I_0 \left(\frac{\mathrm{W}}{\mathrm{cm}^2}\right), \tag{2.5}$$

where λ is the wavelength of the laser light and r_0 the laser spot radius at focus.

When $a_0 \cong 1$ the electron mass m_e begins to change significantly compared to the electron rest mass. This condition is satisfied for a 1 *μm* laser when the intensity is greater than $10^{18}\ \mathrm{Wcm}^{-2}$.

At low laser intensity, the solution to the Lorentz force equation gives the electron motion described by an oscillation at the laser frequency along a straight line parallel to the polarisation vector. For higher intensities, the solution to the Lorentz equation gives an average drift in the direction of laser propagation $\hat{k}$ direction and a figure-of-eight shape in the plane defined by the

polarisation vector and $\hat{k}$, as observed in a frame that moves with the same drift velocity.

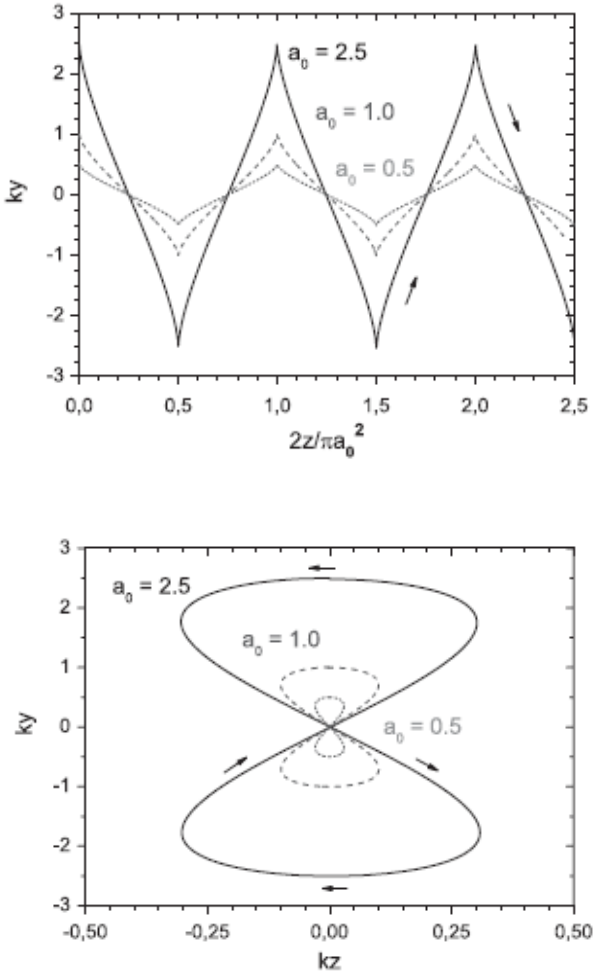

Figure 2.1. Top: Oscillation of a free electron in a linearly polarised plane wave as observed in the laboratory frame for different laser strength parameters. Bottom: Motion of a free electron in a linearly polarised plane wave as observed in the co-moving average frame for different laser strength parameters. Here the classic figure-of-eight motion is observed. The arrows indicate the direction of the oscillation motion. From [18].

The drift motion is due to the fact that the term $v \times B \propto E^2 \hat{k}$. As the laser strength parameter increases $a_0^2 \gg 1$, the longitudinal drift motion, which is proportional to a_0^2, starts to dominate the transverse motion, proportional to a_0.

Because this motion is periodic, electrons that follow a figure-of-eight motion pattern radiate photons with a rich harmonic content, with each harmonic having its own angular distribution pattern. This is called nonlinear Thomson scattering or relativistic Thomson scattering [19].

2.3 Plasma optics

2.3.1 Relativistic self-focusing

For high laser intensities the relativistic change in the electron mass modifies the plasma frequency:

$$\omega_p = \left(\frac{4\pi n_e e^2}{\gamma m_0}\right)^{\frac{1}{2}}, \tag{2.6}$$

where n_e is the electron plasma density and γ is the relativistic Lorentz factor given by:

$$\gamma = \frac{1}{\sqrt{1-\frac{v^2}{c^2}}}. \tag{2.7}$$

The refractive index of the plasma is therefore modified, which changes the dielectric properties of the medium. In this case, the refractive index for radiation with frequency ω will be:

$$n = \left[1-\left(\frac{\omega_p}{\omega}\right)^2\right]^{\frac{1}{2}}. \tag{2.8}$$

For a laser beam with a transverse intensity profile peaking on axis, such as the one shown in Figure 2.2, for $\gamma(0) > \gamma(r)$, the refractive index will have a maximum on axis.

This will produce optical guiding of the laser light by curving inwards the wave-front as well as causing the laser to converge. Due to the fact that the laser phase velocity $v_\emptyset$ depends on the refractive index, $v_\emptyset = c/n$, it will therefore depend on the laser intensity. Local variations in the phase velocity will modify the shape of the laser pulse and, as a consequence, cause spatial and temporal profile variations of the laser pulse intensity.

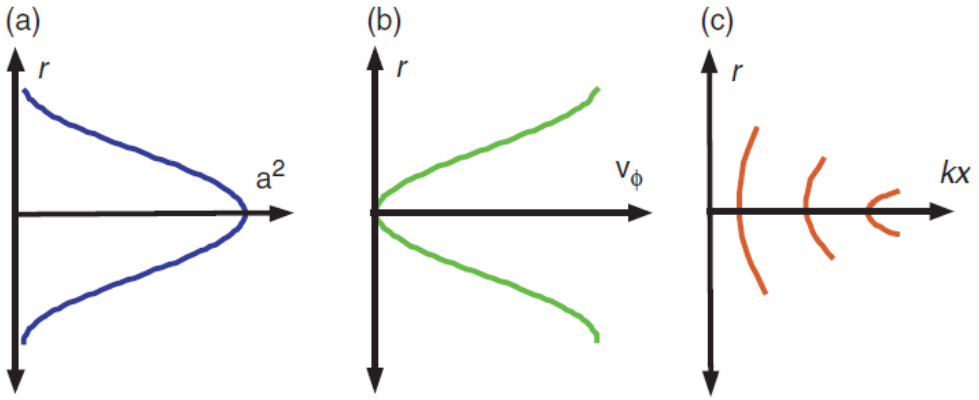

Figure 2.2. Mechanism of relativistic self-focusing. (a) A laser pulse with a transverse Gaussian profile centred on axis produces a larger electron quiver motion on axis than off axis. (b) The phase velocity of light is inversely proportional to the laser intensity via the change in the refractive index. (c) Variation of the phase velocity with radial position focuses the light, acting as a positive lens. From [20].

Relativistic self-focusing occurs for laser powers higher than the critical power defined by [21]:

$$P_c = 17\left(\frac{\omega_0}{\omega_p}\right)^2 [\mathrm{GW}]. \tag{2.9}$$

When the focusing effect is equal to the defocusing due to diffraction, the laser pulse can be self-guided and propagates at high intensity over a long distance.

2.3.2 Pulse compression

Longitudinal variations in the refractive index can also occur. A laser pulse propagating in a low density and high refractive index plasma will have a larger group velocity than a laser beam propagating in a high density plasma. This is because the group velocity depends also on the refractive index n: $v_g = nc$. This can lead to compression of a laser pulse while propagating in a plasma medium [22]. For instance in the bubble regime (defined in section 2.8 of this thesis), if the back of a laser pulse is in the low density region at the centre of the bubble and the front of the laser pulse is in the high density region in the front of the bubble, the high refractive index in the centre of the bubble will make the laser pulse have a larger group velocity than in the front of the pulse. This will make the back of the pulse catch up with the front of the pulse, thus compressing it and increasing the peak intensity.

2.4 The ponderomotive force

The ponderomotive force [23] is responsible for generating the plasma waves in laser plasma acceleration. It can be derived using the electron fluid momentum equation in the cold fluid limit:

$$\frac{d\vec{p}}{dt} = -e\left[\vec{E} + \frac{\left(\vec{v} \times \vec{B}\right)}{c}\right], \tag{2.10}$$

with *p* and *v* the momentum and velocity of the electrons where:

$$\frac{d}{dt} = \frac{\partial}{\partial t} + (\vec{v} \cdot \nabla). \tag{2.11}$$

Assuming a linearly polarised laser the electric and magnetic fields can be expressed as:

$$\vec{E} = -\left(\frac{\partial \vec{A}}{\partial ct}\right), \tag{2.11}$$

and the magnetic field as:

$$\vec{B} = \nabla \times \vec{A}. \tag{2.12}$$

The normalised vector potential in the linear limit is:

$$|a| = \frac{e|A|}{m_e c^2} \ll 1, \tag{2.13}$$

and from $\partial\overrightarrow{p_q}/\partial t = -e\vec{E}$ the main term of the solution of equation 2.10 is the quiver momentum:

$$\overrightarrow{p_q} = m_e c\vec{a}. \tag{2.14}$$

Introducing $\vec{p} = \overrightarrow{p_q} + \delta\vec{p}$ we obtain:

$$\frac{d\delta\vec{p}}{dt} = -\left[\left(\frac{\overrightarrow{p_q}}{m_e}\right)\cdot\nabla\right]\overrightarrow{p_q} - \overrightarrow{p_q}\times(c\nabla\times\vec{a}) = -m_e c^2\nabla\left(\frac{a^2}{2}\right). \tag{2.15}$$

Finally, the expression for the ponderomotive force in the non-relativistic regime is:

$$\overrightarrow{F_p} = -m_e c^2\nabla\left(\frac{a^2}{2}\right) = -\frac{e^2}{2m_e}\nabla A^2. \tag{2.16}$$

The ponderomotive force can also be understood as the radiation pressure, *i.e.* the gradient of the electromagnetic energy density.

In the relativistic case ($a \geq 1$) the important characteristics of the non-relativistic case apply [24, 25], *i.e.* the averaged electron motion is independent of the polarisation of the laser and the electrons are expelled from high-intensity regions.

Several authors [25, 26] have calculated the ponderomotive force in the relativistic regime. Particularly, Quesnel and Mora [25] proved that for a linearly polarised laser the ponderomotive force in the relativistic regime can be calculated by substituting m_e for γm_e in equation 2.16. This is valid under the following assumptions:

- The pulse length $c\Delta\tau$ is much longer than the laser wavelength such that:

$$\sigma = \frac{\lambda}{c\Delta\tau} \ll 1, \tag{2.17}$$

- The transverse scale of the intensity gradient is much larger than the wavelength such that:

$$\varepsilon = \frac{1}{w_0 k_0} \ll 1, \tag{2.18}$$

where w_0 the beam waist and k_0 the laser wave number.

- The initial electron velocity, normalised to c, is small compared with σ and ε.

Assuming this, it is possible to write the ponderomotive force for the relativistic case as follows:

$$\overrightarrow{F_p} = -\frac{e^2}{2\gamma m_e}\nabla A^2. \tag{2.19}$$

2.5 Plasma waves

The ponderomotive force (equation 2.19) of a high intensity laser propagating through an under-dense plasma (*i.e.*, $\omega_0 \gg \omega_p$) expels all the electrons from the laser pulse region leaving the heavy ions behind. This charge separation sets up a restoring Coulomb force from the stationary ions, which attracts back the electrons causing them to oscillate. As a result, highly nonlinear relativistic plasma waves capable of accelerating electrons are created. This is illustrated in Figure 2.3.

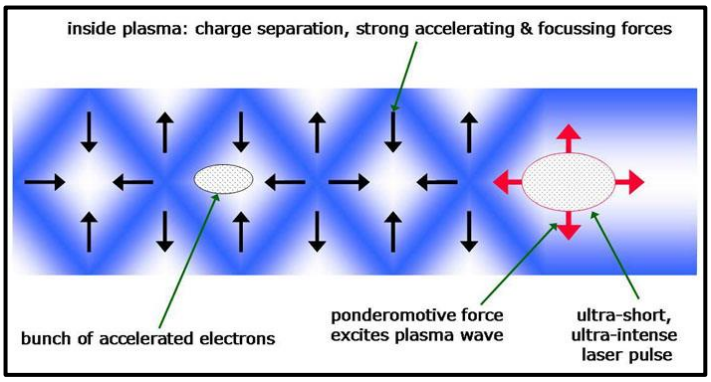

Figure 2.3. Schematic of the ponderomotive force exciting plasma waves [27]. *Electrons (in blue) are expelled by the ponderomotive force (red arrows) setting up large amplitude plasma waves.*

The energy in the plasma wave will be re-absorbed by the trailing part of the laser pulse if the laser pulse length, $c\Delta\tau$, is long compared with the electron plasma wavelength. On the other hand, the energy in the plasma wave will not be re-absorbed if the laser pulse length is equal to or shorter than the plasma

wavelength. In this case, the ponderomotive force excites a wakefield with a phase velocity equal to the laser group velocity. Thus, any pulse with a sharp rise or a sharp fall on a scale of c/ω_p will excite a wake.

2.5.1 Linear plasma waves

In the non-relativistic regime ($a_0 \ll 1$) the generation of plasma waves can be studied using the cold fluid equations. These equations are the Poisson equation, the continuity equation and the fluid momentum equation. Plasma waves generated in a uniform plasma have been described by Gorbunov, Sprangle and Esarey, respectively [28-30].

The normalised density perturbation associated with an electrostatic wake in the linear limit can be written:

$$\frac{\delta n}{n_0} = \frac{(n - n_0)}{n_0}. \tag{2.20}$$

The solution for the density perturbation and the electric field of the wake respectively are [18]:

$$\frac{\delta n}{n_0} = \frac{\left(\frac{c^2}{\omega_p}\right)\int_0^t dt' \sin\left[\omega_p(t-t')\right]\nabla^2 a^2(r,t')}{2}, \tag{2.21}$$

$$\frac{\boldsymbol{E}}{E_0} = \frac{-c\int_0^t dt' \sin\left[\omega_p(t-t')\right]\nabla^2 a^2(\boldsymbol{r},t')}{2}. \tag{2.22}$$

Both equations describe plasma waves generated at the frequency ω_p. They are valid as long as $E \ll E_0$, where $E_0 = m_e c\omega_p/e$. This equation sets the maximum amplitude for a linear plasma wave and is called the cold linear wave breaking field [31].

It is important to point out that the solution to equations 2.21 and 2.22 shows that the plasma waves will be more efficiently generated when the pulse length is of the order of the plasma wavelength $\lambda_p = 2\pi c/\omega_p$.

Another important point is that transverse wakefields E_r and B_θ are also generated. The transverse fields correspond to focusing and defocusing regions being the radial forces cancelled out on axis. If $a^2 \ll 1$ then $E_z \sim E_r \sim a^2$ and $B_\theta \sim a^4$. Electrons travelling close to the speed of light in the plasma waves will experience both longitudinal acceleration and transverse focusing forces within $\lambda_p/4$ of the plasma period.

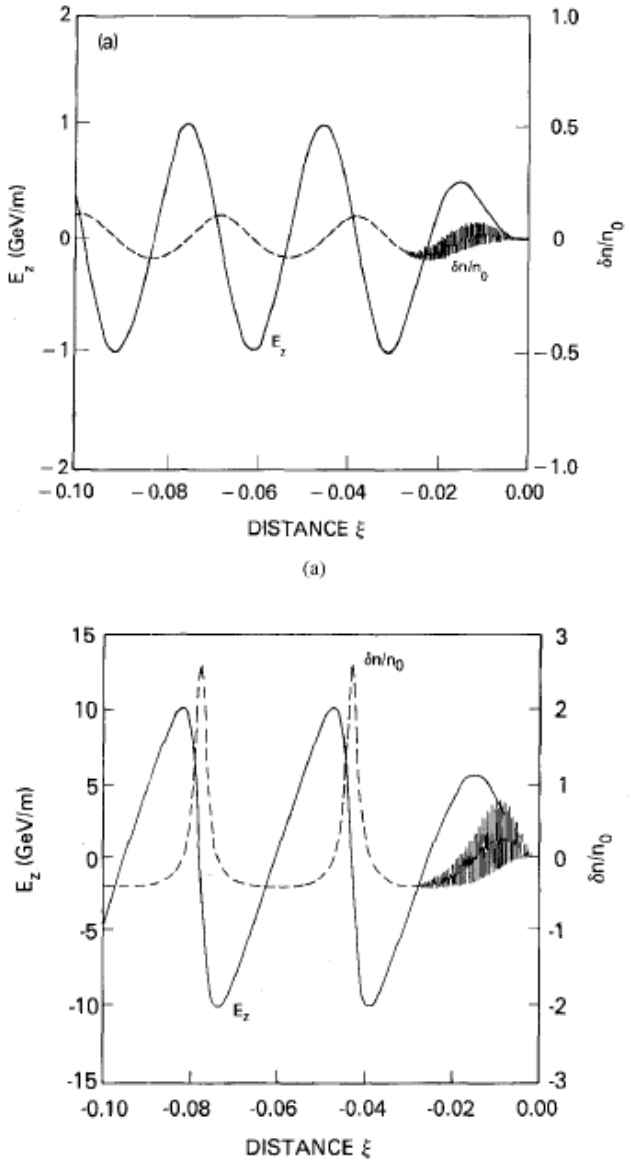

Figure 2.4. Density variations $\delta n/n_0$ and axial electric field E_z in a LWFA in the linear (top) and nonlinear regime (bottom). From [32].

2.5.2 Nonlinear plasma waves

In the linear regime the plasma wave is a simple sinusoidal oscillation at frequency ω_p. When $E \gg E_0$ the plasma waves become nonlinear. Sprangle, Esarey and Ting [33] gave analytical solutions in 1D in the quasi-static approximation for the density perturbation and longitudinal fields in the nonlinear regime. In this approximation, it is assumed that the laser does not evolve in the time it takes to move a plasma wavelength, which is known as the quasi-static approximation.

The most important characteristic of nonlinear plasma waves is that the electric field exhibits a "saw-tooth" profile. This profile is associated with wave steepening and the density oscillations become highly peaked (Figure 2.4). The period of the plasma wave increases as the amplitude increases. In the limit $\gamma_p \gg 1$ the plasma wavelength is given by the following equation [33-35]:

$$\lambda_{Np} = \left(\frac{2\lambda_p}{\pi}\right)\frac{E_{max}}{E_0}, \tag{2.23}$$

where E_{max} is the plasma wave peak electric field.

2.6 Wave breaking

Plasmas can support large plasma waves with phase velocities close to the speed of light. Dawson [31] introduced the concept of wave breaking to describe the limiting amplitude of the plasma waves. In a cold plasma and in the nonrelativistic case the wave-breaking amplitude is given by:

$$E_{WB} = \frac{m_e c \omega_p}{e} = E_0, \tag{2.24}$$

When this amplitude is reached, the wave form steepens. Dawson showed that if plasma is modelled with 1D sheets then wave breaking is equivalent to the crossing of neighbouring sheets.

However, thermal effects reduce the maximum wave amplitude for two reasons:

1. Plasma pressure opposes the trend of the plasma density to increase to infinity,
2. The thermal velocity of the particles moving in the same direction of the wave traps them at a lower wave amplitude.

Thermal corrections to equation 2.24 were studied by Coffey [36]. He used a waterbag model for the electron distribution and obtained the following equation for the nonrelativistic case in a warm plasma:

$$E_{WB} = \frac{m\omega_p v_{ph}}{e}(1 - \frac{1}{3}\beta - \frac{8}{3}\beta^{\frac{1}{4}} + 2\beta^{\frac{1}{2}})^{\frac{1}{2}}, \tag{2.25}$$

where $\beta = 3T/(mv_{ph}^2)$, T is the plasma thermal energy and v_{ph} is the wave phase velocity.

However, the fact that the electrons reach relativistic velocity must be taken into account. The wave-breaking amplitude of cold relativistic oscillations was given by Akhiezer and Polovin [37]:

$$E_{WB} = E_0\sqrt{2(\gamma_p - 1)}, \tag{2.26}$$

where γ_p is the Lorentz factor of the plasma electrons.

Katsouleas and Mori [38] calculated the wave-breaking amplitude in the relativistic regime for a warm plasma taking into account the thermal effects previously mentioned. They obtained the following equation:

$$E_{WB} = E_0\beta^{-\frac{1}{4}}\sqrt{\ln 2\gamma_p^{\frac{1}{2}}\beta^{\frac{1}{4}}} \tag{2.27}$$

2.7 Laser plasma acceleration configurations

There are four main types of laser plasma accelerators: the LWFA, the plasma beat-wave accelerator (PMBA), the self-modulated (SM) LWFA and the resonant laser pulse train. A brief description of each accelerator is given in this section.

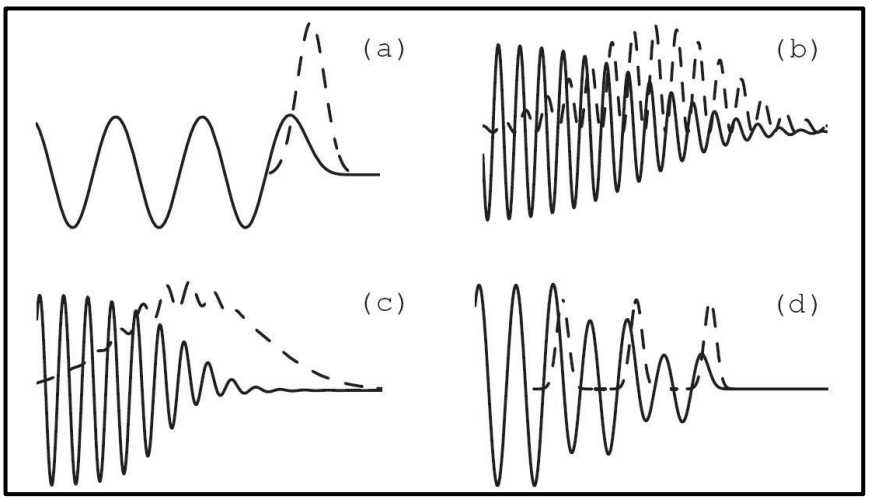

Figure 2.5. Types of laser plasma accelerators: (a) laser wakefield accelerator, (b) plasma beat-wave accelerator, (c) self-modulated laser wakefield accelerator, (d) resonant laser pulse train. The solid lines represent the excited plasma wave potentials and the dashed lines represent laser intensity envelopes moving on the right direction. Figure from [18].

(a) Laser Wakefield Accelerator

In the LWFA [1] a high intensity (≥10^{17} W/cm^2) short laser pulse (≤1 ps) drives a plasma wave as it propagates through under-dense plasma $\omega_0 \gg \omega_p$. The ponderomotive force of the laser expels electrons from the high-intensity region of the laser pulse, while the ions remain almost stationary setting up large accelerating fields. The density waves are efficiently driven when the pulse duration of the laser is approximately equal to the plasma wavelength.

The nonlinear theory of the LWFA in one dimension was developed by Bulanov, Berezhiani and Sprangle [34, 35, 39]. The nonlinear theory of the LWFA in two dimensions was analysed by Sprangle [40] and Esarey [30].

(b) Plasma beat wave accelerator

This scheme was proposed by Tajima and Dawson [1] when CPA was not yet developed by Mourou and collaborators. In the PBWA, plasma waves are

generated by the ponderomotive force of two long laser pulses. The two laser pulses are separated in frequency by the plasma frequency such as: $\omega_1 - \omega_2 = \omega_p$. Due to the fact that this frequency difference is equal to ω_p, the plasma responds resonantly to the ponderomotive force and large plasma waves are created.

Particles that are injected into the beat wave region with similar velocity to the phase velocity of the plasma wave gain more energy from the longitudinal electric field. The Lorentz factor γ_p associated with the beat waves is:

$$\gamma_p = \left(1 - \frac{v_{ph}^2}{c^2}\right)^2 = \frac{\omega_{1,2}}{\omega_p} \gg 1. \qquad (2.28)$$

The beat wave process is related to stimulated Raman forward scattering (SRFS). SRFS is the process of the scattering of electromagnetic waves by longitudinal electron plasma waves. If the scattered electromagnetic wave propagates in the same direction as the incident electromagnetic wave the process is called forward scattering.

As in LWFA there are two main factors that limit this acceleration scheme: diffraction and pump depletion. Both phenomena are explained in section 2.6. Diffraction can be overcome using plasma waveguides. To avoid pump depletion it is necessary to use more powerful lasers.

(c) <u>Self-modulated laser wakefield accelerator (SMLWFA)</u>

This concept combines elements of SRFS [41] and the LWFA. Raman forward scattering (RFS) is the process by which a wave of frequency ω_0 decays into a wave of $\omega_0 \pm \omega_p$ and a plasma wave ω_p with phase velocity approximately equal to the speed of light. When RFS is combined with LWFA this configuration becomes an interesting alternative.

In order to work in the self-modulated regime two conditions must be satisfied:

1. The pulse length of the laser has to be longer than the plasma wavelength, i.e. $L > \lambda_p$.

2. The laser pulse power has to be higher than the critical power for self-focusing [21]:

$$P_c = 17\left(\frac{\omega}{\omega_p}\right)^2 \text{GW}. \tag{2.29}$$

The SMLWFA has the advantage that it is a simpler scheme than the LWFA configuration since the matching condition $L \cong \lambda_p$ is not required. Moreover, a higher acceleration gradient is achieved with this scheme. The reasons for this are the following:

1. SMLWFA works at a higher density and therefore larger plasma waves will be generated.
2. Since $P > P_c$ the laser will focus to a higher intensity and therefore a_0 will be larger.
3. The wakefield is excited by a series of beamlets. In the standard LWFA the wakefield is produced by a single laser pulse.
4. The pulse structure propagates for several Rayleigh lengths (as long as relativistic self-focussing occurs or the pulse propagates in a waveguide) and therefore the acceleration distance is longer.

However, SMLWFA has disadvantages as well. The main ones are the following:

1. The acceleration distance is limited by dephasing since at higher densities the group velocity of the laser pulse decreases.
2. The low quality of the electron beam produced (broad energy spread). This is due to constant trapping and the short dephasing lengths.
3. The modulated pulse structure eventually diffracts.

(d) <u>Resonant laser pulse train</u>

In the PBWA configuration, the laser beat wave acts as a series of short laser pulses. However, as the plasma wave grows the plasma period is increased, leading to a loss of resonance with respect to the laser beat pulses. The beat period can be adjusted to maximise the amplitude of the plasma waves.

The resonant laser-plasma accelerator [42] drives a plasma wave using an optimum train of short laser pulses. In this configuration, both the width and spacing of each laser pulse can be separately controlled. If this separation is properly optimised, the saturation of the plasma wave by resonant detuning can be eliminated.

In the linear regime, and assuming square laser pulses ($a^2 \ll 1$ and $E_{max}/E_0 \ll 1$), the pulse train is optimised when a number m of pulses of width $L = \lambda_p/2$ are separated by a distance equal to $(2l+1)\lambda_p/2$ with l being an integer. Under this condition, the plasma wave amplitude will be:

$$\frac{E_{max}}{E_0} = ma_0^2. \tag{2.30}$$

In the nonlinear regime, both pulse width and spacing have to be optimised for each individual pulse. The optimal conditions and the amplitude of the plasma waves in this regime were obtained by [42, 43] using numerical simulations.

2.8 The "bubble" or blow-out regime

When the laser intensity is sufficiently high, all the plasma electrons are expelled from the vicinity of the laser axis propagation [24] and the laser wake has the shape of a plasma cavity. Moreover, some plasma electrons are self-trapped in the electron cavity and are accelerated to very high energy [14]. This regime has been studied for laser drivers [44, 45], and for electron beam drivers [46], which the latter refers to the nonlinear plasma wakefield accelerator PWFA. Pukhov and Meyer-ter-Vehn observed the bubble regime in 3D PIC simulations for high intense laser pulses shorter than λ_p.

The most important characteristics of the bubble regime are the following:

1. A cavity free from electrons is produced behind the laser pulse.
2. Mono-energetic bunches of relativistic electrons are generated.
3. The laser pulse propagates over many Rayleigh lengths without significant diffraction.

In the bubble, there are three different density regions (clearly observed in Figure 2.6):

1. The plasma cavity with large ion charge.
2. The electron sheath around the plasma cavity forming the bubble.
3. The accelerated electron bunch behind the laser pulse.

The density of the electron sheath is maximum at the head of the laser pulse and at the base of the bubble. These peaks are relativistic electrons with velocity $v \cong v_0$. Electrons from the bubble base are trapped and accelerated to $\gamma \gg \gamma_0$ where γ_0 is the relativistic Lorentz factor of the laser pulse.

Assuming that the ponderomotive force of the laser $k_p \nabla a_0^2/\gamma \sim a_0/(k_p R)$ [45], where R is the bubble radius, is equal to the restoring force of the ion channel $F_p \sim k_p R$ it is possible to calculate the bubble radius:

$$k_p R \sim \sqrt{a_0}. \tag{2.31}$$

where $k_p = 2\pi/\lambda_p$ is the plasma wavenumber. The bubble radius is proportional to the laser spot size w_0, *i.e.* $k_p w_0 \sim k_p R$.

Through PIC simulations Lu *et al.* [45] found a more refined condition that leads to only slight oscillations in the spot size:

$$k_p w_0 \cong k_p R = 2\sqrt{a_0}. \tag{2.32}$$

This relationship is still valid for $a_0 \geq 2$.

Kostyukov, Pukhov and Kiselev [47] calculated the electromagnetic fields felt by an electron in the plasma bubble. They assumed ions to be stationary and the cavity moving with relativistic velocity $v_0 \approx c$ along the x axis.

From Maxwell's equations they found the electric potential inside the bubble to be (in units normalised to the plasma frequency):

$$\Phi = 1 - \frac{R^2}{4} + \frac{r^2}{4}, \tag{2.33}$$

where R is the bubble radius and $r^2 = \xi^2 + y^2 + z^2$. Here, $\xi = x - v_0 t$ and v_0 is the bubble velocity.

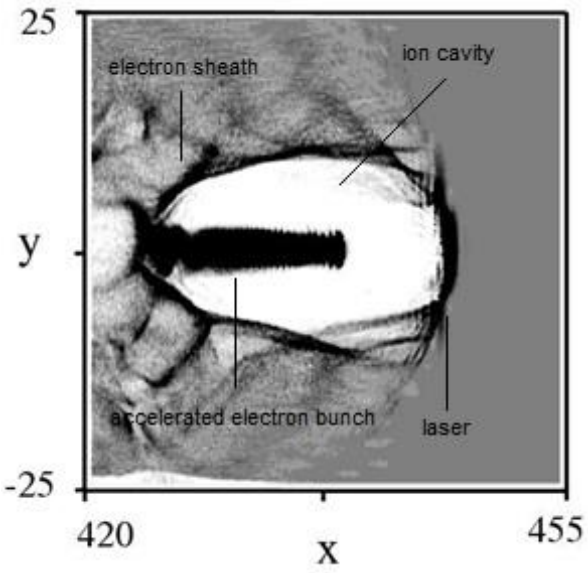

Figure 2.6. 3D PIC simulation showing a bubble picture where the three main density regions can be observed. Coordinates are in c/ω_p. From [48].

The fields inside the cavity are:

$$E_x = \frac{\xi}{2}, \quad E_y = -B_z = \frac{y}{4}, \tag{2.34}$$

$$B_x = 0, \qquad E_z = B_y = \frac{z}{4}. \tag{2.35}$$

The Lorentz force acting on a relativistic electron in the bubble is:

$$F_x = -\frac{\partial \Phi}{\partial \xi} = -E_x = -\frac{\xi}{2}, \tag{2.36}$$

$$F_y = -\frac{\partial \Phi}{\partial y} = -E_y + B_z = -\frac{y}{2}, \tag{2.37}$$

$$F_z = -\frac{\partial \Phi}{\partial z} = -E_z - B_y = -\frac{z}{2}. \quad (2.38)$$

The Lorentz force is maximum for electrons with $v_x = v_0 = 1$ and zero for electrons with $v_x = -1$, where the velocities have been normalised to the speed of light in vacuum.

2.8.1 Energy gain in the bubble regime:

The electrons that are trapped in the bubble are accelerated. Acceleration lasts until the electrons outrun the wave reaching the middle of the bubble (dephasing length). The phase velocity of the wake can be written as [45]:

$$v_\varphi \cong c\left[1 - \frac{3\omega_p^2}{(2\omega_0^2)}\right]. \quad (2.39)$$

Therefore, the distance the electrons travel before dephasing is:

$$L_d \cong \frac{c}{c - v_\varphi} \cong \frac{2\omega_0^2}{3\omega_p^2} R, \quad (2.40)$$

and the energy gain can be written in the following equation:

$$\Delta E = qE_{LW}L_{acc} = \epsilon_{LW} l_{acc} mc^2, \quad (2.41)$$

where E_{LW} is the average accelerating field experience by the electrons, L_{acc} is the length of acceleration, and $\epsilon_{LW} = eE_{LW}/(mc\omega_p)$, $l_{acc} = \omega_p L_{acc}/c$.

Assuming that the bubble is approximately a sphere of radius R, the electrons travel a distance R before dephasing. For $a_0 > 4$ the peak accelerating field [45] is $\epsilon_{LW} \cong \sqrt{a_0}$ and the average field is half of the peak accelerating field: $\epsilon_{LW} \cong \sqrt{a_0}/2$. Therefore, the energy gain is [45]:

$$\Delta E_{Lu} \cong \frac{2}{3} mc^2 \left(\frac{\omega_0}{\omega_p}\right)^2 a_0 \cong mc^2 \left(\frac{P}{\frac{m^2c^5}{e^2}}\right)\left(\frac{n_c}{n_p}\right)^{\frac{2}{3}}. \quad (2.42)$$

It is possible to write this equation in more convenient units:

$$\Delta E_{Lu}[\mathrm{GeV}] \cong 1.7 \left(\frac{P[\mathrm{TW}]}{100}\right)^{\frac{1}{3}} \left(\frac{10^{18}}{n_p[\mathrm{cm}^{-3}]}\right)^{\frac{2}{3}} \left(\frac{0.8}{\lambda_0[\mu m]}\right)^{\frac{4}{3}}. \quad (2.43)$$

This equation points out the dependence of the electron beam energy on the plasma density and on the laser power. It is important to note that if the plasma density is decreased for a certain laser power it is difficult to keep the self-guiding of the laser pulse. In order to do so, preformed plasma channels must be used.

It is possible to write equation 2.42 as a function of the critical power for relativistic self-focusing:

$$\Delta E_{Lu}[\mathrm{GeV}] \cong 3.8 \left(\frac{P}{P_c}\right)^{-\frac{2}{3}} \frac{P[\mathrm{TW}]}{100}. \quad (2.44)$$

Pukhov and Gordienko [49] also studied the energy gained by the electrons in the bubble regime. The key assumption they made was that $a_0 \gg 1$. The equation they obtained is:

$$\Delta E_{Pukhov} \cong 0.65 mc^2 \sqrt{\frac{P}{\frac{m^2c^5}{e^2}}} \frac{c\Delta\tau}{\lambda}. \quad (2.45)$$

It is important to note that, this equation emphasises the dependence of the electron energy gain only on the laser power.

If we make the assumption that $c\Delta\tau \approx \omega_0 \approx \sqrt{a_0}c/\omega_p$ equation 2.45 can be written as:

$$\Delta E_{Pukhov} \cong 0.16mc^2 \frac{c\Delta\tau}{w_0}\left(\frac{P}{\frac{m^2c^5}{e^2}}\right)^{\frac{2}{3}}\left(\frac{n_c}{n_p}\right)^{\frac{1}{3}}. \quad (2.46)$$

2.8.2 Beam loading:

The number of particles that can be loaded into a linear wakefield was studied by Katsouleas *et al* [50]. In order to obtain the accelerating field, Katsouleas superimposed the wakefield generated by the driver to the wakefield generated by the accelerated electrons. He assumed that the wake behind an ultrashort and unshaped accelerated bunch of electrons vanishes, thus obtaining:

$$N_0 \cong 5 \times 10^5 \left(\frac{\delta n}{n_p}\right)\sqrt{n_p}A, \quad (2.47)$$

where δn is the density perturbation of the wake and A is the cross-sectional area of the wake in cm^2.

When estimating the amount of charge that can be loaded into the wake only an area $A_{eff} \sim c^2/\omega_p^2$ should be used [50]. Therefore, using $1/k_p \equiv c/\omega_p \cong 5.3 \times 10^5/\sqrt{n_p}$ the maximum number of electrons is:

$$N_0 \cong \left(\frac{\delta n}{n_p}\right) n_p k_p^{-3} \cong \frac{1.5 \times 10^8}{\sqrt{n_p[10^{18}\mathrm{cm}^{-3}]}}\left(\frac{\delta n}{n_p}\right). \quad (2.48)$$

In the linear regime, $\delta n/n_p \ll 1$. The maximum value will be when $\delta n/n_p \sim 1$, although in this case the nonlinearities have to be taken into consideration.

The nonlinear regime was studied by Lu *et al*. [45], Gordienko and Pukhov [49]. Lu *et al.* obtained the number of electrons that can be loaded into the wake using energy balance. They found out by integrating the energy field in the ion channel that the energy in the longitudinal field is approximately equal to the energy of the focusing fields $\varepsilon_l \sim \varepsilon_f$ [45]:

$$\varepsilon_l \cong \varepsilon_f \cong \frac{1}{2}\varepsilon = \frac{1}{120}\left(k_p R\right)^5 \left(\frac{m^2c^5}{e^2\omega_p}\right). \tag{2.49}$$

Equating ϵ to the energy that N electrons absorbed when travelling along the ion channel and assuming that the average electric field felt by the electrons is $E_{z,max}/2$ we obtain:

$$N \cong \frac{1}{30}\left(k_p R\right)^3 \frac{1}{k_p r_e} = \left(\frac{\beta}{\alpha}\right)^3 \frac{8}{15}\frac{1}{k_0 r_e}\sqrt{\frac{P}{\frac{m^2c^5}{e^2}}}, \tag{2.50}$$

where $r_e = e^2/(mc^2)$ is the classical electron radius, $\alpha = k_p w_0/\left(2\sqrt{a_0}\right)$ and $\beta = k_p R/\left(2\sqrt{a_0}\right)$. Finally, using equation 2.32 and $\alpha \cong \beta \cong 1$ the number of electrons that can be loaded in a nonlinear wakefield is [45]:

$$N_{Lu} \cong \frac{8}{15}\frac{1}{k_0 r_e}\sqrt{\frac{P}{\frac{m^2c^5}{e^2}}}. \tag{2.51}$$

In more convenient units we can write:

$$N_{Lu} \cong 2.5 \times 10^9 \frac{\lambda_0[\mu m]}{0.8}\sqrt{\frac{P[\mathrm{TW}]}{100}}. \tag{2.52}$$

Similar scaling was obtained by Gordienko and Pukhov [49], although they determined the coefficient from PIC simulations:

$$N_{Pukhov} \cong \frac{1.8}{k_0 r_e}\sqrt{\frac{P}{m^2c^5/e^2}} \tag{2.53}$$

It is important to note two things:

1. Lu *et al.* assumed that the bubble was not modified by the presence of the load whereas in the simulations that Gordienko and Pukhov performed, the wake was loaded by trapped electrons.

2. Although Gordienko's and Pukhov's coefficient is three times larger than Lu's coefficient this does not mean that the results are contradictory. In principle, it is possible to either accelerate a small number of electrons to high energy or a large number of electrons to small energy.

2.9 Limitations to acceleration

There are mainly three processes that limit the electron energy gain in the LWFA: laser diffraction, electron dephasing and laser pump depletion. A brief description of these mechanisms is given in this section.

a) <u>Laser diffraction</u>

When in vacuum, the laser spot radius undergoes Rayleigh diffraction and changes according to the following equation:

$$r_s = r_0\left(1+\frac{z^2}{Z_R^2}\right)^{\frac{1}{2}}, \tag{2.54}$$

where r_0 is the spot size at the focal point and $Z_R = kr_0^2/2$ is the Rayleigh length. In the absence of some form of optical guiding the laser-plasma interaction is limited to a few Rayleigh lengths unless the laser and plasma parameters satisfy conditions that lead to self-guiding. For example, as explained in section 2.3.1, relativistic self-focusing occurs for a laser power higher than the critical power. Another technique for optical guiding, which is effective also at lower intensities is the gas-filled capillary, where the plasma is formed by high voltage discharge in gas [51, 52]. These waveguides are usually made of sapphire and normally filled with hydrogen. Manufacturing of capillary waveguides using a femtosecond laser micromachining technique was first proposed by the University of Strathclyde group [53].

b) <u>Electron dephasing</u>

As electrons are accelerated by plasma waves their velocity will increase and get close to the speed of light. If the phase velocity of the plasma wave is

constant and less than speed of light, i.e. $v_p < c$, the electrons will outrun the plasma wave and move to the decelerating region of the plasma wave. This effect limits the energy gained by electrons and is known as electron dephasing. The dephasing length L_d is defined as the length over which an electron has to move before its phase slips by a half of a period with respect to the plasma wave.

The dephasing length, in both linear and nonlinear regime in the case of a LWFA driven by a linearly polarised square laser pulse with duration $L = \lambda_{Np}/2$ is given by [54]:

$$L_d \cong \frac{\lambda_p^3}{2\lambda^2} \qquad \text{for } a_0^2 \ll 1, \tag{2.55}$$

$$L_d \cong \frac{\lambda_p^3}{2\lambda^2}\frac{a_0\sqrt{2}}{N_p\pi} \quad \text{for } a_0^2 \gg 1, \tag{2.56}$$

where N_p is the number of plasma periods behind the laser pulse.

c) <u>Pump depletion</u>

As the laser excites the wake it loses energy. This means its energy etches away and depletes, resulting in a reduction of the group velocity and a decrease in the wakefield phase velocity. The pump depletion equations for the linear and nonlinear regime are given by [54]:

$$L_{pd} \cong \frac{2}{a_0^2}\frac{\lambda_p^3}{\lambda^2} \text{ for } a_0^2 \ll 1, \tag{2.57}$$

$$L_{pd} \cong \frac{\lambda_p^3}{\lambda^2}\frac{a_0\sqrt{2}}{\pi} \text{ for } a_0^2 \gg 1. \tag{2.58}$$

Looking at equations 2.55-2.58 it is easy to see that $L_d \ll L_{pd}$ in the linear regime, so in this case electron acceleration is limited by dephasing. On the other hand, in the nonlinear regime, electron acceleration is limited by both pump depletion and dephasing.

2.10 Betatron oscillations

When electrons are expelled by the ponderomotive force of a laser pulse an ion column is formed. If all the electrons are expelled from the channel, then the restoring force on the electrons due to the ions can be calculated using Gauss' law. In cylindrical geometry:

$$\frac{d\vec{p}}{dt} = \vec{F}_{res} = -\frac{m\omega_p^2 \vec{r}_\perp}{2}, \tag{2.59}$$

where $\vec{r}_\perp$ is the vector from the electron to the axis of the channel. Electrons injected at the back of the bubble off axis or with a finite transverse momentum will experience this restoring force which causes the electrons to undergo betatron oscillations. The frequency ω_b of the betatron oscillations is:

$$\omega_b \cong \frac{\omega_p}{\sqrt{2\gamma}}, \tag{2.60}$$

with γ being the Lorentz factor of the accelerated electrons.

The plasma acts as a wiggler making the electrons oscillate in the ion channel, in the same way as in a conventional wiggler [55], and emit short wavelength electromagnetic radiation [56]. The strength parameter of the plasma wiggler is given by:

$$K = \gamma\theta = \gamma k_b r_b = 1.33 \times 10^{-10}\sqrt{\gamma n_e[\mathrm{cm}^{-3}]}\, r_b[\mu\mathrm{m}], \tag{2.61}$$

where r_b is the amplitude of the electron oscillation in the ion channel, n_e is the plasma density and θ is the maximum angle of the oscillatory motion described by the electron.

Due to the strongly relativistic motion of the electron, the electromagnetic radiation is emitted in a narrow angle given by:

$$\theta = \frac{K}{\gamma}. \tag{2.62}$$

For small amplitude oscillations, i.e. $K \ll 1$, the frequency of the emitted radiation is the fundamental frequency:

$$\omega_f \cong \omega_b 2\gamma^2. \tag{2.63}$$

If the strength parameter is such that $K \gg 1$ then the spectrum of the electromagnetic radiation emitted is similar to a synchrotron spectrum. The function determining this synchrotron spectrum is an integral of the Bessel function given by [57]:

$$S\left(\frac{\omega}{\omega_f}\right) = x \int_x^\infty K_{\frac{5}{3}}(\xi) d\xi. \tag{2.64}$$

For frequencies below the critical frequency the spectrum increases with frequency $\omega^{\frac{2}{3}}$ and it peaks at $\sim 0.3\omega_f$ dropping then exponentially to zero.

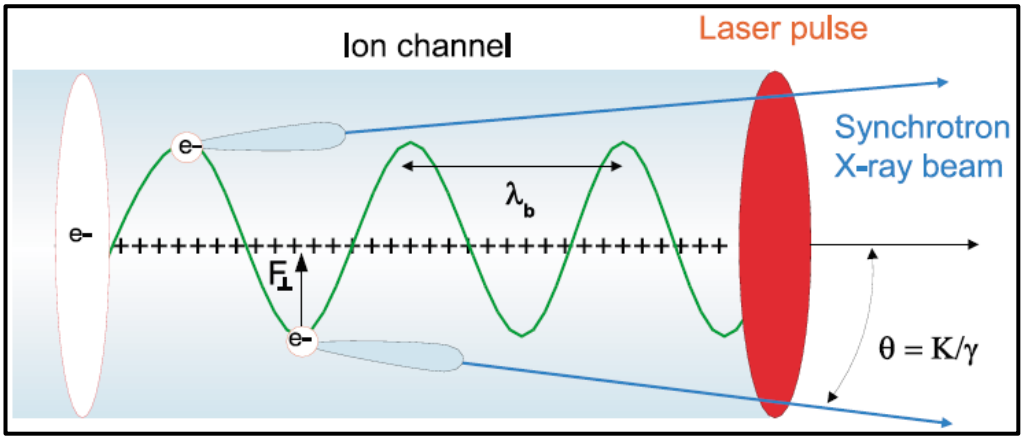

Figure 2.7. Trajectory of a single electron oscillating in the ion channel created by the ponderomotive force of a high intensity laser pulse. From [58].

The critical frequency of the radiation emitted by an electron oscillating in the ion channel is:

$$\hbar\omega_c = \frac{3}{2}\gamma^3\hbar c r_b k_b^2 \cong 5\times10^{-24}\gamma^2 n_e[\mathrm{cm}^{-3}] r_b[\mu\mathrm{m}]\mathrm{keV}. \quad (2.65)$$

The average power radiated by a single electron undergoing betatron oscillations can be calculated using the relativistic Larmor formula [57]. This gives the following equation [57]:

$$\langle P_{total}\rangle \cong \frac{e^2 c}{12}\gamma^2 k_p^4 N_0^2, \quad (2.66)$$

where N_0 is the number of oscillations undergone by the electron.

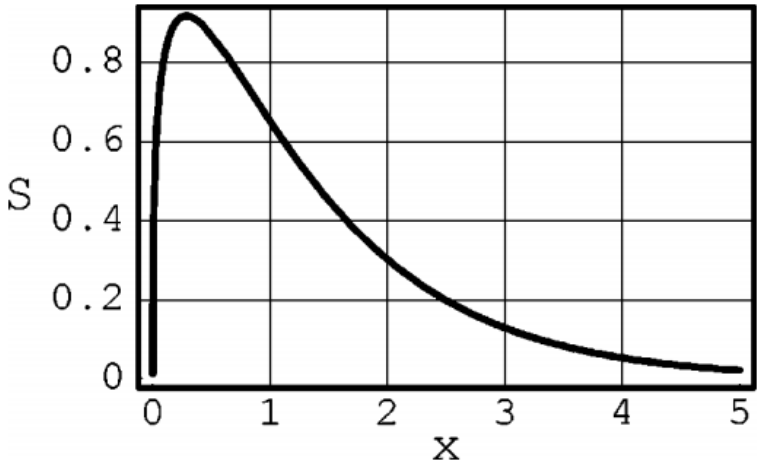

Figure 2.8. Broadband synchrotron spectrum emitted as the integral of the modified Bessel function of the second kind and 5/3 order S(x) vs x. From [56].

The energy lost by an electron per unit distance is given by:

$$Q = \frac{\langle P_{total}\rangle}{c} \cong 1.5\times10^{-45}(\gamma n_e[\mathrm{cm}^{-3}] r_b[\mu\mathrm{m}])^2 \frac{\mathrm{MeV}}{\mathrm{cm}}. \quad (2.67)$$

The number of photons per electron emitted every betatron oscillation cycle is given by:

$$N_{phot} = \frac{2\pi}{9}\alpha_f K, \quad (2.68)$$

where α_f is the fine structure constant.

Chapter references:

1. Tajima, T. and J. Dawson, *Laser electron accelerator.* Physical Review Letters, 1979. **43**(4): p. 267.
2. Joshi, C., et al., *Ultrahigh gradient particle acceleration by intense laser-driven plasma density waves.* Nature, 1984. **311**: p. 525-529.
3. Wilks, S., et al., *Photon accelerator.* Physical Review Letters, 1989. **62**(22): p. 2600.
4. Dawson, J.M., *Particle simulation of plasmas.* Reviews of Modern Physics, 1983. **55**(2): p. 403.
5. Mori, W., et al., *Evolution of self-focusing of intense electromagnetic waves in plasma.* Physical Review Letters, 1988. **60**(13): p. 1298.
6. Birdsall, C.K. and A.B. Langdon, *Plasma physics via computer simulation*. 2004: CRC press.
7. Strickland, D. and G. Mourou, *Compression of amplified chirped optical pulses.* Optics Communications, 1985. **55**(6): p. 447-449.
8. Strickland, D., *Optics Commun. 56, 219 (1985) and P. Maine, D. Strickland, P. Bado, M. Pessot and G. Mourou.* IEEE J. Quant. Electron, 1988. **24**: p. 398.
9. Perry, M.D. and G. Mourou, *Terawatt to petawatt subpicosecond lasers.* Science-AAAS-Weekly Paper Edition-including Guide to Scientific Information, 1994. **264**(5161): p. 917-923.
10. Mourou, G. and D. Umstadter, *Development and applications of compact high-intensity lasers.* Physics of Fluids B: Plasma Physics (1989-1993), 1992. **4**(7): p. 2315-2325.
11. Modena, A., et al., *Accelerator physics: Electrons hang ten on laser wake.* Nature, 1995. **377**: p. 606-608.
12. Umstadter, D., et al., *Nonlinear optics in relativistic plasmas and laser wake field acceleration of electrons.* Science, 1996. **273**(5274): p. 472-475.

13. Nakajima, K., et al., *Observation of ultrahigh gradient electron acceleration by a self-modulated intense short laser pulse.* Physical Review Letters, 1995. **74**(22): p. 4428.
14. Faure, J., et al., *A laser–plasma accelerator producing monoenergetic electron beams.* Nature, 2004. **431**(7008): p. 541-544.
15. Geddes, C., et al., *High-quality electron beams from a laser wakefield accelerator using plasma-channel guiding.* Nature, 2004. **431**(7008): p. 538-541.
16. Mangles, S., et al., *Monoenergetic beams of relativistic electrons from intense laser–plasma interactions.* Nature, 2004. **431**(7008): p. 535-538.
17. Caldwell, A., et al., *Path to AWAKE: Evolution of the concept.* Nuclear Instruments and Methods in Physics Research Section A: Accelerators, Spectrometers, Detectors and Associated Equipment, 2016. **829**: p. 3-16.
18. Esarey, E., C. Schroeder, and W. Leemans, *Physics of laser-driven plasma-based electron accelerators.* Reviews of Modern Physics, 2009. **81**(3): p. 1229.
19. Brown, L.S. and T. Kibble, *Interaction of intense laser beams with electrons.* Physical Review, 1964. **133**(3A): p. A705.
20. Umstadter, D., *Relativistic laser–plasma interactions.* Journal of Physics D: Applied Physics, 2003. **36**(8): p. R151.
21. Sun, G.Z., et al., *Self-focusing of short intense pulses in plasmas.* Physics of Fluids (1958-1988), 1987. **30**(2): p. 526-532.
22. Decker, C. and W. Mori, *Group velocity of large amplitude electromagnetic waves in a plasma.* Physical Review Letters, 1994. **72**(4): p. 490.
23. Kruer, W.L., *The Physics of Laser Plasma Interactions.* (Addison-Wesley, Redwood City), 1988.
24. Mora, P. and T.M. Antonsen Jr, *Kinetic modeling of intense, short laser pulses propagating in tenuous plasmas.* Physics of Plasmas (1994-present), 1997. **4**(1): p. 217-229.

25. Quesnel, B. and P. Mora, *Theory and simulation of the interaction of ultraintense laser pulses with electrons in vacuum.* Physical Review E, 1998. **58**(3): p. 3719.
26. Bauer, D., P. Mulser, and W.-H. Steeb, *Relativistic ponderomotive force, uphill acceleration, and transition to chaos.* Physical Review Letters, 1995. **75**(25): p. 4622.
27. Jaroszynski, D.A., R. Bingham, and R. Cairns, *Laser-plasma interactions*. 2009: CRC Press.
28. Gorbunov, L. and V. Kirsanov, *Excitation of plasma waves by an electromagnetic wave packet.* Sov. Phys. JETP, 1987. **66**(290-294): p. 40.
29. Sprangle, P., et al., *Laser wakefield acceleration and relativistic optical guiding.* Applied Physics Letters, 1988. **53**(22): p. 2146-2148.
30. Esarey, E., et al., *Optically guided laser wake-field acceleration*.* Physics of Fluids B: Plasma Physics (1989-1993), 1993. **5**(7): p. 2690-2697.
31. Dawson, J.M., *Nonlinear electron oscillations in a cold plasma.* Physical Review, 1959. **113**(2): p. 383.
32. Esarey, E., et al., *Overview of plasma-based accelerator concepts.* Plasma Science, IEEE Transactions on, 1996. **24**(2): p. 252-288.
33. Sprangle, P., E. Esarey, and A. Ting, *Nonlinear theory of intense laser-plasma interactions.* Physical Review Letters, 1990. **64**(17): p. 2011.
34. Berezhiani, V. and I. Murusidze, *Interaction of highly relativistic short laser pulses with plasmas and nonlinear wake-field generation.* Physica Scripta, 1992. **45**(2): p. 87.
35. Bulanov, S., V. Kirsanov, and A. Sakharov, *Excitation of ultrarelativistic plasma waves by pulse of electromagnetic radiation.* JETP Lett, 1989. **50**(0): p. 4-25.
36. Coffey, T., *Breaking of large amplitude plasma oscillations.* Physics of Fluids (1958-1988), 1971. **14**(7): p. 1402-1406.
37. Akhiezer, A. and R. Polovin, *Theory of wave motion of an electron plasma.* Soviet Phys. JETP, 1956. **3**.

38. Katsouleas, T. and W. Mori, *Wave-breaking amplitude of relativistic oscillations in a thermal plasma.* Physical Review Letters, 1988. **61**(1): p. 90.
39. Sprangle, P., E. Esarey, and A. Ting, *Nonlinear interaction of intense laser pulses in plasmas.* Physical Review A, 1990. **41**(8): p. 4463.
40. Sprangle, P., et al., *Propagation and guiding of intense laser pulses in plasmas.* Physical Review Letters, 1992. **69**(15): p. 2200.
41. Mora, P., *Physics of relativistic laser-plasmas.* Plasma Physics and Controlled Fusion, 2001. **43**(12A): p. A31.
42. Umstadter, D., E. Esarey, and J. Kim, *Nonlinear plasma waves resonantly driven by optimized laser pulse trains.* Physical Review Letters, 1994. **72**(8): p. 1224.
43. Umstadter, D., et al., *Resonantly laser-driven plasma waves for electron acceleration.* Physical Review E, 1995. **51**(4): p. 3484.
44. Pukhov, A. and J. Meyer-ter-Vehn, *Laser wake field acceleration: the highly non-linear broken-wave regime.* Applied Physics B, 2002. **74**(4-5): p. 355-361.
45. Lu, W., et al., *Generating multi-GeV electron bunches using single stage laser wakefield acceleration in a 3D nonlinear regime.* Physical Review Special Topics-Accelerators and Beams, 2007. **10**(6): p. 061301.
46. Rosenzweig, J., et al., *Acceleration and focusing of electrons in two-dimensional nonlinear plasma wake fields.* Physical Review A, 1991. **44**(10): p. R6189.
47. Kostyukov, I., A. Pukhov, and S. Kiselev, *Phenomenological theory of laser-plasma interaction in "bubble" regime.* Physics of Plasmas (1994-present), 2004. **11**(11): p. 5256-5264.
48. Pukhov, A., et al., *The bubble regime of laser–plasma acceleration: monoenergetic electrons and the scalability.* Plasma Physics and Controlled Fusion, 2004. **46**(12B): p. B179.

49. Gordienko, S. and A. Pukhov, *Scalings for ultrarelativistic laser plasmas and quasimonoenergetic electrons.* Physics of Plasmas (1994-present), 2005. **12**(4): p. 043109.
50. Katsouleas, S.W.T. and J.D.J. Su, *Beam Loading Efficiency in Plasma Accelerators.* Part. Accel, 1987. **22**: p. 81-99.
51. Spence, D., A. Butler, and S. Hooker, *First demonstration of guiding of high-intensity laser pulses in a hydrogen-filled capillary discharge waveguide.* Journal of Physics B: Atomic, Molecular and Optical Physics, 2001. **34**(21): p. 4103.
52. Butler, A., D. Spence, and S. Hooker, *Guiding of high-intensity laser pulses with a hydrogen-filled capillary discharge waveguide.* Physical Review Letters, 2002. **89**(18): p. 185003.
53. Wiggins, S., et al., *Note: Femtosecond laser micromachining of straight and linearly tapered capillary discharge waveguides.* Review of Scientific Instruments, 2011. **82**(9): p. 096104.
54. Shadwick, B., C. Schroeder, and E. Esarey, *Nonlinear laser energy depletion in laser-plasma acceleratorsa).* Physics of Plasmas (1994-present), 2009. **16**(5): p. 056704.
55. Whittum, D.H., *Electromagnetic instability of the ion-focused regime.* Physics of Fluids B: Plasma Physics (1989-1993), 1992. **4**(3): p. 730-739.
56. Kostyukov, I., S. Kiselev, and A. Pukhov, *X-ray generation in an ion channel.* Physics of Plasmas (1994-present), 2003. **10**(12): p. 4818-4828.
57. Jackson, J.D., *Classical Electrodynamics (John Wiley, 1999).*
58. Rousse, A., et al., *Production of a keV X-Ray Beam from Synchrotron Radiation in Relativistic Laser-Plasma Interaction.* Physical Review Letters, 2004. **93**(13): p. 135005.

Chapter 3: ALPHA-X Laser system and beamline experimental setup

3.1 ALPHA-X high power laser system

High laser peak intensities can be produced using both the chirped pulse amplification (CPA) scheme [1] and Ti:sapphire amplification crystals [2]. This technology made laser systems of up to 10 PW commercially available and capable of delivering laser pulses of a few femtosecond duration and several Joules of energy. High intensity laser-matter interactions can be achieved by focusing these pulses to tens of *μm* spot size. This is performed routinely in research laboratories giving peak intensities of $10^{18} - 10^{20}\ \mathrm{Wcm^{-2}}$.

The physics community is interested in producing laser systems that can give even higher peak intensities in order to do research into phenomena such as radiation reaction [3] or to reach higher energy in electron beams from laser wakefield accelerators (LWFAs). Facilities such as the Extreme Light Infrastructure (ELI) [4] aim for laser peak intensities up to $10^{23}\ \mathrm{Wcm^{-2}}$.

The ALPHA-X laboratory system [5] follows the architecture of a typical high power laser system based on CPA Ti:sapphire technology (Figure 3.1). The laser system consists mainly of the following key parts: the oscillator to produce the femtosecond duration laser pulses; a grating based stretcher to increase the laser pulse duration and avoid damage to optics during amplification stage; a regenerative amplifier; three multi-pass amplification stages to increase the laser pulse energy and a grating based compressor to compress to the initial short laser pulse duration.

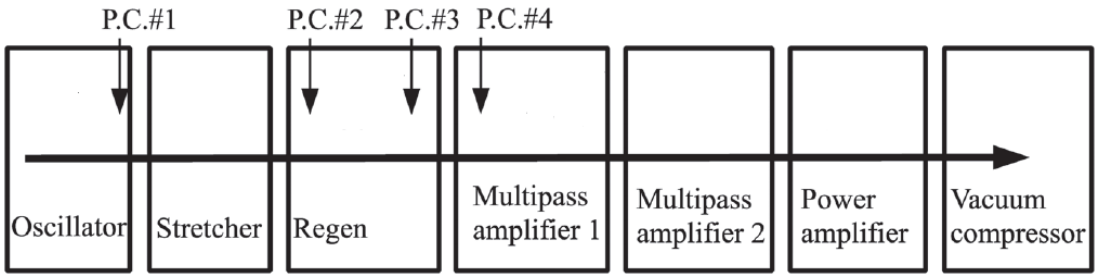

Figure 3.1. Schematic of the architecture of a typical high power laser. P.C. stands for Pockels cell showing the position of the Pockels cells in the laser system.

The essential laser requirements for LWFA experiments are the following:

- High peak intensity (10^{18} $\mathrm{Wcm^{-2}}$ or above).
- Good laser pulse contrast ratio (LPCR), i.e., 10^6 or above.
- A focal spot free from aberrations with a symmetric broad spectrum.

The Ti:sapphire oscillator of the ALPHA-X system operates at ~75 MHz repetition rate and generates laser pulses with a central wavelength of about 800 nm. The initial pulse duration is typically ~20 fs and has a spectral bandwidth of 80-100 nm. To avoid optical damage during amplification the stretcher increases the pulse duration of the laser pulse. The ALPHA-X stretcher negatively chirps and stretches the pulse to ~250 ps duration.

To compensate for the gain narrowing during the different amplification stages, a programmable acousto-optic dispersive filter (Dazzler) [6] is placed after the stretcher to control the spectral phase and amplitude distribution of the laser pulse.

A set of Pockels cells are used through the laser system to isolate the main pulse and to increase the LPCR. The LPCR is defined as the ratio R between the laser pulse peak intensity I_{peak} and any pre-pulse or pedestal intensity I_p:

$$R = \frac{I_{peak}}{I_p}. \tag{3.1}$$

This is an important parameter in LWFA. A low contrast ratio laser pulse can generate a pre-plasma before the arrival of the main laser pulse and change the interaction mechanism between the laser pulse and target [7, 8]. In other

words, if the intensity of the pre-pulse is too high the target can be “destroyed” before the main pulse arrives.

The first Pockels cell is the pulse picker. The pulse picker reduces the laser repetition rate from the MHz range to Hz range. The second Pockels cell is located at the entrance of the regenerative amplifier and it is used to seed it. The third one is also located inside the regenerative cavity. It allows the amplified pulse to exit. The last Pockels cell is located between the regenerative cavity and the first multi-pass amplifier and further reduces the pre-pulse level. The Pockels cells rotate the polarisation of the laser effectively isolating the amplified laser pulse.

The regenerative amplifier provides a high amplification factor of around $10^5 - 10^6$. In the ALPHA-X laser system the energy after the regenerative and pre-amplifier is approximately 15-20 mJ.

The next amplification stage is a (3 pass) multi-pass amplifier pumped by two Nd:YAG solid state lasers (Saga 1 and Saga 2). Each of them used separately amplifies the laser pulse to an energy of 100-150 mJ. When both are used together, the laser pulse energy at this point is around 310-320 mJ and has a bandwidth of 40-45 nm.

After the amplification stage the laser pulse goes through a spatial filter. The spatial filter “cleans” the laser pulse by removing high spatial frequency components (called “hot spots”), which could damage the crystal in the final amplifier. In a spatial filter, a lens focuses the laser pulse. Because of diffraction, laser pulse will not focus to a spot but to an Airy pattern due to the top-hat shape of the laser pulse. A pinhole is placed at the focus position so only the central bright spot passes. Finally, another lens collimates the laser pulse before it passes into the final amplifier.

The final amplification stage increases the laser pulse energy to 1.6 J. This amplifier is pumped by three solid state Nd:YAG pump lasers (Saga 3, Saga 4 and Saga HP1), each typically providing close to 400 mJ in energy.

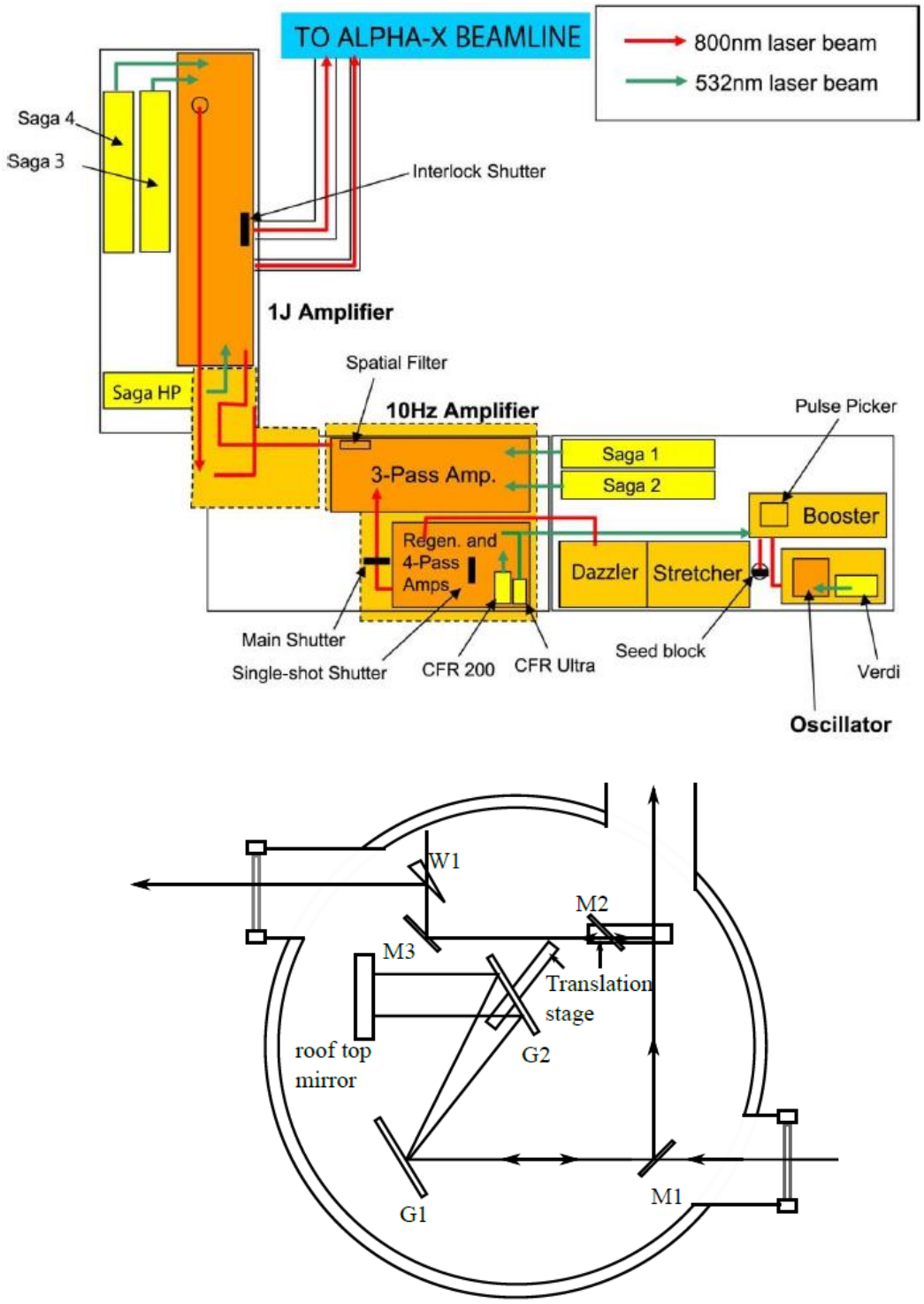

Figure 3.2. Top: schematic of the 10 Hz ALPHA-X laser system. Picture courtesy of Dr Gregor Welsh. Bottom: schematic of the ALPHA-X compressor. The beam is transported to the interaction chamber by mirror M1. The grating G2 is set in a translation stage in order to allow fine adjustment of pulse duration. Mirror M2 can be placed in the beam path and is used to send the laser beam to the auto-correlator. Picture from [9].

The amplification crystals of the laser system are water cooled, except for the final amplifier, which requires cryogenic cooling to avoid thermal lensing.

It is important to note that during this PhD thesis the final amplifier of the ALPHA-X laser system was redesigned and upgraded (in April 2014). A solid state Nd:YAG pump laser has been included in the final amplifier making a total of 4 pump lasers (Saga 3, Saga 4, Saga HP1 and Saga HP 2). Each pump laser amplifies the pulse energy to 400-500 mJ when used separately and up to 2.0 J combined. A schematic of the upgraded final amplifier can be found in Figure (3.4). Moreover, the cryogenic cooling system has been changed to a water cooling system.

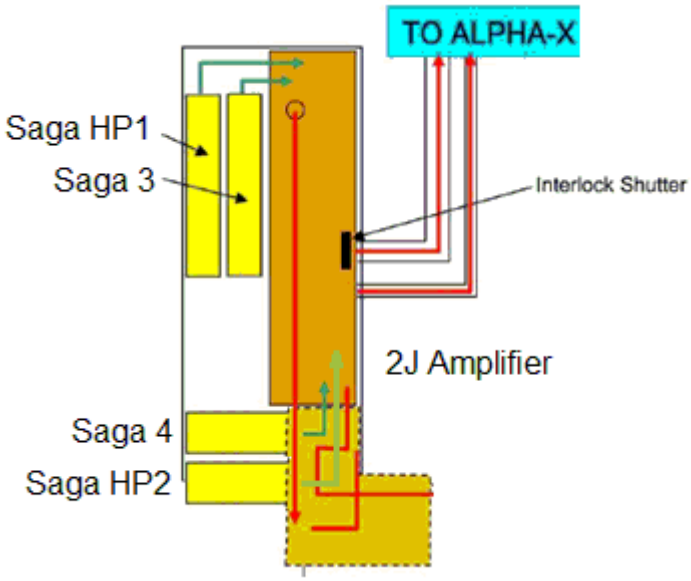

Figure 3.3. Schematic of the ALPHA-X final amplification stage after the upgrade of the laser system in April 2014.

After the amplification stages the laser pulse enters the compressor. The compressor must be kept in vacuum in order to avoid beam quality degradation and power losses caused by nonlinear effects in air. The ALPHA-X compressor is based on parallel gratings that compress the laser pulse to 35-40 fs. The transmission efficiency of the ALPHA-X compressor is around 70%.

After compression the laser pulse enters the interaction chamber situated in a bunker through a series of mirrors in a vacuum pipe. A spherical mirror with a 75 cm focal length focuses the laser pulse onto the gas jet. A Helium-Neon laser is used to align the laser beam.

The energy of the laser pulse on target is around 0.85 J (after laser upgrade this has been increased to 1 J), with a 10% intensity loss from the final amplifier to the compressor, a 30% further loss in the compressor and a 10% loss from the compressor to the gas jet.

3.2 ALPHA-X beam line

All the experiments described in this thesis have been carried out at the ALPHA-X laser wakefield accelerator beam line at the Terahertz to Optical Pulse Source facility at the University of Strathclyde. For this purpose, laser pulses of 800 nm, 0.85 J and 35 fs from a Ti:sapphire laser are focused using a F/18 spherical mirror to a spot diameter of 40 μm $(1/e^2)$ at the entrance of a 2.7 mm diameter pulsed supersonic helium gas jet producing a 10 μm wide relativistic plasma channel. These laser parameters correspond to a peak intensity of $I = 2 \times 10^{18}\,\mathrm{Wcm^{-2}}$ on target. A schematic of the beamline is presented in Figure 3.4.

Both accelerator and diagnostics of the beamline are described in this section.

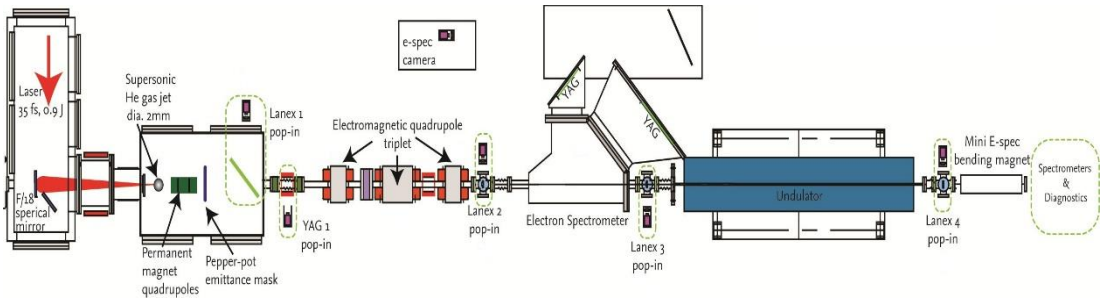

Figure 3.4 Schematic of the ALPHA-X beamline. The main components, i.e., plasma accelerator, beam optics, electron spectrometer, undulator and lanex screens can be seen in the picture.

3.2.1 Supersonic gas jet

Gaseous targets are used in a large number of laser plasma interaction experiments. A helium supersonic gas jet has been used as the plasma accelerator for all the experiments carried out in this thesis. The laser pulse is synchronised to the gas injected by the supersonic gas jet. The nozzle is connected to a pulsed valve that has an opening time of around 3 ms.

The nozzle used in the experiments has been manufactured at the mechanical workshop of the Department of Physics at the University of Strathclyde. It follows an axisymmetric conical De Laval design. A schematic of nozzle and valve can be seen in Figure 3.5. The nozzle has been designed by Dr Constantin Aniculaesei and more detail can be found in his PhD thesis [10]. The throat of this nozzle and the exit have a diameter of approximately 0.50 mm and 3.0 mm, respectively. The gas valve is a Parker valve. Further information about it can be found in [11].

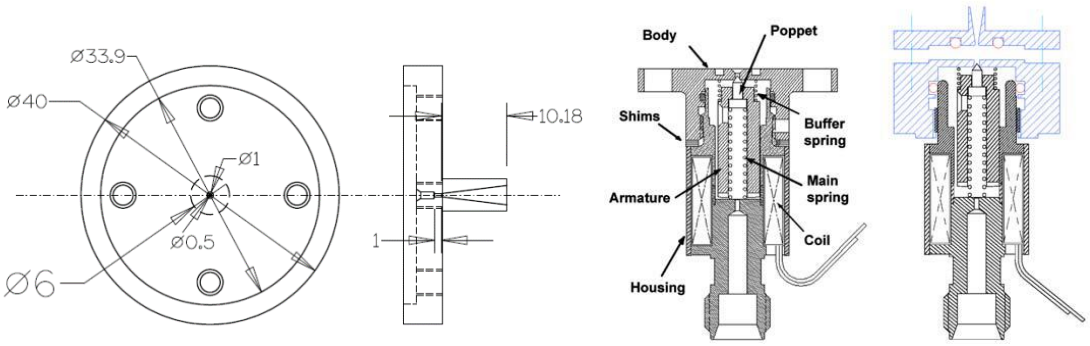

Figure 3.5. Left: Dimensions of the nozzle 511 used in the experiments performed for this thesis (in mm). Right: Schematic of the Parker valve set up in the ALPHA-X chamber.

In the experiments performed for this thesis, the distance between nozzle and laser, *i.e.* the height, was 2 - 4.5 mm and the backing pressure ranged from 25 to 50 bar. Please note that throughout this thesis the y axis represents height from nozzle exit, z is the laser propagation axis and x represents the direction transverse to the laser propagation axis observing the nozzle from a top view. The laser is polarised in the horizontal (xz) plane. For these backing pressures and for He gas jets, the plasma density is of the order of $1 - 3 \times 10^{19}\ \mathrm{cm}^{-3}$.

An important parameter in LWFA experiments is the plasma density. It is not an easy task to estimate this quantity. One option for a direct measure of the plasma density is to use interferometric techniques, which are very sensitive because very small differences in the optical path length can be measured.

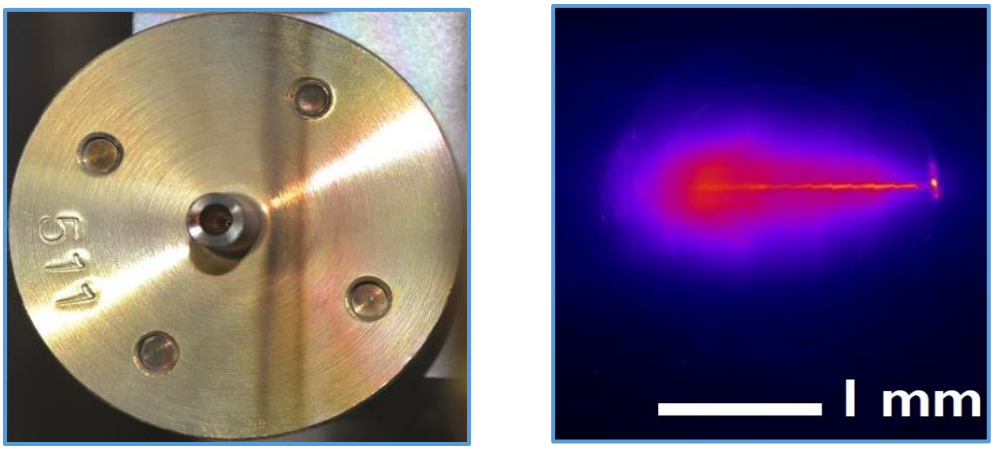

Figure 3.6. Left: picture of the nozzle 511 used in this thesis. Right: example of laser-induced plasma channel at 4.0 mm from the nozzle exit and backing gas pressure of 50 bar.

A second option to estimate the densities is to use computational fluid dynamics simulations (CFD) to simulate the gas flow for the nozzle used in the experiments.

The commercial software ANSYS Fluent 15 is used for CFD simulations. ANSYS Fluent solves the mass and momentum conservation equations for all flows on a grid using a finite volume method [12]. These equations can be written as follows:

$$\frac{\partial \rho}{\partial t} + \nabla \cdot (\rho \bar{v}) = S_m \tag{3.2}$$

$$\frac{\partial (\rho \bar{v})}{\partial t} + \nabla \cdot (\rho \bar{v}\, \bar{v}) = -\nabla p + \nabla \cdot (\bar{\tau}) + \rho \bar{g} + \bar{F} \tag{3.3}$$

$$\frac{\partial}{\partial t}(\rho E) + \nabla \cdot (\bar{v}\,(\rho E + p)) = -\nabla \cdot \left(\sum_j \left(h_j J_j \right) \right) + S_h. \tag{3.4}$$

Eq (3.2) is the general form of the mass conservation equation and is valid for both compressible and incompressible flows. S_m is the mass added to the continuous phase from the dispersed second phase. This term equals zero in our case.

Eq (3.3) represents the conservation of momentum in an inertial reference frame. Here p is the static pressure, $\rho \bar{g}$ the gravitational body force and $\bar{F}$ the external body forces. τ is the stress tensor given by:

$$\bar{\tau} = \mu\left[(\nabla\bar{v} + \nabla\bar{v}) - \frac{2}{3}\nabla\cdot\bar{v}I\right], \quad (3.5)$$

where μ is the viscosity and I the unit tensor.

Eq (3.4) is the energy conservation equation where h_j is the enthalpy, J_j is the diffusion flux of species *j* and S_h is a heat source term (zero in our case).

Simulations use the Shear-Stress Transport (SST) k-omega model. Further information about CFD simulations and FLUENT 15 software can be found in Dr Constantin Aniculaesei PhD thesis [11].

The following figures show density profiles obtained from CFD simulations in FLUENT 15 using the nozzle 511 geometry showed in Figure 3.5. Most of the measurements for this thesis have been performed between 1.5 mm and 4.0 mm from nozzle exit.

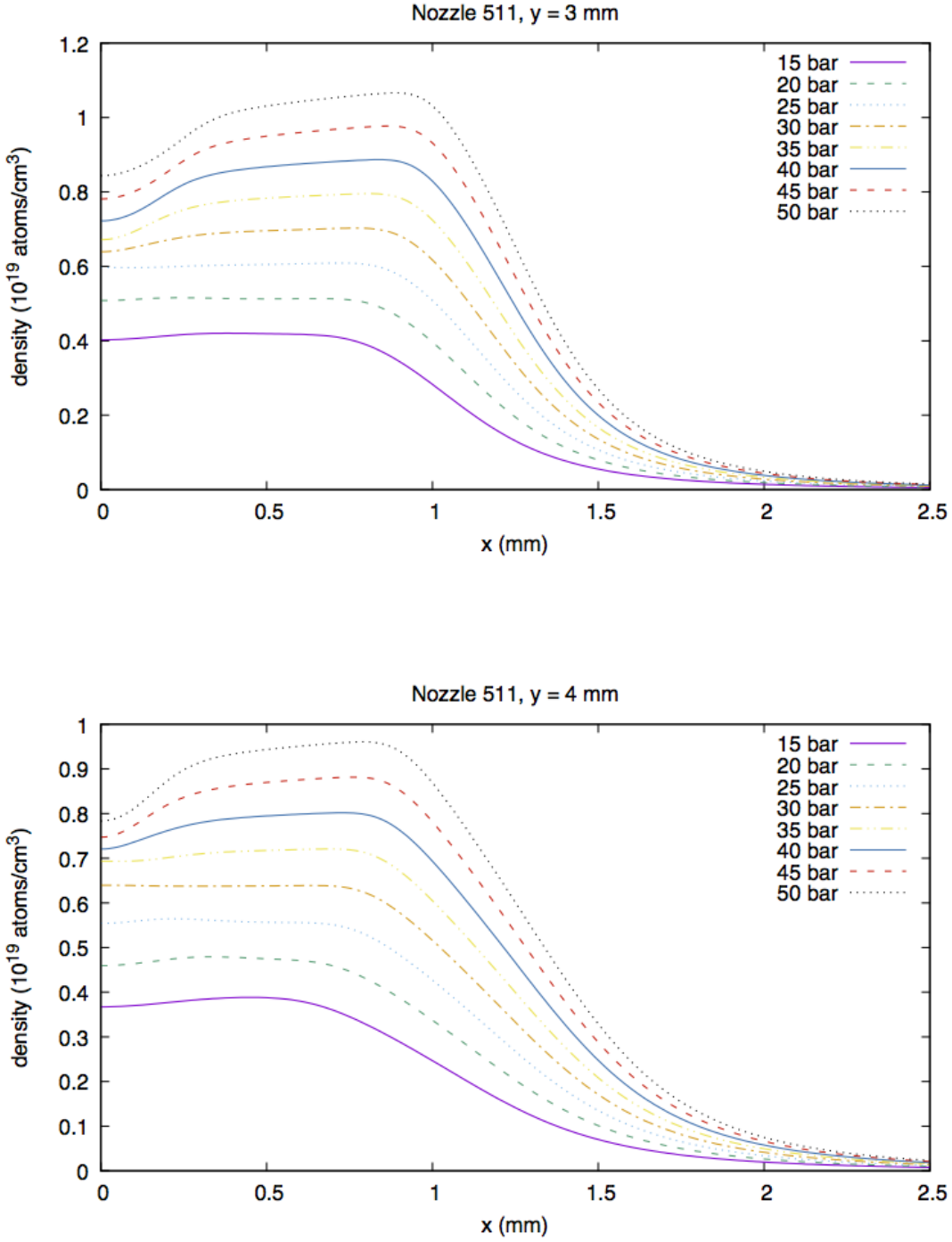

Figure 3.7. Top: density profiles of half of nozzle 511 for different backing pressures at 3 mm height from nozzle exit (simulations and Figure courtesy of Dr Enrico Brunetti). Bottom: density profiles of half of nozzle 511 for different backing pressures at 4 mm height from nozzle exit (simulations and Figure courtesy of Dr Enrico Brunetti). X=0 corresponds to the centre of the nozzle.

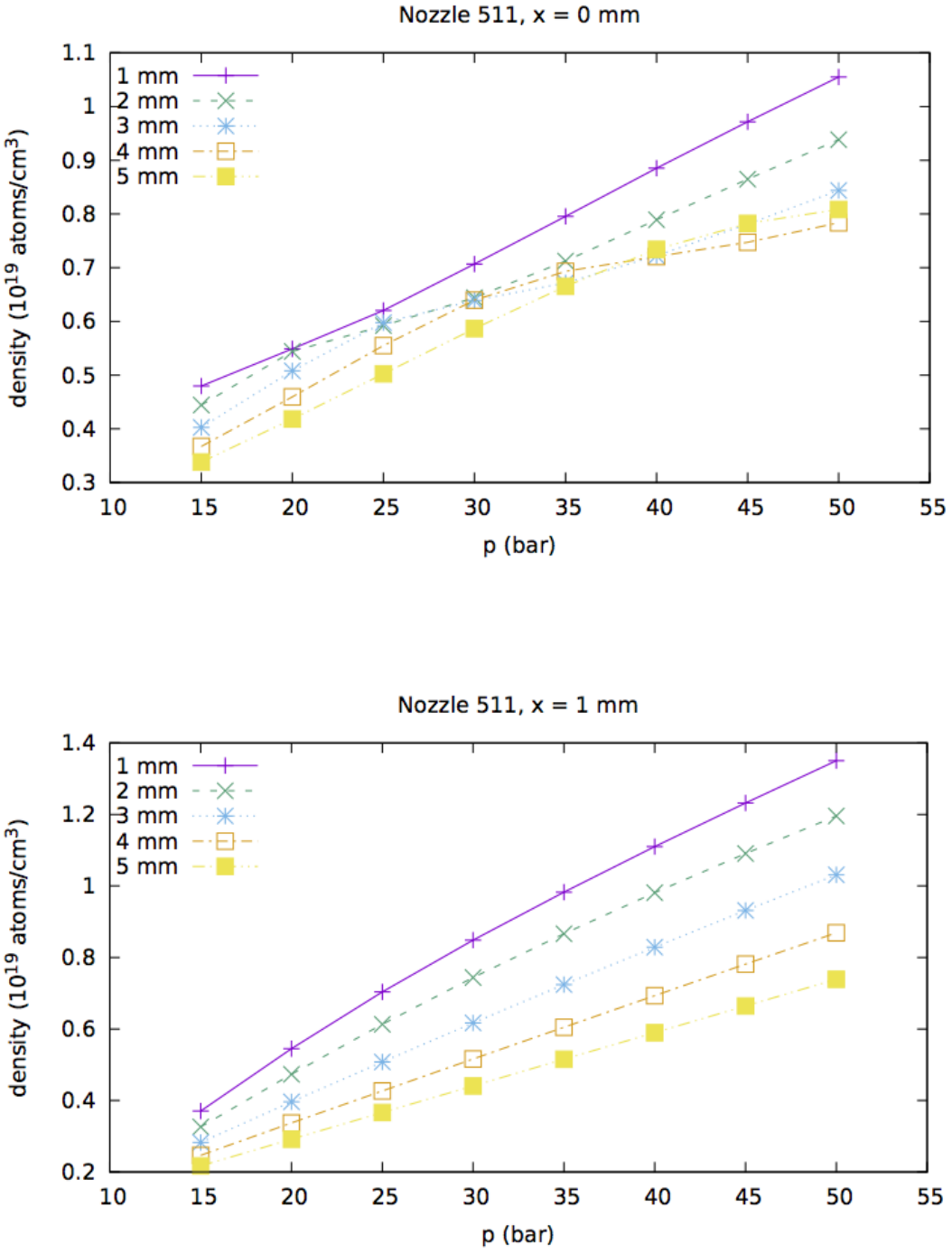

Figure 3.8. Top: density values for nozzle 511 for different backing pressures and heights from nozzle exit at nozzle centre (simulations and Figure courtesy of Dr Enrico Brunetti). Bottom: Density values for nozzle 511 for different backing pressures and heights from nozzle exit at 1 mm from nozzle centre along the x axis (simulations and Figure courtesy of Dr Enrico Brunetti).

3.2.2 Imaging plates for electron charge measurements

Imaging plates (IPs) are photo-sensitive devices that can detect ionising radiation such as X-rays. Their use as X-ray imaging detectors is widespread, particularly in applications such as materials testing and medical diagnostics. Their main advantages are their complete immunity to electromagnetic interferences and large dynamic range.

Normally, the sensitive layer of the IPs is made of BaF(Br,I):Eu^{2+}. When X-rays or other ionising radiation reach this layer, Eu^{2+} atoms lose one electron becoming Eu^{3+}. These electrons stay in the conduction band in an F-centre metastable state. The total number of F-centres is proportional to the energy of the incident radiation. Spontaneous recombination of metastable electrons with Eu^{3+} atoms can occur in a process known as fading [13], depending only on the environmental temperature, the type of IP and on the time elapsed since the irradiation. This effect must be taken into account before reading as the output must be kept as constant as possible.

After X-ray exposure the IP plates are read out by inducing recombination of electrons using a narrow laser beam. This recombination produces photons in a process known as photo-stimulated luminescence (PSL), which can be easily recorded using photo-multiplier tubes. IPs can be reused by erasing them with UV light.

In previous experiments [14-16], IPs have been calibrated for use in measuring high energy electrons that are generated by the interaction of high intensity laser pulses with solid, plasma or gas targets. IPs are also used to detect high energy protons and photons [17, 18].

The process of measuring the charge from an electron beam used in this thesis is the following:

1. After the IP (Fujifilm BAS-SR model) has been irradiated it is read out using a Fujifilm FLA700 reader, which uses a magnetic tray to hold the IP and a $\lambda = 650$ nm solid state readout laser. Arbitrary size plates can be scanned.

2. Images are saved in a logarithmic grayscale (known as a quantum level) image and converted into physical PSL units using the following equation [18]:

$$PSL = \left(\frac{R}{100}\right)^2 \times \frac{4000}{S} \times 10^{L\left(\frac{Q_L}{G}-\frac{1}{2}\right)} \tag{3.6}$$

where $L = 5$ is the latitude, $R = 50$ is the resolution, $S = 1000$ the sensitivity, $G = 65535$ the bit depth for 16 bits and Q_L the logarithmic grayscale value.

3. The PSL value is corrected by the fading. As previously mentioned the fading was studied by Meadowcroft *et al.* [13]. The fading correction factors are shown in Figure 3.9:

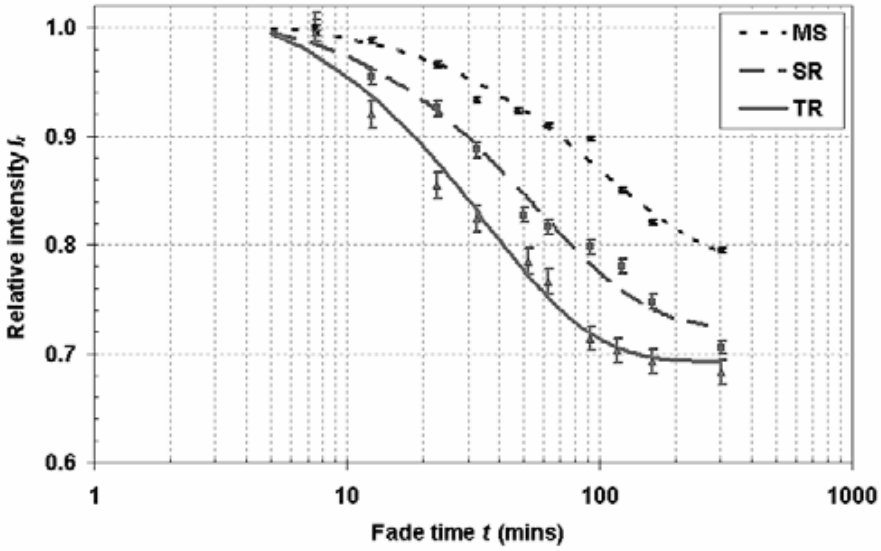

Figure 3.9. Fading of the Fuji BAS IP as a function of time. From [13].

4. From the PSL value the total charge can be estimated using the calibration value of $0.0064 PSL/\text{electron}$ valid for the electron energy range produced in the experiments carried for this work (80-160 MeV) [16].

One important consideration in the use of the IPs is how the number of scans performed affect the IP response. In Figure 3.10 it can be observed that every

time an IP is read the number of counts observed is reduced, a fact that must be taken into account in order not to underestimate the number of counts. Concretely, if after scanning the irradiated IP it is necessary to perform further scans a correction factor which can be extracted from Figure 3.10 must be applied. Roughly, every time an IP is read, the number of counts is reduced by a factor of 1.02 ± 0.01. This measurement has been performed by the author. For this, an IP was irradiated with electrons produced at the ALPHA-X beam line and scanned several times to infer the correction factor with the number of scans.

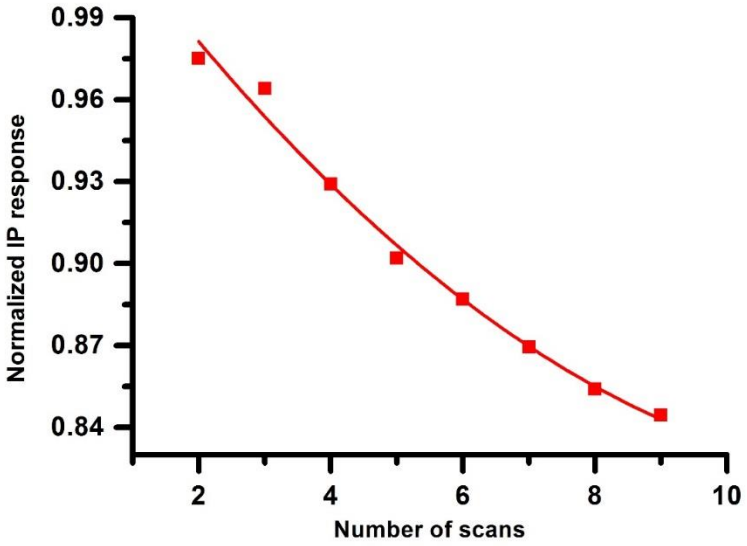

Figure 3.10. Evaluation of the number of scans correction on the Fuji BAS IP-SR model response.

Another important consideration is its energy dependence. Chen *et al.* [15] studied this effect in the energy range of 100 keV - 4 MeV. Tanaka *et al.* [14] looked at a higher energy range up to 100 MeV and Nakanii *et al.* [16] studied this effect up to 1 GeV electron beam energy (Figure 3.11).

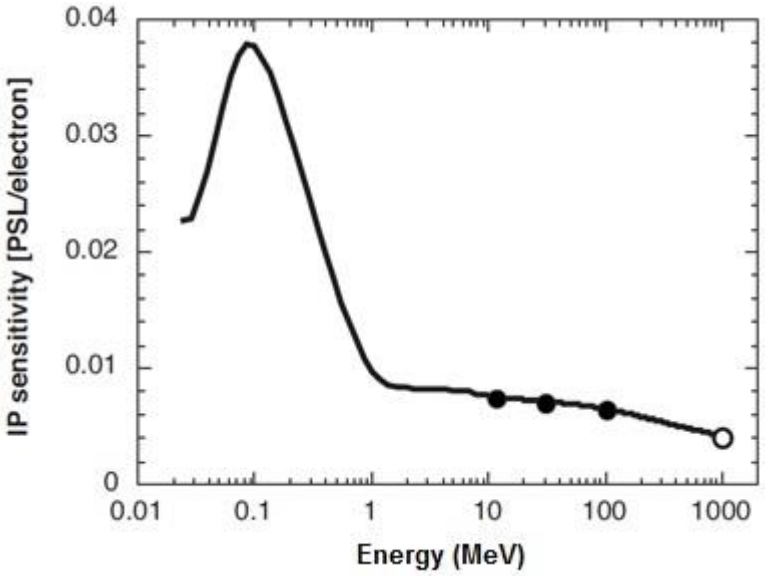

Figure 3.11. Calibrated sensitivity curve for electrons up to 1 GeV energy from [16]. The sensitivity up to 100 MeV has been plotted using the data from reference [14].

The energy of the electron beam generated in the ALPHA-X laboratory is in the 70-180 MeV range. As it can be seen from Figure 3.11 the correction factor for this energy range is minimum.

3.2.3 Electron beam profile scintillators: Lanex screens

Lanex screens are used in the ALPHA-X beamline to monitor the transverse properties of the electron beam in different positions of the beam line. The location of all the lanex screens of the ALPHA-X beam line can be seen in Figure 3.4.

A Lanex screen is a scintillating screen that emits light in the green part of the visible spectrum when ionising radiation interacts with it. The resolution of this kind of screens has been measured for the fine and medium grain thickness screens as 40 and 76 μm respectively [19]. The Lanex (KODAK) screen is a thallium doped caesium iodide (CsI:Tl) grown in a columnar "needle-like" structure.

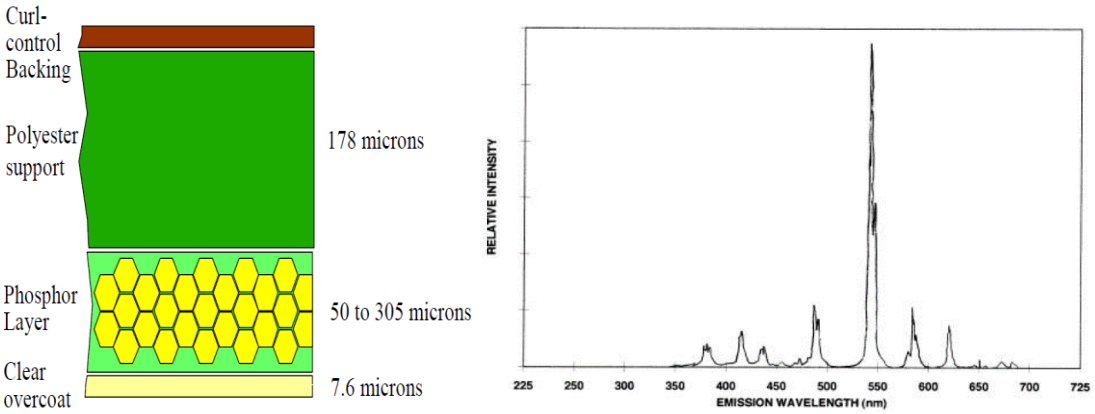

Figure 3.12. Left: composition of a typical scintillating Lanex screen. The thickness of the phosphor layer depends on the Lanex type. Right: Spectrum of the light emitted by the Lanex Fast model by Kodak. It can be seen that the most intense emission is around a wavelength of 550 nm.

In this work, the lanex screens used are identified as Lanex 1 and Lanex 2. Lanex 1 is the first beam profile monitor. It is placed at the end of the acceleration chamber at a distance of 64 cm from the gas jet, as can be seen in Figure 3.4. The accelerator is optimised by observing the quality of the electron beams on this screen. One pixel corresponds to 40 and 30 μm along the x and y axis respectively.

Lanex 1 is mounted in a manual sliding pipe through a vacuum feed-through that allows the screen to be inserted into the beam line axis for electron beam monitoring, and can be retracted to allow the electron beam to travel down the beam line. The screen is positioned at 45º to the laser beam axis. Lanex 1 is observed from behind through a Perspex window with a CCD camera. When a laser interacts with a lanex screen this emits light, which interferes with electron beam monitoring. To solve this problem, lanex 1 is shielded by a layer of aluminium foil, which blocks the laser light preventing saturation of the CCD camera.

Lanex 2 is mounted in a cross-piece after the electromagnetic quadrupoles (Figure 3.4). This screen is mounted normal to the beam line and a mirror is placed behind it at 45º. The screen can be inserted and retracted from the beam line using a pneumatic feed-through (pop-in in Figure 3.4), which can be controlled from the control room.

There are two more Lanex screens in the ALPHA-X beam line: Lanex 3 and Lanex 4. Lanex 3 is used to monitor the electron beam at the entrance of the undulator and lanex 4 is used to monitor the beam after the undulator. These two screens have not been used in the experiments carried out for this thesis.

An extra lanex screen (new lanex) has been installed in the accelerating chamber to perform experiments related to this thesis. More details on this new lanex screen are given in Chapter 4.

All the lanex screens used in the ALPHA-X beam line are observed using 12 bit Point Grey Research Flea cameras with Edmund Optic objectives.

3.2.4 Electromagnetic quadrupoles

The typical electron beam energy in the ALPHA-X beam line is of the order of 120 MeV, which is highly relativistic. Magnets can be used to bend, steer and focus the electron beam. Quadrupole magnets consist of four magnets designed in a way that the dipole terms cancel out in the planar multipole expansion, therefore the lowest significant terms in the field equations are quadrupole.

There are two types of quadrupoles:

- F quadrupoles: which are horizontally focusing but vertically defocusing.
- D quadrupoles: which are vertically focusing but horizontally defocusing.

It is important to note that it is impossible for a quadrupole to focus in both horizontal and vertical planes at the same time.

Figure 3.13 shows a schematic of a quadrupole. This example focuses a positive charged particle travelling to the image plane in the vertical direction (forces above and below the centre point towards the centre) while defocusing in the horizontal direction (forces left and right of the centre point away from the centre).

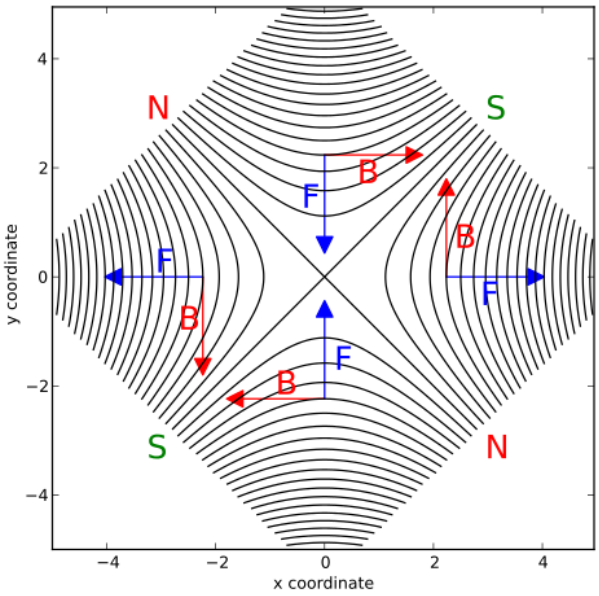

Figure 3.13. Magnetic field lines of an ideal quadrupole. The red arrows show the direction of the magnetic field while the blue arrows show the direction of the Lorentz force on a positive particle. Picture courtesy of Dr Andre Holzner.

If a type F quadrupole and a D type quadrupole are positioned together the fields cancel out completely. However, if both are placed within a certain separation and this separation is properly designed the overall effect is focusing in both horizontal and vertical planes. This allows quadrupoles to be used to transport particle beams over long distances (such as in synchrotrons or for LWFAs as in the ALPHA-X beam line).

There are two sets of magnetic quadrupole triplets in the ALPHA-X beam line: the permanent magnetic field quadrupoles (PMQs) and the dynamic electromagnetic quadrupoles (Figure 3.4).

The PMQs are placed in the accelerator chamber several centimetres from the gas jet (along the z axis). This is a very compact magnetic quadrupole triplet, with an aperture of 6 mm. The drift distances between the PMQs can be adjusted between 1.5 and 5 cm to optimise transport at different energies. They have been installed in the chamber for two reasons:

- To reduce the divergence of the electron beam just after the accelerator.
- To improve the pointing stability and also to act as an energy filter removing the low energy component of the electron bunch produced, since this component is strongly over focussed. The spatial profiles may be slightly distorted due to the energy spread and the energy dependence of the PMQs focusing strength.

The second triplet set of quadrupoles, *i.e.* the dynamic electromagnetic quadrupoles, are mounted after the accelerator chamber and in front of the electron spectrometer, as shown in Figure 3.4. The magnetic fields in these quads are controlled by the current passing through their coils and can be fully adjusted to suit the requirements of the electron beam. The dynamic electromagnetic quadrupoles are used to optimise electron beam transport for electron spectrometer measurements.

3.2.5 *Electron spectrometer*

The energy of the electron beam produced at the ALPHA-X beam line is measured using an electron spectrometer designed by Dr Allan Gillespie and manufactured by SigmaPhi [20]. The electron spectrometer is placed 2.56 m after the gas jet. It has a magnetic strength up to 1.7T.

When the electromagnets are switched on, the electrons are bent out of the beam line at an angle that depends on the energy. Therefore, by measuring the deflection of the electron beam, the energy spectrum can be monitored. The radius of the orbit of an electron deflected by a magnetic field is given by:

$$r = \frac{\gamma m_0 c}{eB} \cong \frac{3.34 E_0[\mathrm{MeV}]}{B[\mathrm{T}]}, \tag{3.7}$$

therefore:

$$E_0[\mathrm{MeV}] = \frac{r[\mathrm{mm}]B[T]}{3.34}, \tag{3.8}$$

where $m_0\gamma$ is the electron relativistic mass, E_0 the energy of the electron beam, B the strength of the magnetic field and r the radius of the orbit described by the electrons.

The ALPHA-X electron spectrometer follows a Browne–Buechner design [21] in order to provide a strong focusing in both horizontal and vertical planes. This guarantees high energy resolution over a wide range of energies.

The electron spectrometer has two operating modes: high resolution mode and high energy mode. The high resolution mode uses a high field strength to bend the electrons through approximately 90º with relatively narrow bandwidth, and high resolution imaging at the focal plane. This mode is restricted to an energy less than 105 MeV. Since the electrons are bent through a large angle the energy resolution is very high (around 0.1%).

The high energy mode allows for wide bandwidth at the expense of a lower resolution. In this mode, it is possible to image beams with energies up to 657 MeV. However, the energy resolution is much lower than in the first mode (between 1-10%). A Lanex scintillating screen positioned at the focal plane is used to image electrons exiting the spectrometer and the image is captured on a 14 bit Grasshopper CCD camera. Electron energy is estimated after background subtraction. For this purpose, a first image without laser shot is always recorded before each run. An example of electron beam spectra recorded on the electron spectrometer can be seen in the following Figure:

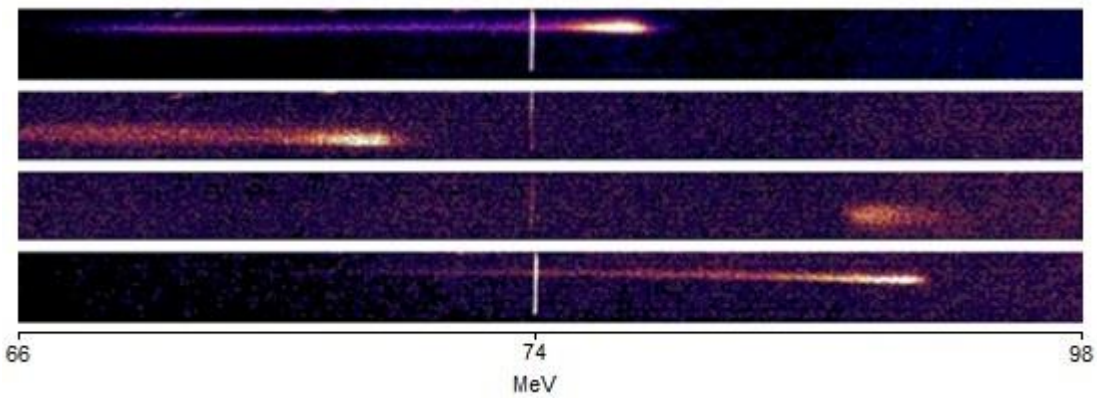

Figure 3.14. False colour images of four electron beam spectra recorded using the ALPHA-X electron spectrometer. The energy range shown is from 66 to 98 MeV from left to right. From [20].

Chapter references:

1. Strickland, D. and G. Mourou, *Compression of amplified chirped optical pulses.* Optics Communications, 1985. **55**(6): p. 447-449.
2. Moulton, P.F., *Spectroscopic and laser characteristics of Ti: Al2O3.* JOSA B, 1986. **3**(1): p. 125-133.
3. Zhidkov, A., et al., *Radiation damping effects on the interaction of ultraintense laser pulses with an overdense plasma.* Physical Review Letters, 2002. **88**(18): p. 185002.
4. Gerstner, E., *Laser physics: Extreme light.* Nature, 2007. **446**(7131): p. 16-18.
5. Jaroszynski, D.A., et al., *The Strathclyde terahertz to optical pulse source (TOPS).* Nuclear Instruments and Methods in Physics Research Section A: Accelerators, Spectrometers, Detectors and Associated Equipment, 2000. **445**(1–3): p. 317-319.
6. Tournois, P., *Acousto-optic programmable dispersive filter for adaptive compensation of group delay time dispersion in laser systems.* Optics Communications, 1997. **140**(4): p. 245-249.
7. Zhidkov, A., et al., *Prepulse effects on the interaction of intense femtosecond laser pulses with high-Z solids.* Physical Review E, 2000. **62**(5): p. 7232.
8. Workman, J., et al., *Picosecond soft-x-ray source from subpicosecond laser-produced plasmas.* JOSA B, 1996. **13**(1): p. 125-131.
9. Shanks, R., *Comprehensive characterisation of laser plasma wakefield accelerated electrons.* Ph.D. thesis, University of Strathclyde, 2012.
10. Aniculaesei, C., *Experimental studies of laser plasma wakefield acceleration.* Ph.D. thesis, University of Strathclyde, 2015.
11. www.parker.com
12. Versteeg, H.K. and W. Malalasekera, *An introduction to computational fluid dynamics: the finite volume method*. 2007: Pearson Education.
13. A. L. Meadowcroft, C.D.B., E. N. Stott, *"Evaluation of the sensitivity and fading characteristics of an image plate system for X-ray diagnostics".* Review of Scientific Instruments, 2008. **79**: p. 113102.

14. K. A. Tanaka, T.Y., T. Sato, R. Kodama, Y. Kitagawa, T. Takahashi, T. Ikeda, Y. Honda, S. Okuda, *"Calibration of imaging plate for high energy electron spectrometer".* Review of Scientific Instruments, 2004. **76**: p. 013507.
15. H. Chen, N.L.B., T Bartal, F. N. Beg, D. C. Eder, A. J. Link, A. G. MacPhee, Y. Ping, P. M. Song , A. Throop, L. Van Woerkom, *"Absolute calibration of image plates for electrons at energy between 100 keV and 4 MeV".* Review of Scientific Instruments, 2007. **79**: p. 033301.
16. N. Nakanii, K.K., T. Yabuuchi, K. Tsuji, K. A. Tanaka, S. Suzuki, T. Asaka, K. Yanagida, H. Hanaki, T. Kobayashi, K. Makino, T. Yamane, S. Miyamoto, K. Horikawa, *"Absolute calibration of imaging plate for GeV electrons".* Review of Scientific Instruments, 2008. **79**: p. 066102.
17. A. Mančić, J.F., P. Antici, S. A. Gaillard,P. Audebert, *"Absolute calibration of photostimulable image plate detectors used as (0.5–20 MeV) high-energy proton detectors".* Review of Scientific Instruments, 2008. **79**: p. 073301.
18. B. R. Maddox, H.S.P., B. A. Remington, N. Izumi, S. Chen, C. Chen, G. Kimminau, Z. Ali, M. J. Haugh, Q. Ma, *"High-energy x-ray backlighter spectrum measurements using calibrated image plates".* Review of Scientific Instruments, 2011. **82**: p. 023111.
19. Jing, T., et al. *Evaluation of a structured cesium iodide film for radiation imaging purposes*. in *Nuclear Science Symposium and Medical Imaging Conference, 1993., 1993 IEEE Conference Record.* 1994. IEEE.
20. Wiggins, S.M., et al., *High quality electron beams from a laser wakefield accelerator.* Plasma Physics and Controlled Fusion, 2010. **52**(12): p. 124032.
21. Browne, C. and W. Buechner, *Broad-Range Magnetic Spectrograph.* Review of Scientific Instruments, 1956. **27**(11): p. 899-907.

Chapter 4: Laser-driven X-ray phase contrast imaging

4.1 Laser-driven X-ray phase contrast imaging

As pointed out in Chapter 2 of this thesis, electrons in the LWFA can undergo transverse oscillations and emit synchrotron-like (betatron) radiation into a narrow cone around the propagation axis. The properties of the betatron radiation produced by LWFA make it an excellent candidate for X-ray phase contrast imaging (XPCi). Betatron radiation is bright and spatially coherent [1].

The first measurements of betatron radiation emitted by a LWFA were reported by Rousse *et al.* [2] in 2004, when the authors measured a maximum energy of few keV (1-10 keV). A few years later Kneip *et al.* [3] reported an X-ray source with 10 times higher energy than the source reported by Rousse *et al.* This was made possible by operating the LWFA in the bubble regime. More recently, Cipiccia *et al.* [4] demonstrated experimentally and theoretically that interaction of electrons with the laser pulse can resonantly amplify the betatron motion. This leads to an increase in the energy of the emitted photons, which can extend to several MeV [4].

XPCi requires a source with a high level of spatial coherence. Before the development of the LWFA technology, this high level of spatial coherence was only achievable in synchrotron facilities or alternatively using interferometric techniques, which required expensive optics. The micrometer-sized source of the betatron radiation [4] guarantees a high level of spatial coherence that is required for XPCi.

The first experimental demonstration of betatron radiation was soon followed by the first XPCi measurements using the betatron source from a LWFA. The first X-ray phase contrast images using this source were performed by Kneip *et al.* [5]. A few years later, single-shot laser driven phase contrast images were demonstrated by Fourmaux *et al.* [6].

In this Chapter, the characterisation of the main properties of the ALPHA-X betatron source is presented and the properties of the detectors used are described. The source is then used to produce X-ray phase contrast image of a biological specimen using an in-line phase-contrast imaging technique.

In the second part of this Chapter further betatron source measurements are presented (performed after the upgrade of the ALPHA-X laser). The source is then used to obtain microscopy images of very thin wires with unprecedented quality and resolution. Several projections of a micrometer-size object and the discussion of the use of the betatron radiation as a source for XPCi tomography is presented in this section.

The analysis of the results and the equipment used for each experiment are described in the corresponding sections. Finally, conclusions and summary of results are given in the last section of this Chapter.

4.2 Basic concepts of X-ray phase-contrast imaging

4.2.1 Introduction

X-ray phase contrast imaging (XPCi) represents an elegant solution to maximize the resolution while minimizing the X-ray dose delivered. XPCi was developed mainly in the 90s. It is a promising technique that has attracted the attention of the scientific community.

The main principle of phase contrast imaging was first developed by Frits Zernike [7, 8] while working with diffraction gratings and visible light. A further step to take phase contrast from visible light to X-rays did not happen until the 1970s with the huge improvement of the quality of the X-ray beams from synchrotrons. X-ray sources from synchrotrons are more intense and versatile than X-rays produced by conventional X-ray tubes. Both the construction of synchrotron facilities and the progress in the development of X-ray optics were fundamental for the development of XPCi.

In 1965 Ulrich Bonse and Michael Hart at the Department of Materials Science and Engineering of Cornell University developed a crystal interferometer [9]

applying, for the first time, Zernike's phase contrast method to X-rays. 30 years later the Japanese scientists Atsushi Momose and Tohoru Takeda used the XPCi method to image biological soft tissues samples [10, 11] at the National Laboratory for High Energy Physics in Tsukuba (Japan), connecting XPCi to biomedical imaging.

Several phase contrast imaging configurations have been developed mainly at synchrotron facilities. All these configurations will be reviewed in detail in the next section.

The application of phase contrast imaging techniques in biological imaging has been held back by the limited number of appropriate X-ray sources. Some configurations demand X-ray beams with high transverse or longitudinal coherence. XPCi configurations such as grating interferometry [12] or propagation-based phase contrast imaging require a set up where the sample "sees" a small X-ray source, which is obtained when the coherence length, $L_{coh} = \lambda R/s$, is larger than the detail to be imaged (where λ is the wavelength, s the source size and R is the source to observation distance). On the other hand, both techniques have the advantage that polychromatic radiation may be used without significant loss of contrast [13].

In analysing-based imaging [14] and crystal interferometry the transverse coherence is not crucial but the angle of deflection introduced by the crystal is energy-dependent. This implies an increased imaging time compared with techniques using polychromatic X-rays.

Conventional X-ray sources can generate beams with a high transverse or longitudinal coherence. However, this can only be done at the cost of increasing the exposure time, which becomes too long for applications such as clinical imaging.

Highly coherent beams are available at synchrotron facilities, where most of the progress in the development of XPCi has been carried out. Some examples of the last third generation of synchrotron facilities are Alba, SOLEIL, Diamond,

ESRF or Elettra[1]. In these facilities, light pulses with peak brilliances of the order of 10^{24}-10^{25} ph/s/mm^2/mrad^2/0.1%BW and average brilliance of 10^{21} ph/s/mm^2/mrad^2/0.1%BW can be produced. The brilliance is defined as the flux of photons divided by the emittance. The emittance is a measure of the beam distribution in the transverse phase space. Moreover, fourth generation synchrotron light sources (such as linac-based free-electron lasers FELs) increase the average brilliance by four or five orders of magnitude and the peak brilliance by ten orders or magnitude.

As mentioned before, the main challenge is that access to beam time at these facilities is very limited due to high demand. Another disadvantage is that, apart from limited clinical research, these large facilities are not suitable for clinical practice. These two reasons stimulated scientists to start investigating “table-top” solutions to find alternatives to both conventional sources and large scale synchrotron and FEL facilities.

The first solution is the use of light sources such as mini-synchrotrons. In this technology, a circulating electron beam of 10 MeV interacts with a solid target emitting bremsstrahlung in the forward direction [15]. Grating interferometry and propagation based phase contrast imaging has already been demonstrated using this technology [16].

The second option is based on inverse Compton scattering. In this configuration, a laser pulse is backscattered to produce hard X-rays as the electron beam from a small storage ring or linear accelerator (LINAC) interacts with it. When the electron beam interacts with the laser pulse it oscillates in its periodic electromagnetic field and emits narrow band synchrotron radiation. The radiation is emitted in a cone of a few mrads, with a pulse interval of 10 ns and an energy bandwidth of around 1% (depending on the laser pulse length and its bandwidth). Several facilities of this kind are being commissioned and their performance is expected to be similar to large synchrotrons. XPCi configurations such as grating interferometry and

[1] *Source optimisée de lumière d’énergie intermédiaire du LURE (SOLEIL), European Synchrotron Radiation Facility (ESRF).*

propagation based phase contrast imaging methods have been already demonstrated using inverse Compton scattering sources [17, 18].

The third and most promising table-top solution is the laser wakefield accelerator which has been described in chapter 2.

Progress has also been made with incoherent sources. Particularly promising is the coded-aperture method developed by Olivo and collaborators [19], which uses a conventional X-ray tube. This technique produces phase contrast images similar to the ones obtained with synchrotron radiation but using conventional X-ray sources.

4.2.2. XPCi basic concepts

This section reviews the main aspects of XPCi and is mainly based on reference [20]. In conventional X-ray absorption imaging, the contrast arises from the difference in the X-ray attenuation coefficients of different materials. The attenuation contrast, C_{att}, is defined as:

$$C_{att} = \frac{I_1 - I_2}{I_1}, \tag{4.1}$$

where I_1 and I_2 are the intensities of X-rays transmitted in the shadow of the detail and the intensity transmitted outside it, respectively. Introducing the Beer-Lambert's law into equation 4.1 yields:

$$C_{att} = 1 - e^{[(\mu_1 - \mu_2)t_2]}, \tag{4.2}$$

where μ_1 and μ_2 are the attenuation coefficients of the background and the detail respectively, and t_2 is the thickness of the detail. Considering equation 4.2 one can see that if the attenuation coefficients are similar or the thickness of the detail is small the contrast will also be small.

X-ray phase-contrast imaging is based on different physics. The complex refractive index n can be defined as follows:

$$n = 1 - \delta + i\beta, \tag{4.3}$$

where δ is related to the phase shift ϕ that the X-rays experience when going through a material, $i = \sqrt{-1}$ and β is the attenuation coefficient of the material given by:

$$\mu = \frac{4\pi\beta}{\lambda}, \tag{4.4}$$

where λ is the wavelength of the X-rays.

The phase shift that an X-ray experiences when going through a material is given by:

$$\Phi(x, y) = \frac{2\pi}{\lambda} \int_{t_1}^{t_2} \delta(x, y, z) dz, \tag{4.5}$$

Where z corresponds to the direction of propagation of the X-ray wave and the integration is carried out over the thickness of the material in the direction of propagation of the X-ray wave, *i.e.* z.

δ can be written as:

$$\delta = \frac{r_e \rho_e \lambda^2}{2\pi}, \tag{4.6}$$

where r_e is the classical electron radius and ρ_e is the electron density of the material.

δ and β have different dependencies with the X-ray energy as can be seen in Figure 4.1. For most biological tissues, and in the 40-150 keV energy range used for clinical medical imaging, δ is around 1000 times larger than β. This results in high contrast, enabling the detection of details that are invisible to conventional absorption techniques, as will be discussed below.

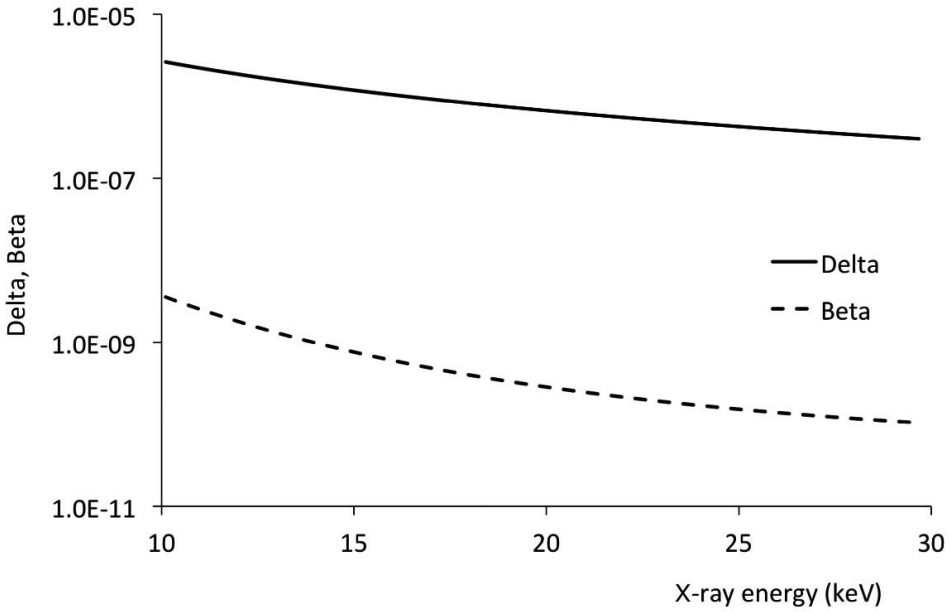

Figure 4.1. δ and β dependency on the X-ray energy for PMMA (often used as a tissue substitute in phantoms because its properties are similar to water). From [20].

Moreover, this high contrast could potentially reduce the dose delivered to a patient during medical imaging diagnosis (i.e. CT scan, mammography, angiography, etc.) allowing an increase of the number of imaging diagnostics used on patients (since each diagnostic has to be clinically justified).

Depending on the XPCi technique used, the contrast in XPCi can be obtained from single or double pairs of dark and bright fringes (*i.e.* an interference pattern). Therefore, the concept of coherence is very important in XPCi. Coherence defines the ability of a wave to produce interference patterns and diffraction observables. An ideal plane wave will be coherent, while the light emitted from a light bulb will be incoherent.

There are two types of coherence:

- Spatial or transverse coherence: considers the phase between two transversally spaced pairs of points $\Delta\phi(P_3{:}\,P_4)$ (see Figure 4.2), which is determined by the source size.
- Temporal or longitudinal coherence: considers the phase between two longitudinally spaced pairs of points $\Delta\phi(P_1{:}\,P_2)$ (see Figure 4.2), which is determined by the monochromaticity of the electromagnetic wave.

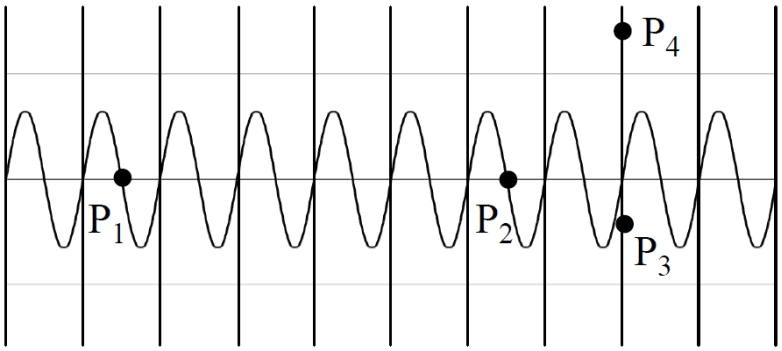

Figure 4.2. Schematic of an electromagnetic wave underlining the difference between spatial and temporal coherence.

Now the question is how to detect these changes in ϕ since X-ray detectors used in conventional absorption imaging rely on detecting intensity changes. This can be achieved either by detecting interference patterns or by using X-ray refraction. The first option can be achieved by allowing the X-rays to propagate through a distance sufficiently long for both perturbed and unperturbed waves to interfere and thus create a measurable pattern. Alternatively, both perturbed and unperturbed waves can be recombined in an interferometer.

The second option is to use X-ray refraction. X-rays refract in the same way as visible light but at smaller angles. The propagation direction of the X-rays is orthogonal to the wave front so a change in the wave front is consistent with changes in the X-ray propagation direction. The refraction angle α is given by the following equation:

$$\alpha = \frac{\lambda}{2\pi}\nabla_{x,y}\Phi, \tag{4.7}$$

where $\nabla_{x,y}$ is the gradient, with each derivative giving the refraction angle in each plane.

4.2.2 Phase contrast imaging techniques

There are several methods of performing XPCi. The main ones are the analyser-based imaging, free-space propagation imaging, crystal and grating interferometry, and edge-illumination methods. A brief review of these

methods will be given in this section, with a summary of the advantages and disadvantages of each technique.

Analyser based imaging (ABI): in this method a parallel quasi-mono-energetic X-ray beam irradiates the object. A crystal (analyser) is set between the sample and detector to analyse the radiation leaving the object. More crystals (monochromators) are required to achieve a quasi-monoenergetic X-ray beam before the sample, as shown in Figure 4.3.

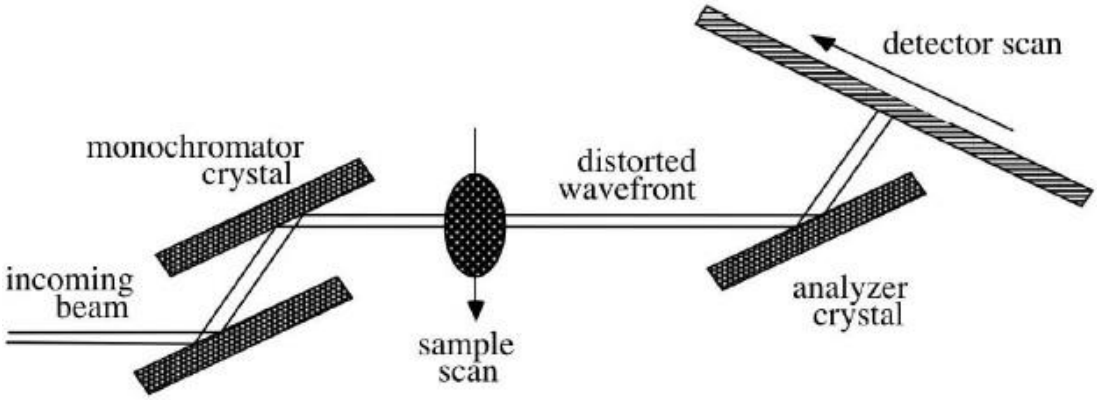

Figure 4.3. Synchrotron beamline ABI. The X-ray beam energy is selected by the monochromator crystals reaching the detector after being reflected by the analyser. From [20].

The analyser selects the photons which satisfy the Bragg law:

$$\lambda = 2d\sin\vartheta, \tag{4.8}$$

where d is the crystal d-spacing and ϑ is the grazing angle of incidence to the crystal. The detector is illuminated by a narrow X-ray beam that contributes to image formation.

The parameters that influence the image contrast in this technique are the composition and quality of the crystals, the energy of the X-ray beam, the divergence of the X-ray beam and the diffraction order. Once all these parameters are chosen the image contrast will depend on the angular position of the analyser crystal with respect to the Bragg angle corresponding to the X-ray energy.

Grating interferometry: Grating-based imaging (GI), also known as X-ray Talbot interferometry, is based on the use of grating interferometers. The

standard setup consists of a phase grating and an analyser. This method is based on the optical phenomenon discovered by Talbot [12] where a grating illuminated by coherent X-rays forms images of the grating repeated at certain distances known as Talbot distances. The Talbot distances d_t are given by the following equation:

$$d_t = \frac{2p^2}{\lambda}, \tag{4.9}$$

where p is the period of the grating.

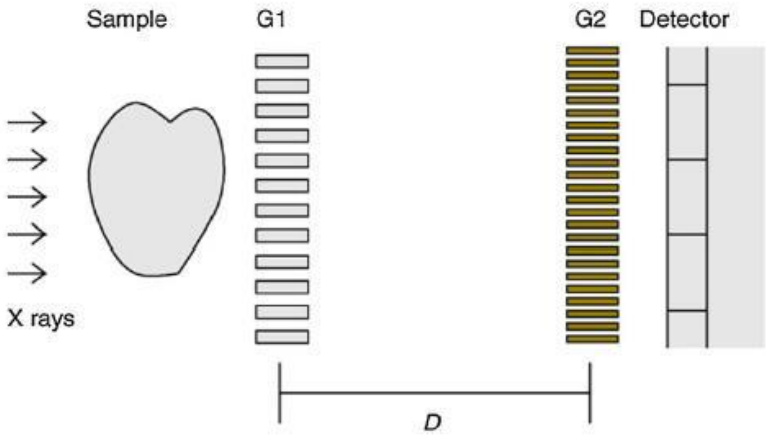

Figure 4.4. Schematic of the GI setup where the two gratings (G1 and G2) are separated by a Talbot distance D and the detector is positioned just after G2. From [21].

When an object is placed before the grating the interference pattern is modified due to the absorption, refraction and scattering in the sample. By placing an absorption grating (analyser) at a Talbot distance and taking measurements with and without the object in position it is possible to measure the changes in the position of the interference pattern.

Pfeiffer *et al.* [22] demonstrated that this technique can be used with conventional incoherent X-ray sources if a source grating is placed just after the X-ray source. This configuration was called Talbot-Lau configuration.

Edge-illumination or coded aperture technique: The coded aperture (CA) imaging or edge illumination (EI) technique has been developed by Olivo *et al.* [19]. The main principle of this technique is that the phase sensitivity of an X-ray imaging system can be significantly improved if only the edge of the pixel

of the X-ray detector used is illuminated. This means that a fraction of the beam falls outside the pixel edge.

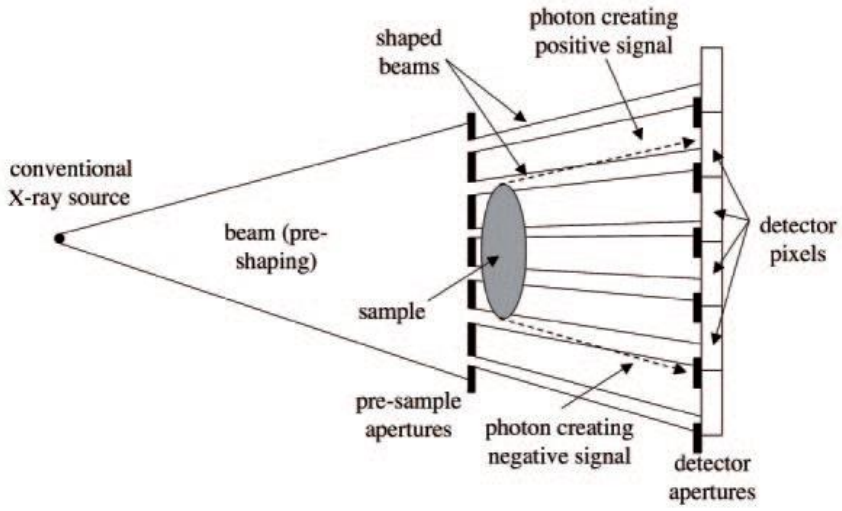

Figure 4.5. Schematic of the EI technique. From [20].

This method uses two coded mask apertures: a pre-sample coded-aperture mask and an after-sample coded aperture mask. The first one is placed just before the object in order to dissect the incoming X-ray beam into small beamlets. Each X-ray beamlet hits the detector pixel in a place given by the coded aperture mask placed after the sample.

The after-sample coded aperture mask is in direct contact with the X-ray detector. Its purpose is to create insensitive regions along the separation between adjacent pixel rows. The pre-sample coded mask avoids unnecessary radiation going through the object therefore improving the efficiency in dose delivery.

By interacting with the object, X-ray photons that would not hit the detector if the object was not in place will be deflected to it leading to a higher number of counts. Following the same idea, photons that would hit the detector pixel if the object was not in place will now be deflected outside the detector area thus reducing the number of counts. The recorded signal will consist of negative and positive peaks similar to the ones obtained with the ABI technique.

Free space propagation, in-line holography or propagation based imaging (PBI): Snigirev *et al.* [23] showed that it is possible to perform phase contrast imaging without the need of any optics. The only requirement is a coherent X-ray source.

A difference in the δ value between a detail and the surrounding background results in a phase shift between the wave transmitted through and outside the detail. Due to this phase shift, both perturbed and unperturbed waves interfere. When the detector is placed at a sufficiently large distance, an interference pattern is detected.

This effect can be explained by the near field Fresnel diffraction theory (Figure 4.6).

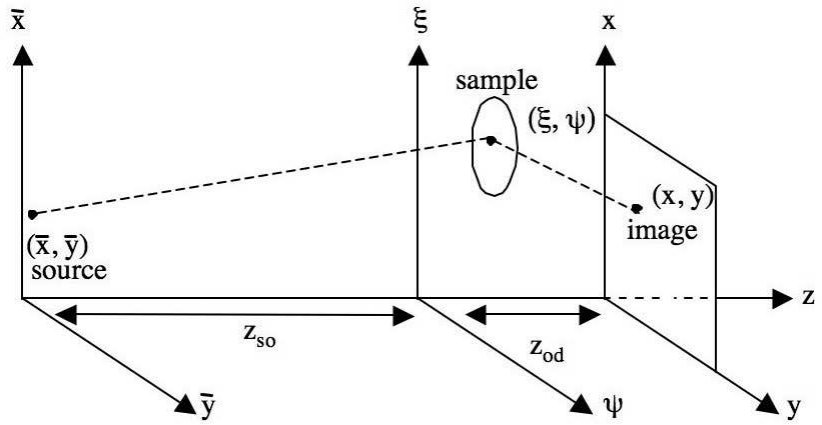

Figure 4.6. PBI formulation using Fresnel-Kirchhoff diffraction integrals. From [20].

The Fresnel-Kirchhoff diffraction integral is given by:

$$E(x,y) = -\frac{i\cos\vartheta}{\lambda}\int d\xi \int d\psi f(\xi,\psi), \tag{4.10}$$

where $E(x,y)$ is the electric field at the image formation plane x, y. The integral over ξ and ψ extends over the object plane. ϑ is the inclination factor [24], which in the case of synchrotron radiation (and betatron X-rays) is equal to zero because the source to object distance (z_{so}) and the object to detector distance z_{od} are much larger than the sample size. The function f is given by the following equation:

$$f = \frac{\exp(2\pi i/\lambda\{[z_{so}^2 + (\bar{x} - \xi)^2 + (\bar{y} - \psi)^2] + [z_{od}^2 + (\xi - x)^2 + (\psi - y)^2]\}}{\lambda} \times \exp[i\Phi(\xi, \psi)], \quad (4.11)$$

where $\bar{x}$ and $\bar{y}$ represent the source location in the source plane and ϕ is the phase shift produced by the sample (eq. 4.5). This integral is typically solved numerically.

The resolution of this technique depends mainly on the size of the source and on the pixel size of the X-ray detector used. The X-ray beam has to be spatially coherent but monochromaticity is not required. Wilkins *et al.* [13] showed that it is possible to obtain XPCi images using this method with polychromatic sources.

To fulfil the condition that the source has to be spatially coherent, synchrotron radiation is normally used for this experiments. In the case of laser-driven XPCi, coherence is guaranteed since the source size of the betatron X-rays is of the order of a few microns [4].

The following table summarises the main advantages and disadvantages of each phase-contrast imaging method:

Table 4.1. Summary of advantages and disadvantages of each XPCi technique.

Method	Advantages	Disadvantages
ABI	• Can be used over a wide range of energies (20-100 keV). • Large field of view.	• Requires both intense and monochromatic X-rays.
GI	• Works with conventional X-ray tubes. • Large field of view.	• Different gratings are required for different energy ranges. • Gratings are expensive and difficult to produce.
EI	• Little requirements of the X-ray source. • High energy imaging close to 100 keV performed.	• Not really a disadvantage but the technique is still at an early stage.
PBI	• The setup of this method is simple. • Divergence and beam size not important. • Works with polychromatic beams.	• This technique requires a small source size, *i.e.*, high spatial coherence.

4.3 Semiconductor pixel detectors

A brief introduction on semiconductor pixel detectors is given in this section because they play an important role in the experiments that will be described in the next sections.

In a semiconductor pixel detector a bias voltage is applied to the electrodes of a semiconductor diode. When ionising radiation interacts with the diode, free electrons and holes are created in a quantity proportional to the incident X-ray photon energy. These charges move in the electric field of the detector and are collected by read-out electronics for further processing. The signal amplification, discrimination and analog-to-digital conversion (or counting) are performed by the electronics. The pixel detector is made of a matrix of pixels, where each pixel of the matrix is connected to its own electronic chain.

Semiconductor pixel detectors can be hybrid or monolithic. Monolithic devices have only one chip where the readout electronics are on the surface and the bulk is used as the sensor.

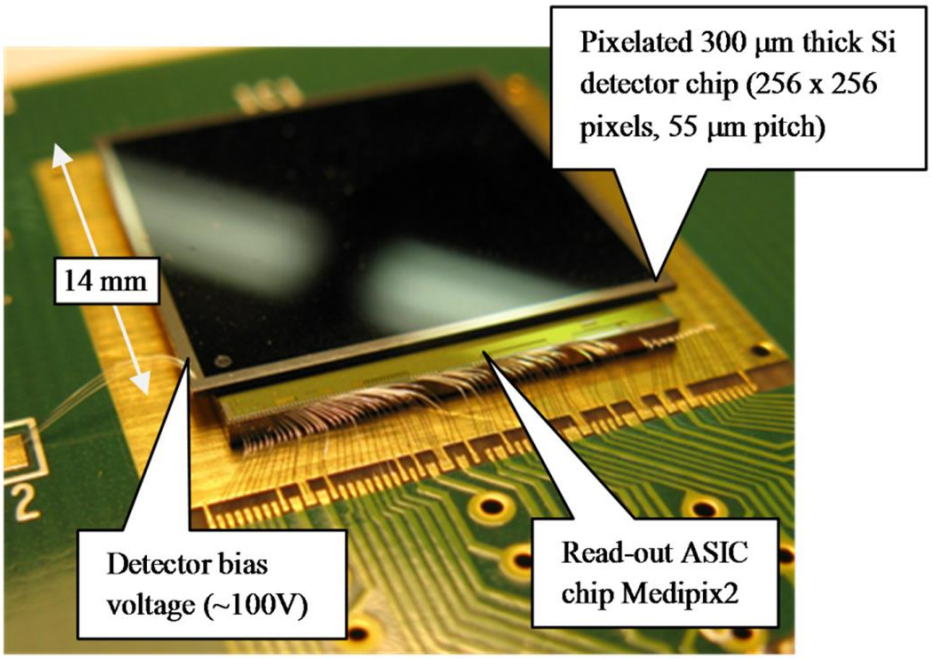

Figure 4.7. Shot of the hybrid semiconductor pixel detector Timepix. The sensor chip is usually made of Si but other materials are available. Picture from [25].

The hybrid pixel devices consist of two chips corresponding to the sensor and to the read-out electronics for all the pixels. Both chips are usually bump-bonded. Some examples of hybrid pixel detectors are Timepix [26] or XPAD [27]. The main advantage of the hybrid detectors is that it is possible to attach the read-out chip to sensors made of different materials such as CdTe or GaAs. On the other hand, monolithic devices are limited to silicon.

Timepix has been used to measure the spectrum of the ALPHA-X betatron source. The Timepix sensor has an active area of 1.4x1.4 cm^2 with 65536 pixels (256x256) of 55 μm size. Each pixel is connected to its corresponding preamplifier, double discriminator and digital counter integrated on the readout chip.

Timepix is based on the successful Medipix2 semiconductor pixel detector [28], with the main difference being the design of the read-out chip. This detector can be used in three different modes:

1. Medipix mode where an integrated counter counts incoming particles.
2. Timepix mode, where the counter measures the time when the particle is detected.
3. Time over threshold (TOT) mode, where each pixel allows a direct energy measurement.

Prior to experiments, the detector is calibrated using a laboratory sealed americium source (Am-241). Am-241 decay produces both X-rays and 5.5 MeV alpha particles. A 1 mm Al filter is placed between the Am-241 source and Timepix to minimise the noise in the detector. The X-rays emitted by the Am-241 source after decay correspond to energies 13.9, 17.8, 26.3 and 59.5 keV. The Al filter attenuates the 13.9 and the 17.8 keV peaks allowing the 26.3 and 59.5 keV lines to be clearly measured. Although attenuated, the 13.9 keV peak is also distinguishable because it is much more intense than the 17.8 keV peak.

An additional reference point for the calibration of the detector is given by the Compton edge, which is the maximum energy that an X-ray can deposit through Compton scattering. For the energies considered here, the interaction between X-rays and matter is governed by the photoelectric and Compton effects. In the photoelectric effect X-rays are absorbed by the material and their entire energy is deposited in the detector. On the other hand, in the Compton effect, X-rays scatter from electrons and can escape the material, depositing only a fraction of their energy in the detector. In this case, the amount of energy deposited depends on the photon scattering angle, and therefore on the energy of the photo-electrons. When the photon is fully back-scattered the amount of energy deposited is maximum. This is called the Compton edge.

For a photon energy of 59.5 keV the Compton edge corresponds to an energy of 48.3 keV. The Compton edge is calculated using the following equation:

$$E_{edge} = \frac{E_\gamma}{1 + \frac{2E_\gamma}{m_0 c^2}} \cong 48.3 \text{ keV}. \tag{4.12}$$

The following Figure shows an example of the spectrum recorded with Timepix using the Am-241 source and the corresponding calibration curve obtained for Timepix:

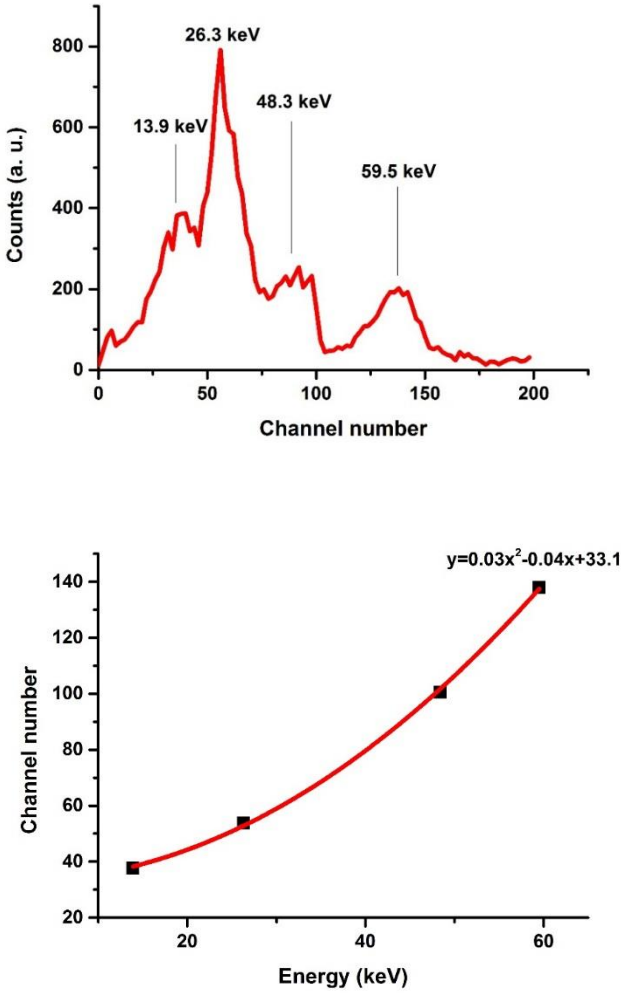

Figure 4.8. Top: Example of spectrum recorded with Timepix using an Am-241 source for detector calibration. Bottom: Calibration curve obtained from Am-241 emission lines and Compton edge (48.3 keV).

4.4 Characterisation of the ALPHA-X betatron X-ray source

4.4.1. Introduction and experimental setup:

Prior to exploring imaging applications, the betatron X-ray source at the ALPHA-X laser wakefield accelerator beam line at the University of Strathclyde

has been characterised. An experiment has been setup at the ALPHA-X beam line for this purpose.

Laser pulses from a Ti:sapphire laser with energy of 0.9 J, duration of 35 fs, and a central wavelength of 800 nm, are focused using a F/18 spherical mirror to a spot diameter of 40 μm at the entrance of a 2.7 mm diameter pulsed supersonic helium gas jet producing a 10 μm wide relativistic plasma channel. The width of the plasma channel is based on PIC simulations [29]. The resolution of the imaging system used is not high enough to measure 10 μm (see Figure 3.6 right). These laser parameters correspond to a vacuum peak intensity of $I = 2 \times 10^{18}$ $\mathrm{Wcm^{-2}}$ on target. The experiment was performed before the laser upgrade as mentioned in Chapter 3.

A schematic of the experimental setup for the characterisation of the source can be seen in the following figure:

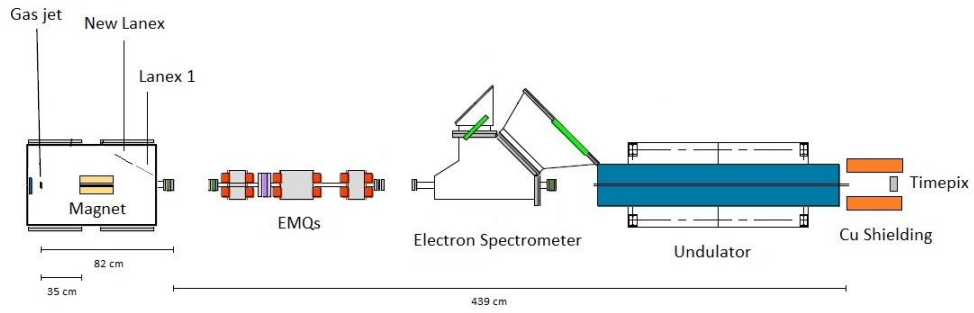

Figure 4.9. Experimental setup schematic for the characterisation of the betatron source showing the key components of the experiment.

4.4.2 X-ray spectrum and critical energy:

The spectrum of the emitted X-rays has been measured using the Timepix detector. A 0.7 T bending magnet is placed on a motorised stage inside the interaction chamber just after the gas-jet to deflect the accelerated electron beam away from the laser axis close to where it is produced.

The electron beam could have been deflected using the beam line electron spectrometer described in Chapter 3 of this thesis. However, due to the pointing instability, electrons can hit the beamline pipes before entering the

electron spectrometer and produce bremsstrahlung radiation that would mask the betatron source.

The magnet inside the chamber bends the electrons towards the side wall of the interaction chamber. The emerging bremsstrahlung radiation is emitted off axis. This minimises the on-axis bremsstrahlung component and therefore reduces the background noise on the X-ray detector.

The deflected electrons are detected before they hit the chamber wall using two scintillating LANEX phosphor screens (Lanex 1 and New Lanex in Figure 4.9) and their energy spectrum is measured. Stable quasi-monoenergetic electron beams of ~150 MeV are measured.

The electron beam charge was measured using imaging plates. Each measurements was performed by averaging 5 laser shots. An electron beam charge between 5-7 pC/shot is estimated. The typical bunch length of the electron beams from a LWFA is in the range 1-10 fs [29] and the repetition rate of the accelerator is set to 0.33 Hz, limited by gas loading on the vacuum pumps.

The X-ray detector, *i.e.* Timepix, is placed at the end of the beam line (source-detector distance is 5.7 m) in order to characterise the spectrum of the X-ray betatron source. It is laterally shielded by copper bricks to reduce the background noise as much as possible. The detector itself is enclosed in an Al case in order to block the k-alpha lines from the copper. The X-ray beam leaves the interaction chamber and propagates through a 4.39 m long column of air to the Timepix detector.

The calibration of the detector was checked every day with the Am source in order to monitor changes in the calibration. No significant changes were observed from day-to-day.

Before starting a measurement with Timepix, a threshold equalization of the detector was performed. This is required since the pixels are not all identical due to the fabrication process. Because of this, every pixel has a different noise

level and therefore the threshold energy has to be adjusted for each pixel individually.

This process is called threshold equalization and it can be done automatically with the PixelMan software [30]. Threshold equalization on Timepix was performed every day before the beginning of the measurements.

The X-ray spectrum was measured for different plasma densities by changing the backing pressure of the gas (pressure scan).

Each set of data was recorded with and without a filter in front of the Timepix semiconductor detector. The filter used was 1 mm thick Al. The filter was placed in front of the detector for two reasons:

1. To confirm that the radiation recorded was coming from the plasma accelerator (not noise or k-alpha lines from different metal components of the beamline).
2. To decrease the number of counts to a maximum of one photon per pixel as explained below.

The number of electrons generated in the sensor is proportional to the X-ray photon energy. The X-ray spectrum of the incoming photons can be measured by computing the intensity histogram of the signal. In this kind of measurement, the electron charge is not deposited in a single pixel of the chip, but spreads over several neighbouring pixels. However, to obtain a correct measurement, it is important that every photon is separated from the others on the chip, *i.e.*, this measurement relies on the assumption of a low photon flux regime achieved by using a filter to reduce the incoming flux of photons.

The data from Timepix is corrected for attenuation in the materials the X-rays are passing through before they reach the detector (air, beamline, perspex windows and corresponding metal filter). The attenuation coefficients for all the materials for each energy can be found in the Nist database [31].

To remove the noise, a Savitzky and Golay filter was used. This method is widely used to increase the signal-to-noise ratio without distorting the original signal. More information on this method can be found in reference [32].

Finally, the critical energy was obtained by fitting the data to a synchrotron-like spectrum, *i.e.* the integral of the Bessel function (which will be described later on in this Chapter) that minimizes the correlation coefficient with the analysed data.

Plasma densities in the range from 1.72×10^{19} cm^{-3} to 2.24×10^{19} cm^{-3}, depending on the gas backing pressure used, were measured using a Mach-Zehnder interferometer. The interferometer is set up in an independent vacuum chamber so that the gas jet/nozzle system can be characterised before the experiment. The setup of the interferometer and the characterisation of these nozzles were performed by Mr David Grant.

The following plots show the X-ray spectrum measured for different plasma densities. Each spectrum corresponds to an accumulation of 1000 shots:

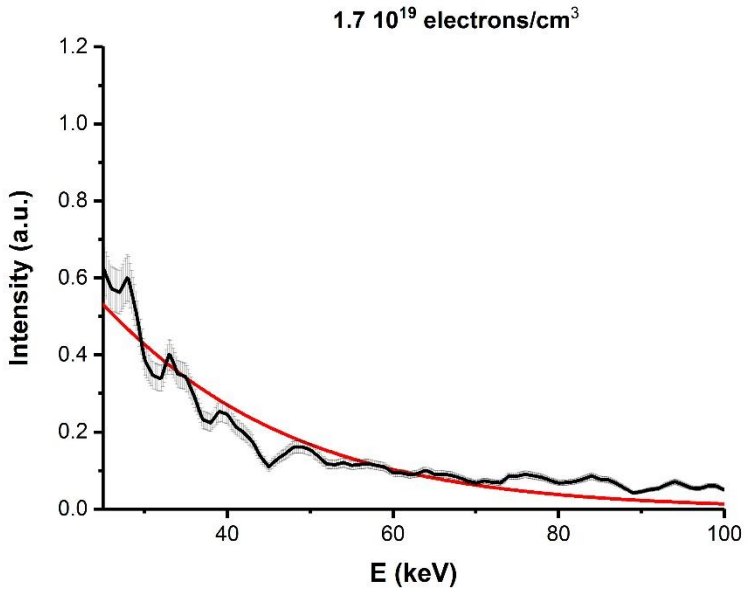

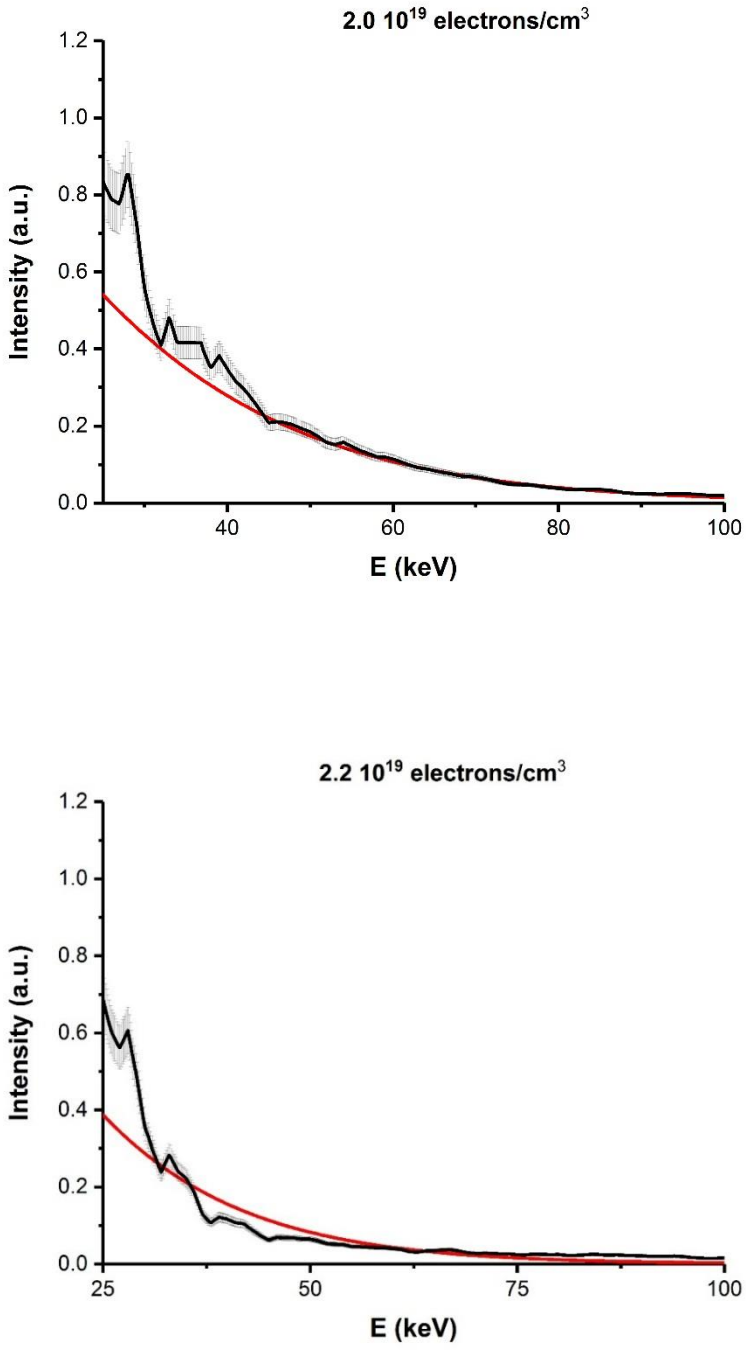

Figure 4.10. X-ray spectrum recorded using Timepix for different plasma densities corresponding to 25, 30 and 35 bar backing pressure. The shaded area that can be seen in the plots corresponds to the error bars and the red curve corresponds to the integral of the Bessel function fitting.

The critical energy E_c is defined as the energy that divides the emitted power into equal halves. The critical energy obtained for each plasma density is summarised in the following table:

Table 4.3. Critical energy measured with Timepix for each plasma density.

n_p (10^{19} cm^{-3})	1.72 ± 0.17	2.04 ± 0.20	2.24 ± 0.22
E_c (keV)	18.2 ± 2.1	17.9 ± 2.1	13.9 ± 1.6

A second measurement of the critical energy of the betatron radiation was performed using sets of different metal filters (Cu, Al, Ti and Ag). The shadows cast by the metal filters were recorded with imaging plates (Fuji BAS-SR). A schematic of this part of the experiment is shown in Figure 4.11. The set of metal filters was placed just after the vacuum chamber and the imaging plate was placed a few cm after the filters. To prevent K_α lines to reach the imaging plate, a short gap of air was left between the metal filters and the image plate. This can be seen in Figure 4.11.

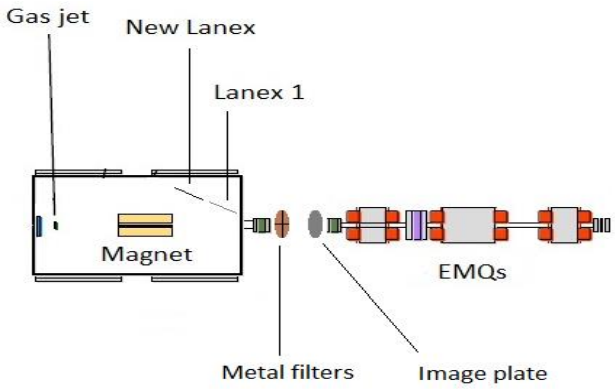

Figure 4.11. Schematic of the experimental setup for the measurement of the betatron X-rays critical energy using metal filters.

As in the Timepix measurements, the electron beam is bent upward by the bending magnet to avoid irradiating the filters and image plates. By measuring the attenuation through the different filters it is possible to estimate the critical photon energy of the emitted radiation.

The X-ray beam intensity distribution is assumed to be uniform across the filters. By assuming that the X-rays produced have a synchrotron-like spectrum it was possible to calculate the critical energy matching the measured attenuation through the set of metal filters.

This method has advantages and disadvantages: on one hand, it is very simple and provides a good second measurement to compare with the critical energy measured using Timepix.

On the other hand, with this measurement it is not possible to obtain detail of the spectral shape. It is also not possible to measure deviations from a synchrotron-like spectrum.

All the measurements have been performed in a single shot. The experiment was performed for the same plasma densities used in the measurements performed with Timepix.

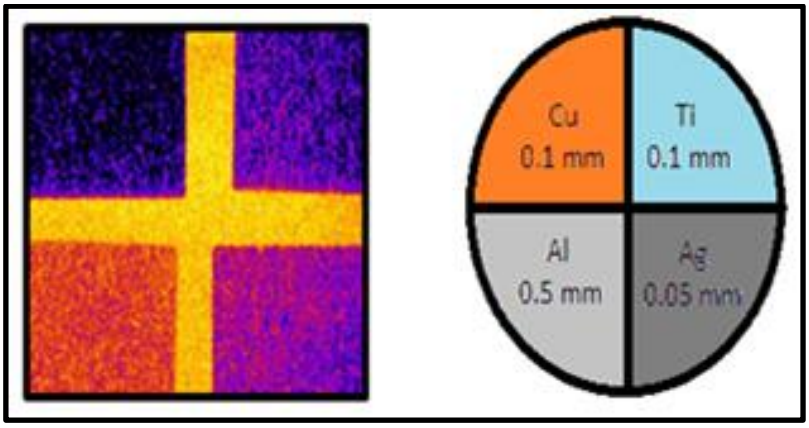

Figure 4.12. False colour image showing the shadows projected by 4 metal filters on an imaging plate for a typical shot and distribution of the thickness and material used to measure the critical energy.

The following table summarises the critical energies obtained for each plasma density using metal filters. The results shown correspond to an average of 10 measurements for each plasma density:

Table 4.3. Critical energy measured metal filters for each plasma density

n_p (10^{19} cm^{-3})	1.72 ± 0.17	2.04 ± 0.20	2.24 ± 0.22
E_c (keV)	17.7 ± 2.5	15.7 ± 1.2	15.8 ± 1.2

4.4.3 X-ray beam divergence:

The divergence of the emitted betatron X-rays has also been measured. The setup used in this part of the experiment is very similar to the setup shown in Figure 4.11.

In this case, an imaging plate was placed just after the interaction chamber to record the shape of the X-ray beam. Note that the electrons are bent away from the laser axis. The distance between the gas jet and the imaging plate is 82 cm. The laser is linearly polarised in the horizontal direction. All measurements have been taken in a single shot. An example of X-ray distribution on an imaging plate can be seen in Figure 4.13.

The divergence can be estimated from the beam size on the imaging plate. Here, a convention similar to what is typically used for lasers will be adopted. The half-angle divergence is defined as:

$$\vartheta = \frac{w}{l} \tag{4.13}$$

where *w* is the beam waist and *l* is the distance source-detector.

The beam waist is estimated by taking a cross-section and fitting it to the following intensity function:

$$I = I_0 e^{-2\left(\frac{x^2}{w^2}\right)}. \tag{4.14}$$

Since the spot is often elliptical and tilted, two cross-sections have been taken, along the major and minor axis. This has been done for each individual shot, rotating the images as required. An example of the analysis is shown in Figure 4.13. The corresponding conversion factor from pixels to cm is known since the size of the imaging plate is known, *i.e.* 740 pixels correspond to 4.5 cm.

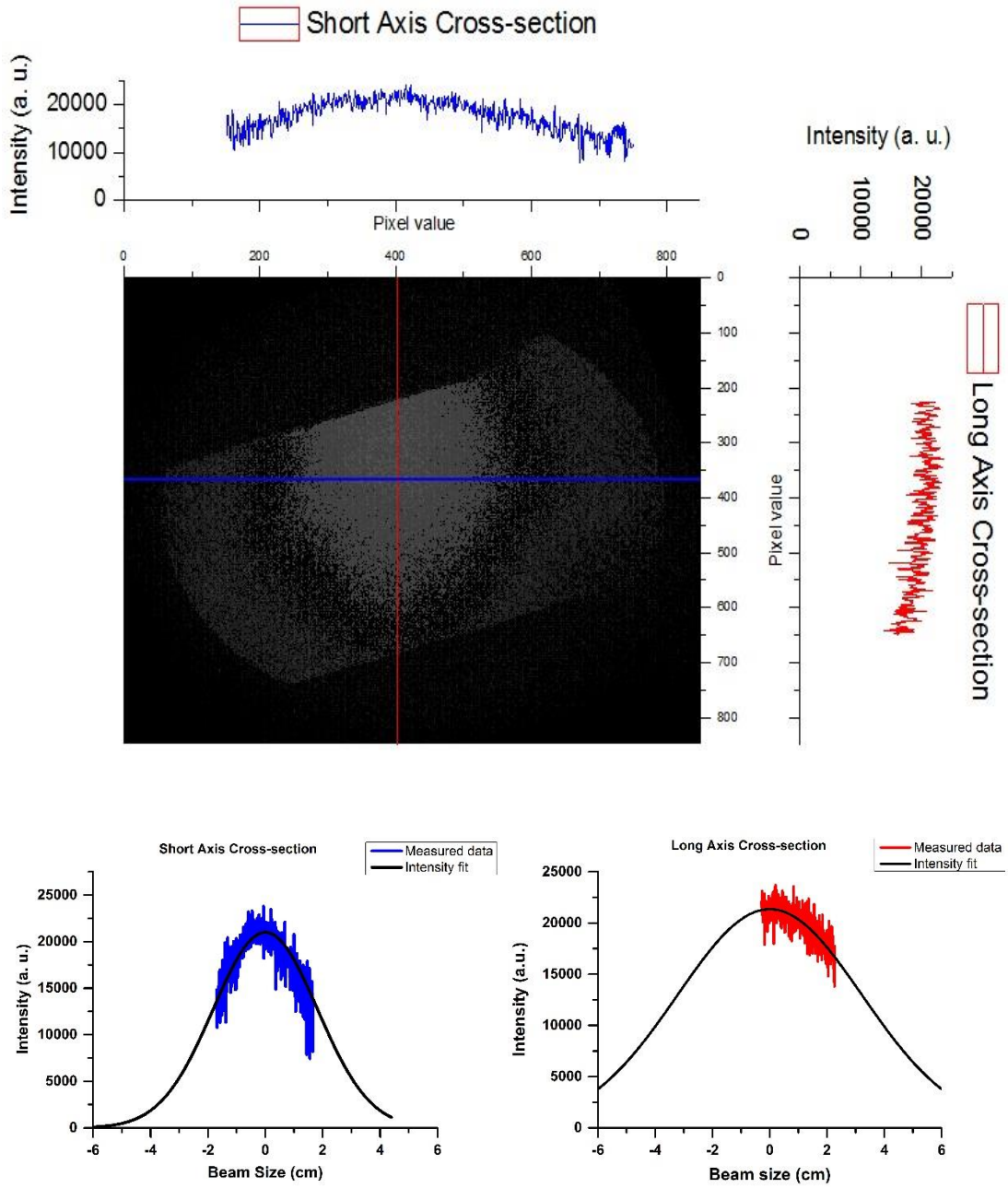

Figure 4.13. Top: raw image of the spatial distribution of the betatron X-ray source recorded by a Fujifilm BAS-SR imaging plate 82 cm behind the laser-plasma interaction in a single shot. The shadow of the magnet is also visible. The round shadow is due to the exit rounded pipe of the interaction chamber. Bottom: Short (blue) and long (red) profiles of the X-ray beam fitted to equation 4.14. The calculated beam waist corresponds to 3.6 cm in the short axis and 6.5 cm in the long axis. This corresponds to a half angle divergence of 43.9 mrads for the short axis and 79.3 mrads for the long axis. The electron density for this particular shot was 1.72 ± 0.17 (10^{19} cm^{-3}).

An interesting feature of these measurements is the shape of the X-ray beam, which has been found to be elliptical or circular depending on the laser shot. Statistically, around 75% of the 21 shots recorded show an elliptical shape and 25% a circular shape. The elliptical X-ray beam profiles are always tilted,

although the tilting angle is not constant but varies between -60 and 30 degrees depending on the laser shot. The flatness/ellipticity also varies from shot to shot.The flattening or ellipticity of an ellipse gives a measure of the deviation from a perfect circle. It is given by the following equation:

$$\varepsilon = \frac{a - b}{a}, \tag{4.15}$$

where a is the radius of the long axis and b the radius of the short axis. The factor b/a is known as the compression factor. The flattening also varies from shot to shot from a maximum of 0.7 (Figure 4.14, bottom right), corresponding to the most elliptical shot, down to almost 0 (circular shots). The 21 shots have been measured on two consecutive days. No change in the electron beam parameters or laser system performance have been observed over these two days.

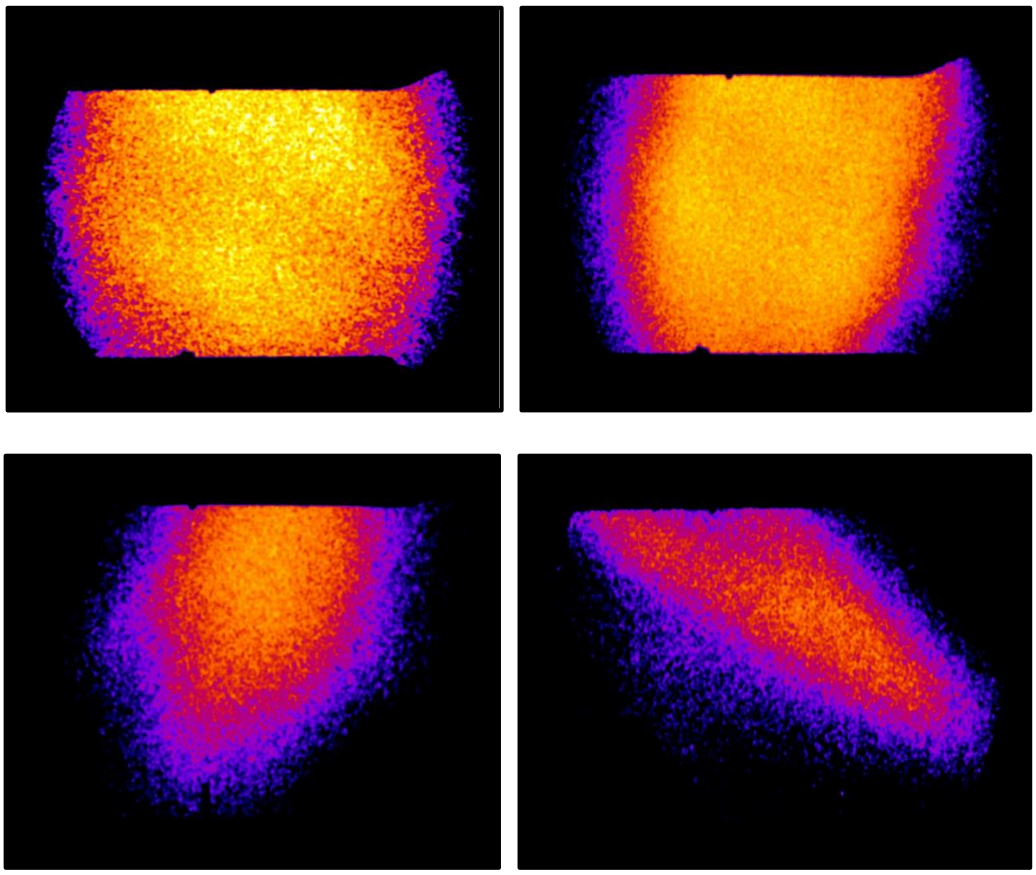

Figure 4.14. False colour image showing X-ray shots recorded on the imaging plates showing the differences in the spatial distribution from shot to shot. Top left: almost perfect circular shot. Top right: shot tilted at 15 degrees and 0.2 flattening. Bottom left: X-ray beam tilted at 20 degrees and 0.5 flattening. Bottom right: 60 degrees tilting angle and 0.7 flattening value.

The shape of the X-ray beam depends on the trajectory that the electrons follow in the bubble. The type of trajectory depends on the initial conditions of the electrons as they are injected into the bubble and on the characteristics of the electromagnetic fields inside the bubble. Ideally, the injected electron beam and the bubble are cylindrically symmetric with respect to the laser propagation axis and the X-ray beam should have a circular profile. However, in practice, the symmetry can be broken if the laser spot size is elliptical, if the laser intensity distribution is not uniform or if the wavefront is tilted. Electrons can also interact with the laser electric field inside the bubble and oscillate preferentially along the laser polarization direction [33]. As a possible explanation, the fact that some shots are tilted might indicate a change in the polarisation angle of the laser.

A total of 21 shots have been analysed, corresponding to seven shots for each plasma density studied. The divergence of the X-ray beam does not change significantly with the density. However, more shots would be required to make this study more statistically relevant, although the use of imaging plates makes it very time-consuming. On average, the half-angle divergence (equation 4.13) measured for the elliptical shots is 38.0 ± 2.6 mrads for the short axis and 62.2 ± 2.7 mrads for the long axis (rms). For the circular shaped shots, the divergence measured was 63.3 ± 2.9 mrads (rms).

From equation 2.43 it is possible to calculate the maximum energy expected for the electron beam and therefore the Lorentz factor γ. For a plasma density of 1.72×10^{19} cm^{-3} and a laser intensity of 1.9×10^{18} $\mathrm{Wcm^{-2}}$ the expected maximum energy is 157.5 MeV, which agrees well with the 150 ± 12 MeV electron beam energy measured. This gives a maximum γ of 308, since $\gamma = E/(m_e c^2)$, with $m_e c^2 = 0.511\ \mathrm{MeV}$ for electrons.

Since the critical energy has been measured, the amplitude of the betatron oscillations r_β can be calculated using equation 4.16:

$$E_c = \frac{3\hbar\omega_p^2 r_\beta \gamma^2}{2c} \tag{4.16}$$

where ω_p^2 is the plasma frequency and E_c is the measured critical energy. The normalised transverse momentum is given by:

$$a_\beta = k_p r_\beta \sqrt{\frac{\gamma}{2}}, \tag{4.17}$$

where $k_p = \frac{2\pi}{\lambda_p}$ is the plasma wavenumber.

Table 4.4. Measured plasma densities, critical energy and long axis half-angle divergence and corresponding estimated amplitude of the betatron oscillations, normalised transverse momentum and half-angle divergence.

n_p (10^{19} cm^{-3})	E_c (keV)	r_β (μm)	a_β	θ_{th} (mrad)	θ_{exp} (mrad)
1.72	18.2	2.1	20.0	67.1	63.1
2.04	17.9	1.8	17.6	66.3	62.5
2.24	13.9	1.2	11.9	47.8	62.6

Table 4.4 shows the estimated values for r_β, a_β and the theoretical and long axis experimental half-angle divergences (calculated using equation 2.62) from the estimated a_β for each plasma density and critical energy of the betatron measured with Timepix during the experiment.

From the results shown in table 4.4 it can be seen that the measured X-ray divergence agrees reasonably well with the theoretical value.

The shot-to-shot stability of the X-rays has been measured. The results can be seen in Figure 4.15 for the 21 laser shots. The beam line axis is used as the reference point. The measured mean pointing angles correspond to 4.3 ± 3.7 mrads and 5.0 ± 2.9 mrads for the horizontal and vertical axes, respectively. The maximum pointing angles are 11.1 mrads for the vertical axis and 15.0 mrads for the horizontal axis.

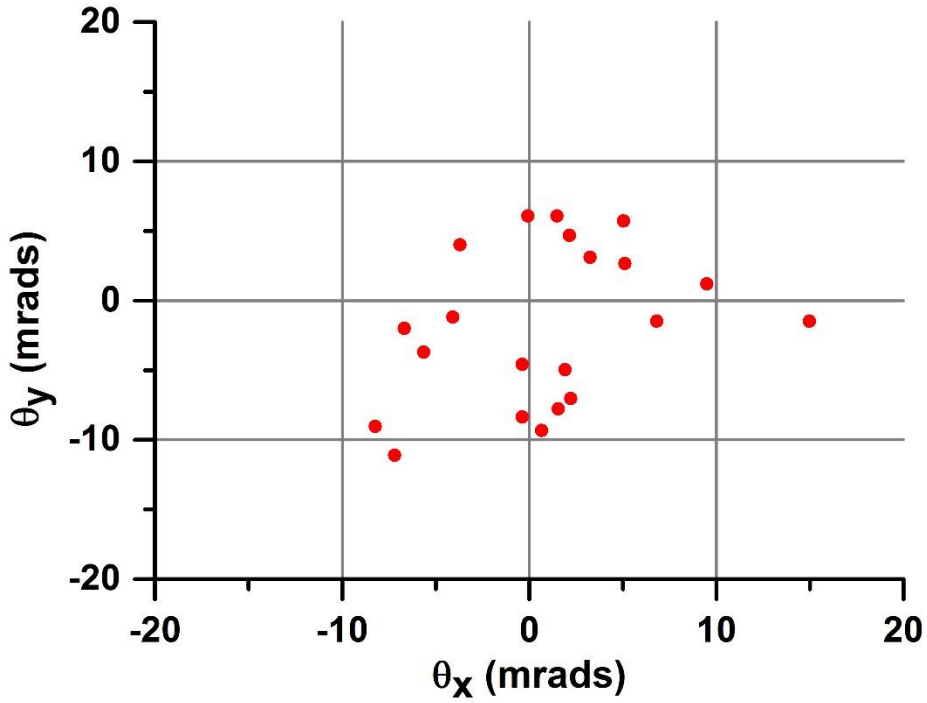

Figure 4.15. X-ray beam pointing angles for 21 laser shots. The origin denotes the beam line axis.

4.4.4. X-ray beam polarisation:

The polarisation of the betatron X-rays has also been measured using Timepix. In previous studies [33] the linear polarisation of the betatron X-rays has been measured using LiF crystals to build an X-ray polarimeter. The results presented here have been obtained only using a semiconductor detector, which has the added advantage of making the setup simpler.

This kind of X-ray polarisation measurements was first proposed by Fraser in 1989 [34]. After this, Tsunemi et al. [35, 36] successfully performed X-ray polarisation measurements of synchrotron radiation with an energy between 15 and 37 keV. Later on, Bogner et al. [37] measured the polarisation of synchrotron X-rays with energies ranging between 10 and 75 keV.

When a polarised X-ray photon interacts with the Si sensor of a pixelated detector it releases a photoelectron from the K-shell of the Si atom. The direction of the photoelectron released follows a $\cos^2\theta$ probability distribution parallel to the electric field of the incoming X-ray [38]:

$$P(\theta)d(\theta) = \cos^2(\theta)d(\theta) \tag{4.18}$$

The photoelectron moves through the pixelated structure undergoing multiple scatterings and creating electron-hole pairs. To a first approximation the range in μm of the photoelectron for incoming X-rays of tens of keV and for silicon is given by [39]:

$$R(\mu\text{m}) = \left(\frac{E(\text{keV})}{10}\right)^{1.75}, \tag{4.19}$$

where E is the energy of the incoming X-ray in keV.

The ejected photoelectrons cross the pixels depositing energy in more than one pixel. Therefore, their paths can be tracked by the array allowing a measurement of the X-ray polarisation. The distribution of the energy deposited should agree with equation 4.18.

The charge cloud created by the photoelectron is collected in detector pixels. This means that it is possible to measure the polarisation of the incoming X-ray beam if the range of the generated photoelectron is comparable to the pixel size of the semiconductor detector and the charge cloud generated by the photoelectron is collected over at least two adjacent pixels.

In our case, the pixel size of the semiconductor detector used, i.e., Timepix is 55 μm. Using equation 4.19 it is possible to work out the incident energy of the X-ray beam required to generate photoelectrons with a range of 55 μm in silicon, *i.e.*, ~100 keV.

As previously shown, the estimated critical energy of the betatron X-ray beam is ~17 keV, which is an order of magnitude lower than the required energy to generate photoelectrons with a range of 55 μm in silicon. However, as can be seen in Figure 4.10, the synchrotron betatron X-ray spectrum has a tail of high energy photons extending beyond 90 keV. This means that in principle it is possible to measure the polarisation of the high energy tail using this technique.

The results obtained with Timepix for two different experimental runs can be seen in the following Figure:

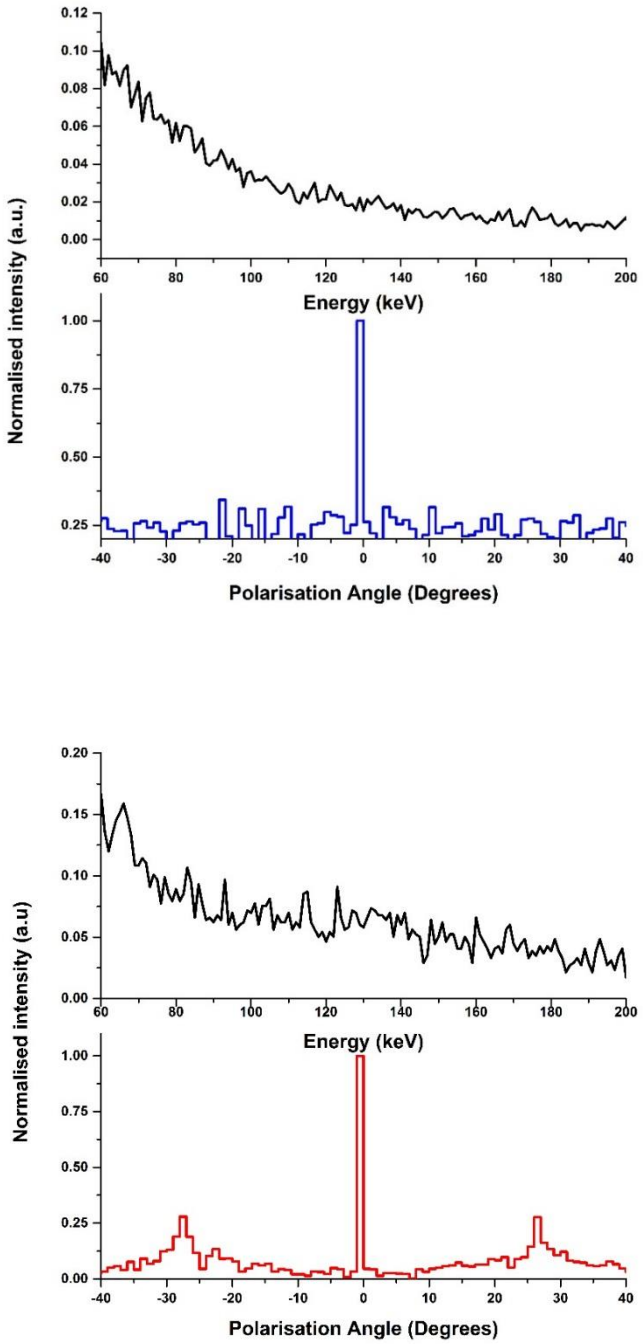

Figure 4.16. Two experimental run examples where the X-ray spectrum of the high energy component and corresponding polarisation state are shown. The top one corresponds to the case in which the betatron X-rays follow the laser polarisation. In the bottom one two additional polarisation states at around -28 and 28 are observed.

The experimental setup is similar to the one used for the X-ray spectrum measurements (Figure 4.9). Both runs shown in Figure 4.16 correspond to an accumulation of 1000 shots. The plasma density is 1.72×10^{19} cm^{-3} for both runs. The critical energy of the X-ray beam estimated from a synchrotron-like fitting (similarly to section 4.3.2) was 17.1 and 16.9 keV respectively.

The top plots in Figure 4.16 show an experimental run in which the polarisation of the X-ray beam is mainly horizontal. In this case, the electrons follow the polarisation of the laser pulse therefore oscillate horizontally.

In the second case (bottom plots in Figure 4.16) the horizontal polarisation state is clearly the predominant one. However, it can be observed that the other two polarisation angles are at around 28 and -28 degrees and do not correspond to the polarisation state of the laser. This will be discussed in section 4.4.6.

This experiment demonstrates that it is possible to measure the polarisation state of the betatron X-rays by simply using a semiconductor detector. Moreover, it is possible to measure simultaneously both the X-ray spectrum and polarisation state. This simultaneous measurement is not possible when an X-ray crystal polarisation state analyser is used.

4.4.5. Phase-contrast imaging experiment using the X-ray source:

In order to demonstrate the potential of the LWFA X-ray betatron source for XPCi applications, a proof of principle experiment has been carried out using the previously characterised betatron X-ray beam produced at the ALPHA-X beamline.

The X-ray source size corresponds to the amplitude of the betatron oscillations, which is of the order of 1 μm. This allows the use of the free space propagation configuration, although the sample to detector distance has to be increased to achieve contrast enhancement. As mentioned in the section 2 of this Chapter, the only requirements for this experimental configuration are a high spatially coherent source (which is guaranteed by the small source size) and an X-ray detector. Monochromatic X-rays are not required [13].

For this experiment a biological sample (dead domestic spider) was placed just after the interaction chamber. The detector used was an imaging plate. The sample was placed at a source-object distance (R_1) of 0.82 m. The sample-detector distance (R_2) is 4.39 m. The magnification M can be calculated using the following relationship:

$$M = \frac{(R_1 + R_2)}{R_1}, \tag{4.20}$$

which yields a value of 6.35 for our setup. As in the previous measurements, a permanent magnet bends the electrons away from the laser axis. A schematic of the setup can be seen in Figure 4.17.

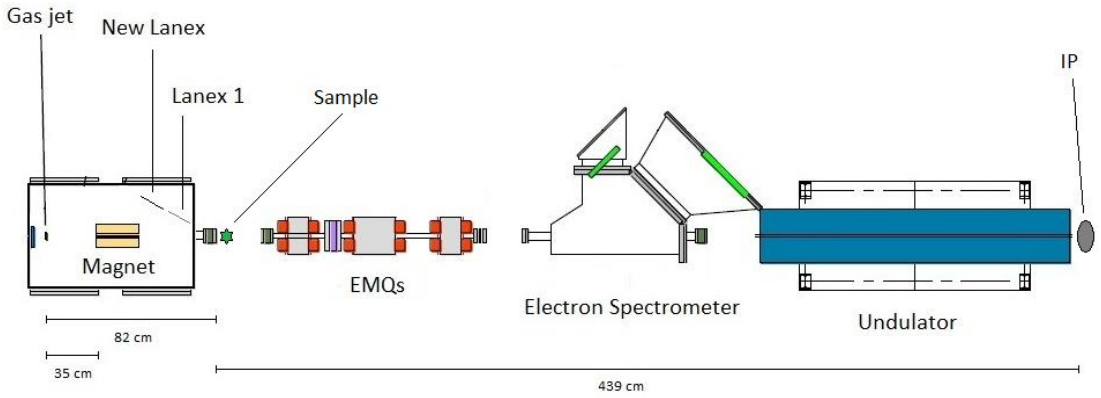

Figure 4.17. Schematic of the XPCi experiment using the X-ray beam source produced on the ALPHA-X beamline. The source to object distance is 0.82 m and the object-detector distance is 4.39 m giving a magnification of 6.35.

The resolution of the image is set by the imaging plate scanner to 50 μm. For the given magnification, this allows resolution of details down to ~8 μm. The transverse coherence length is given by:

$$L = \frac{\lambda l}{\sigma}, \tag{4.21}$$

where λ is the wavelength of the X-ray source, l the source to detector distance and σ the source size. For a 1 μm source size, 15 keV X-rays and 4.2 m source to detector distance the transverse coherent length is equal to L~400 μm. This is larger than the source size, and therefore the imaging resolution, making phase contrast imaging in this configuration possible.

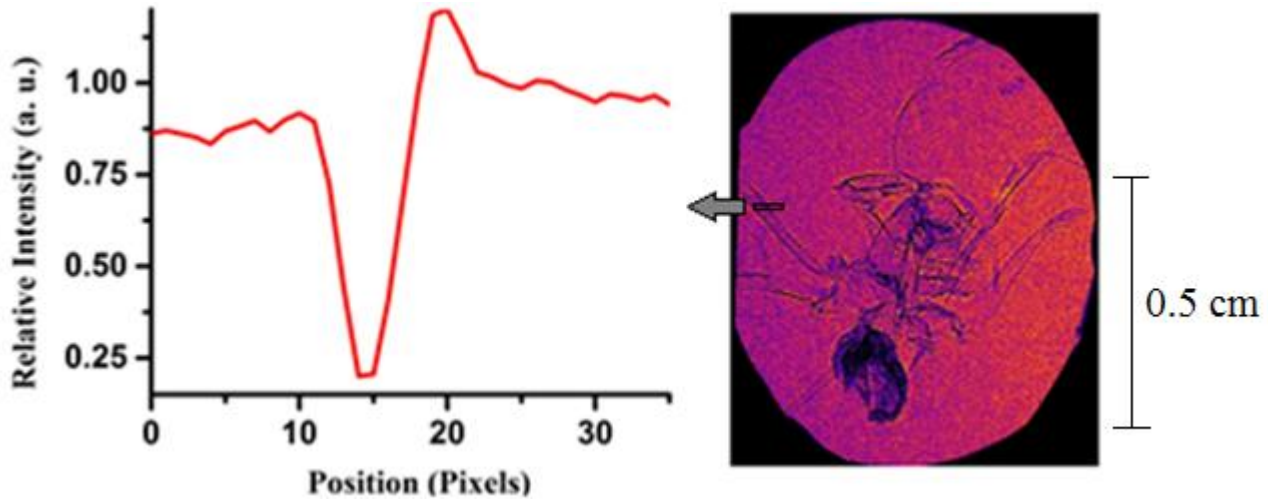

Figure 4.18. R.h.s: image obtained after 300 shots. L.h.s: relative intensity from the edge of a leg. Contrast is estimated to be 0.71. The image is obtained after 300 shots at a repetition rate of 0.33 Hz. From [40].

Absorption contrast from the non-absorbing thin legs and body of the spider would be very poor. However, the use of the free-space propagation technique reveals details of the body of the sample as shown in Figure 4.18. The edge enhancement is clearly observed in different parts of the sample, such as the legs (100-300 μm size).

The contrast can be deduced using the following relationship:

$$C = \frac{(X_2 - X_1)}{(X_2 + X_1)}, \tag{4.22}$$

where X_1, X_2 are the signals from the edge representing, respectively, the highest and lowest intensities. For the fringe corresponding to the line out shown in Figure 4.18 the contrast is approximately 0.71.

The aim was to experimentally show that phase-contrast imaging experiments can be done using the LWFA at the ALPHA-X facility and that the expected XPCi features are clearly observed in the image. This shows the potential of the betatron X-rays for biomedical applications amongst others. Development of real world applications will be discussed in the next section.

4.4.6 Experiment conclusions and discussion:

The measured divergence of the betatron X-rays is of the same order of magnitude of previously reported experiments at similar laser intensities [41], although the critical energy measured is around 10 keV higher than [41], probably because of the higher electron beam energy. Our measurements are compatible with a 150 MeV electron beam energy and 2 μm betatron oscillation amplitude.

Polarisation measurements show that the high energy tail of betatron X-rays can have the same polarisation of the laser beam, as shown in the top graph of Figure 4.16. This suggests that electrons can interact with the laser beam inside the bubble, possibly leading to a resonant enhancement of the amplitude of the betatron oscillations [4].

Previous measurements of the betatron X-ray polarisation have been reported [33] by Schnell et al. using an X-ray polarimeter, where they demonstrated that by tilting the pulse-front of the laser it is possible to control the trajectory of the injected electrons and therefore the polarisation of the emitted betatron X-rays.

Our experiment is different in several respects: firstly, the method of measuring the polarisation of the X-rays is different, as explained in the previous section. Moreover, we have explored the polarisation of the X-rays in the harmonically resonant regime since this regime can increase the purity of the polarisation status of the betatron X-rays as suggested by Schnell [33]. Finally, we observed that the polarisation peaks at around 28 and -28 degrees in some experimental runs, a feature not observed before (to the author's knowledge).

This might be related to a rotation of the polarisation status of the laser. One way to check this would be to measure the Stokes parameters [42] of the laser pulse after interaction with the gas jet.

The Stokes parameters are a set of four numbers that determine the polarisation status of an electromagnetic wave. Normally, they are grouped in a vector known as the Stokes vector. A rough schematic of a possible optical diagnostic for measuring the Stokes parameters shown in the following Figure:

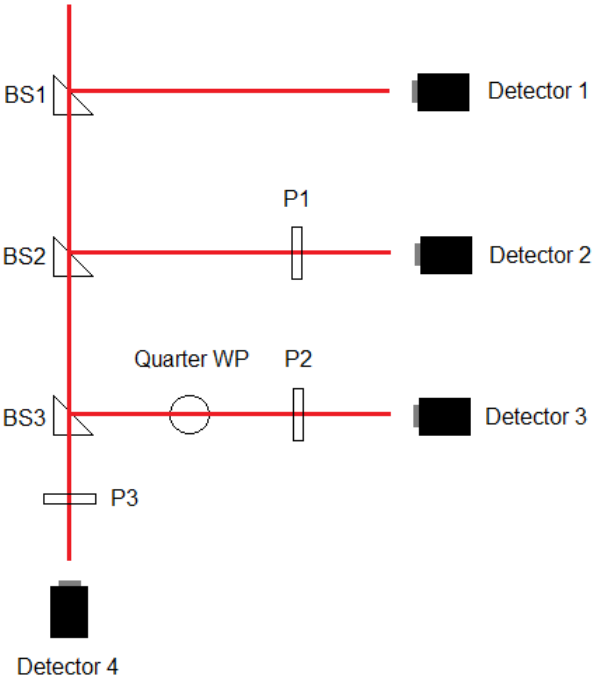

Figure 4.19. Schematic of the optical diagnostic proposed for the measurement of the laser polarisation status after interaction. Each detector measures one of the Stokes parameters. Polariser 1 (P1) should transmit horizontally and polarisers 2 and 3 (P2 and P3) at 45°. The λ/4 waveplate should have a horizontal fast axis.

In this configuration, the following S_0, S_1, S_2 and S_3 specify the polarisation state:

$$\begin{aligned} S_0 &= 2I_1 \\ S_1 &= 2I_2 - 2I_1 \\ S_2 &= 2I_3 - 2I_1 \\ S_3 &= 2I_4 - 2I_1 \end{aligned} \tag{4.23}$$

where I_1, I_2, I_3 and I_4 are the corresponding intensities recorded by each detector. A first measurement without polarisers and waveplate must be obtained to calibrate each detector.

The scalability in energy of the betatron X-ray beams allows for phase-contrast imaging of denser biological materials. For example, phase-contrast imaging of a bone requires a critical energy of ~50 keV. This energy can be achieved with the current LWFA technology.

It has been shown that the interaction of the electrons with the laser pulse [4] in the bubble region can lead to a resonant enhancement of the betatron

amplitude and therefore a higher critical energy of the betatron X-ray beams (50 - 450 keV). This energy can be obtained from 100 TW-scale laser systems such as the ASTRA-GEMINI laser at the Rutherford Appleton Laboratory and the Scottish Centre for the Application of Plasma-based Accelerators (SCAPA) at Strathclyde.

In particular, phase-contrast imaging of micron size cracks in bone using the LWFA is an interesting biomedical application. Bone micro-cracks are related to osteoporosis and bone stress. This increases bone fragility. By detecting and monitoring their growth, it is possible to prevent larger fractures.

Simulations using the Monte Carlo FLUKA code [43] have been performed to prove the feasibility and estimate the resolution limit of the betatron X-ray beams from a LWFA for performing bone micro-crack phase-contrast imaging. For this, a refraction model based on Snell's law has been developed and included in the FLUKA code by Dr Silvia Cipiccia [44].

As indicated above, for phase-contrast imaging of bone a betatron X-ray energy of ~50 keV is required. However, as a first step and proof of principle, a thin section of 200 *μm* of bone has been considered in the simulations.

The parameters of the source used in the simulations have been matched to the ones measured at the ALPHA-X beam line. The energy spectrum used for the simulations is the betatron spectrum, *i.e.*, a synchrotron-like spectrum similar to a conventional synchrotron:

$$E_c \propto \int_{\frac{E}{E_c}}^{\infty} K_{\frac{5}{3}}(\xi)\, d\xi, \tag{4.24}$$

where $K_{5/3}$ is the modified Bessel function of the second kind. The critical energy is set to 15 keV (see Figure 4.20) and the number of particles simulated for each run is 10^9.

To reduce the computational time, the divergence was set to 2 mrad, which corresponds to the detector active area in the simulation geometry. The source-to-sample distance is set to 30 cm and the sample-to-detector distance

to 80 cm. The geometry of the simulation consists of a cylindrical 200 *μm* thick bone tissue. The bone tissue material properties, including density and composition are already implemented in FLUKA. A single cylindrical micro-crack fissure filled with air is placed in the middle of the bone.

Simulated phase-contrast images for different micro-crack thickness are shown in Figure 4.21. The thinnest micro-crack observed with FLUKA corresponds to a radius of 1 *μ*m.

The corresponding convoluted images for a 13 *μ*m pixel size (which is a typical CCD pixel size available) are shown in Figure 4.22.

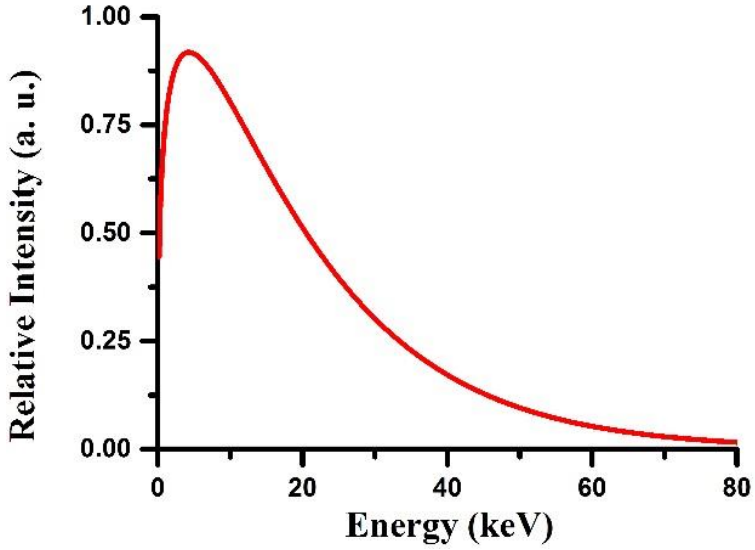

Figure 4.20. Synchrotron-like spectrum used for the phase-contrast FLUKA simulations. The critical energy is 15 keV corresponding to a peak energy of about 4 keV. From [40].

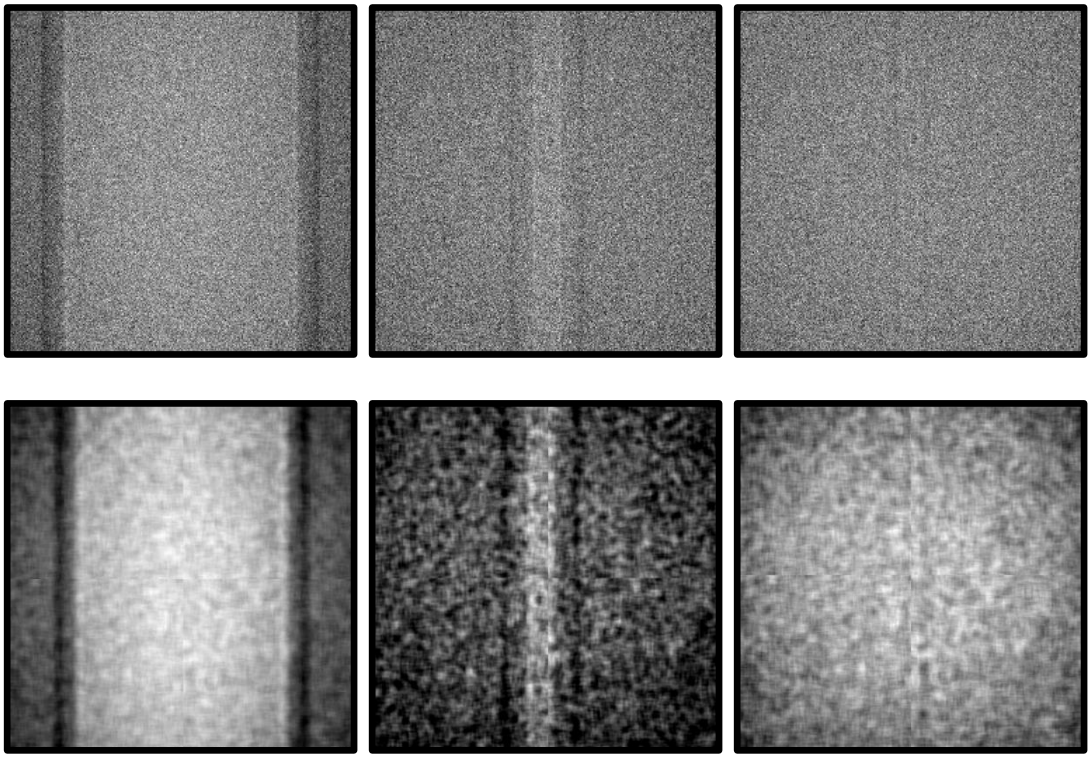

Figure 4.21. Top: Simulated phase-contrast images for bone micro-cracks of 25, 5 and 1 µm radius size respectively from left to right. Bottom: corresponding convoluted images for a 13 µm detector pixel size. From [40].

If the number of projections is high enough it is possible to perform tomographic studies and 3D reconstruction of thin bones. This is shown in Figure 4.22 where a single projection, a tomogram (slice) and the corresponding 3D reconstruction of a thin bone with a crack can be seen. The bone diameter is 100 *µm* and the micro-crack (fissure) diameter is 40 *µm*.

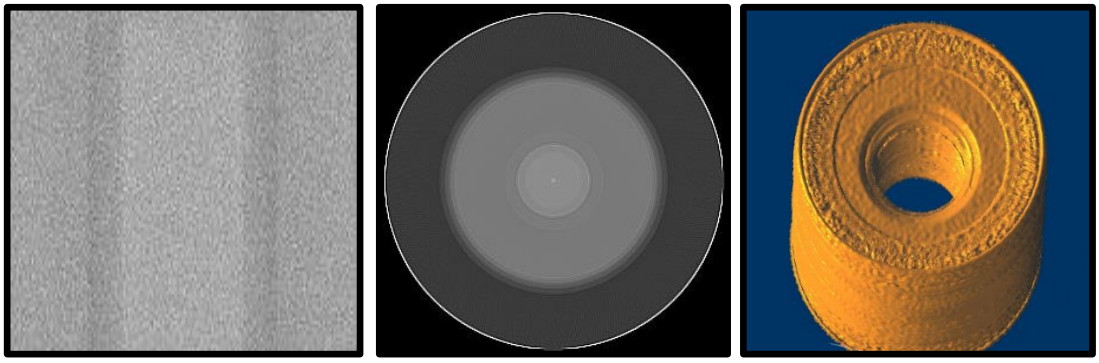

Figure 4.22. Examples of projection (left), tomogram (centre) and 3D reconstruction (right) of a FLUKA simulated 100 µm diameter bone with a 40 µm micro-crack. From [40].

To process the projections to obtain the slices, an in-house developed tomography software package based on filtered back projection algorithm is used. This software package has been developed by Dr Dima Maneuski. The 3D reconstruction was performed using the imageJ [45] 3D volume viewer plugin.

The filtered back-projection is a more sophisticated version of the back-projection or simple back-projection technique. It is the most commonly used algorithm for computed tomography systems.

The back-projection method involves acquiring a set of views of a certain object at different angles. After this, each view is back-projected by spreading it back along the path it was acquired in the first instance. Finally, all the back-projections are added in order to obtain the final back-projected image. This can be seen in Figure 4.23.

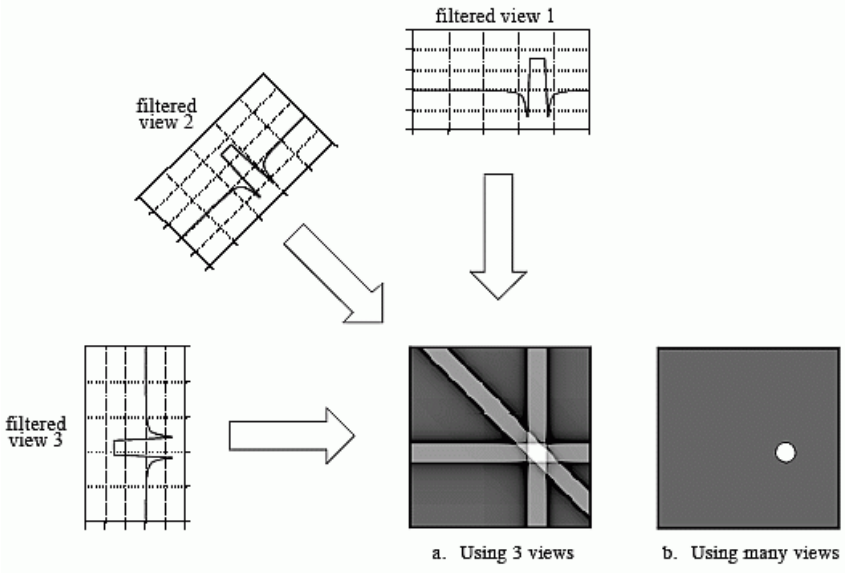

Figure 4.23. Schematic of the filtered back-projected method. Each view is filtered before being back-projected to avoid blurring. From [46].

The problem of this technique is that the back-projected images are normally blurred. To solve this problem, each view can be filtered before taking the back-projection, *i.e.*, each view is convolved with a filter. After the convolution, the views are back-projected. The reconstructed image will be exactly equal to

the “true” image when an infinite number of views are taken. This method is called the filtered back-projection method.

Another interesting feature of the betatron X-ray beams, which has not been mentioned yet and is worth to note, is its femtosecond pulse duration [2]. This ultrashort duration may find uses in a wide variety of applications where motion blur is a problem. This is not possible with conventional synchrotron sources.

4.5 Laser-driven XPCi applications

4.5.1 Introduction:

In the previous section we focused on measuring the main parameters of the betatron X-ray source of the ALPHA-X laboratory. In the following experiments, the betatron X-rays have been used to explore two imaging applications. Concretely, the betatron X-rays have been used to explore the potential of LWFA for microscopic and tomographic applications.

These experiments have been undertaken after the upgrade of the ALPHA-X laser system mentioned in Chapter 3 (in April 2014). An extra pump laser has been included in the final amplifier. This yields a total laser energy before pulse compression of 2 J. The energy on target after the losses in both compressor and transport optics is of the order of 1 J.

This important change in the final amplifier of the laser system required an additional characterisation of the betatron X-rays prior to the applications experiments.

The structure of this section is the following: first the experimental setup and the betatron X-ray characterisation are shown. The second part focuses on the microscopy and tomography experiment. The last part discusses the results of the experiments and gives conclusions.

4.5.2 Experimental setup and betatron X-rays characterisation:

The experimental setup for the characterisation of the X-ray and electron beam is similar to the one shown in Figure 4.9. However, in this case, the laser

energy is 1 J, while the pulse duration, spectrum and spot size remain the same. These laser parameters correspond to a peak intensity of $I = 2.3 \times 10^{18}\ \mathrm{Wcm^{-2}}$ on target.

Similar to the previous experiments, the nozzle 511 model described in Chapter 3 of this thesis is used. The height between nozzle and laser beam is set to 4 mm because this provides the most stable electron beam. The backing pressure is set to 45 bar, corresponding to a plasma density of $1.5\times10^{19}\ \mathrm{cm^{-3}}$. This plasma density has been estimated using FLUENT simulations, which can be found in Chapter 3 of the thesis.

A more powerful vacuum pump for the interaction chamber has been installed allowing a higher repetition rate of 0.5 Hz, and 1 Hz for short experimental runs.

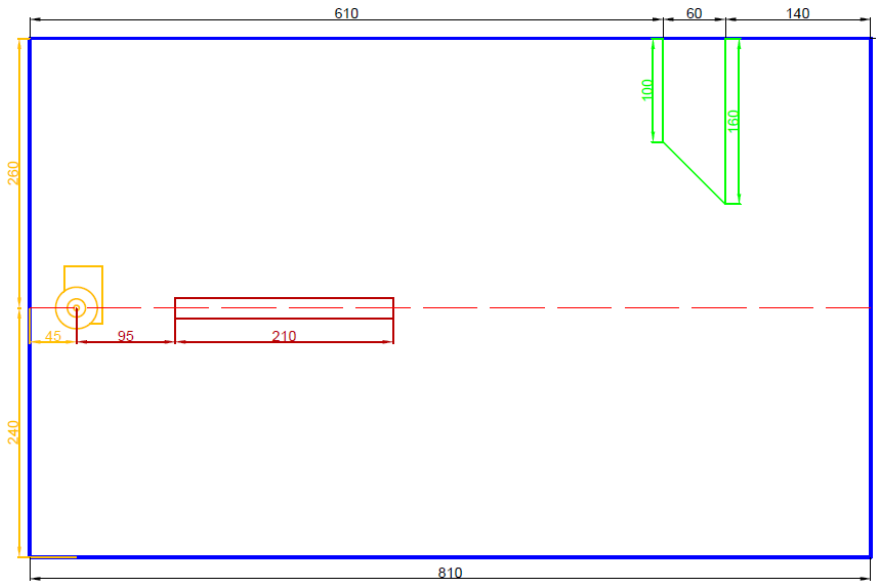

Figure 4.24. Chamber layout with the relevant distances. In yellow the gas jet, magnet in red and lanex screen in green.

As in the previous experiment, a 0.7 T bending magnet is placed on a motorised stage inside the interaction chamber just after the gas-jet to deflect the accelerated electron beam away from the laser axis as soon as it is generated, which minimises the amount of bremsstrahlung on axis. This allows an estimate of the electron beam energy as well as monitoring of the electron beam. For this experiment, the bending magnet is placed closer to the gas jet

to reduce clipping of the x-ray beam on the bending magnet, which occurred in the previous experimental run.

The deflected electrons are detected using a scintillating LANEX phosphor screen (see Figure 4.24), as in the previous experiment, and the energy spectrum is measured. The length of this screen is 8 cm and has been calibrated performing a Monte Carlo FLUKA simulation. Both calibration and geometry of the simulation can be found in Figure 4.25.

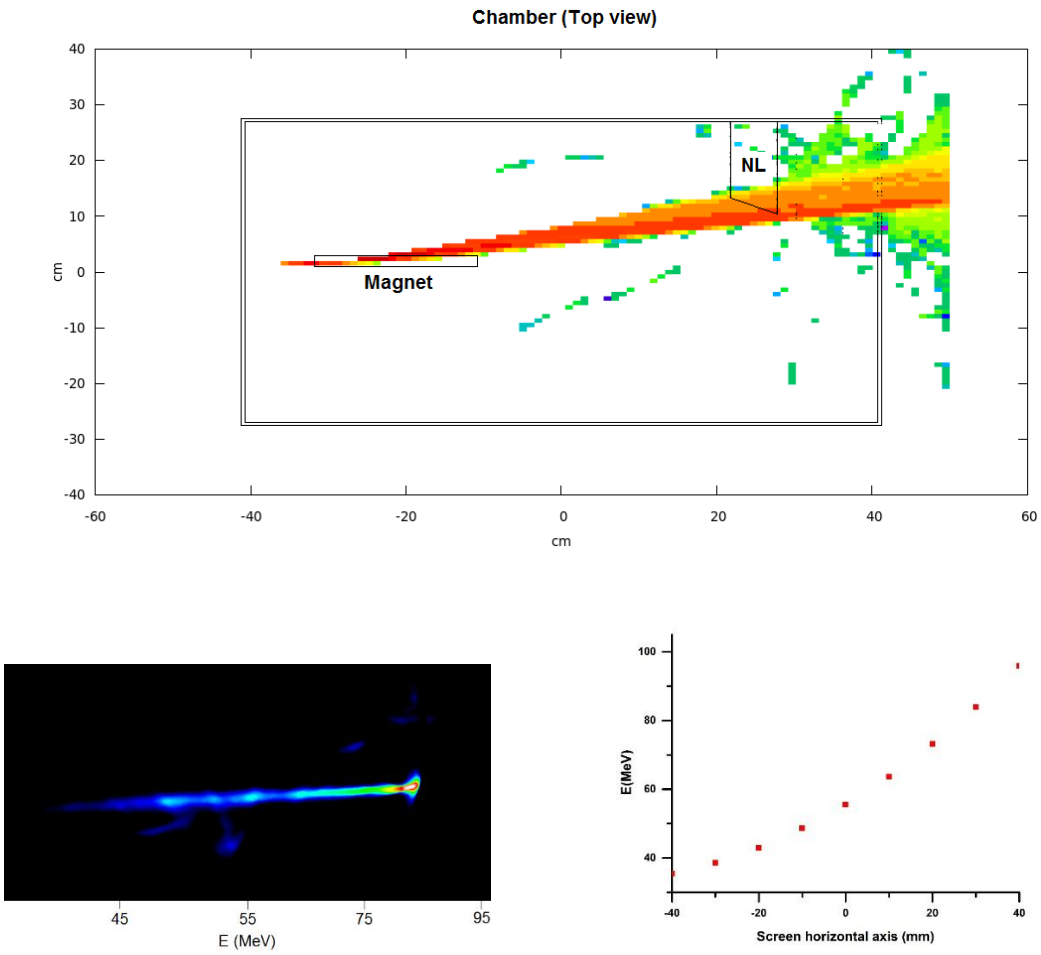

4.25. Top: geometry of the Monte Carlo simulation for lanex screen calibration. Bottom left: false colour image showing an example shot of the electron beam on the lanex screen. Bottom right: calibration curve for electron energy estimation.

The peak electron beam energy for this experimental run is estimated to be 84 ± 11 MeV. The electron beam charge is estimated using imaging plates before and after carrying out the imaging experiments. An average charge of 3.1 ± 1.2 pC per laser shot is estimated. The measurement are carried out just after

the interaction chamber. The electron beam energy and charge were measured every day and the results were always in the same range mentioned in this paragraph.

The X-ray spectrum measurements and the imaging experiments have been performed using an X-ray charged-coupled device manufactured by ANDOR. The CCD (Ikon-M BN) is cooled to -100°C to provide low readout noise, therefore increasing the quality of the measurements.

An important feature of these detectors is their small pixel size. The Ikon-M series have a pixel size of 13 μm. The size of the Si sensor is 13.3x13.3 mm^2 giving a total number of pixels of 1024x1024. This small pixel size makes this detector a good option for microscopy.

This detector also provides a good quantum efficiency in the soft X-ray (1-10 keV) range. This can be seen in the following Figure:

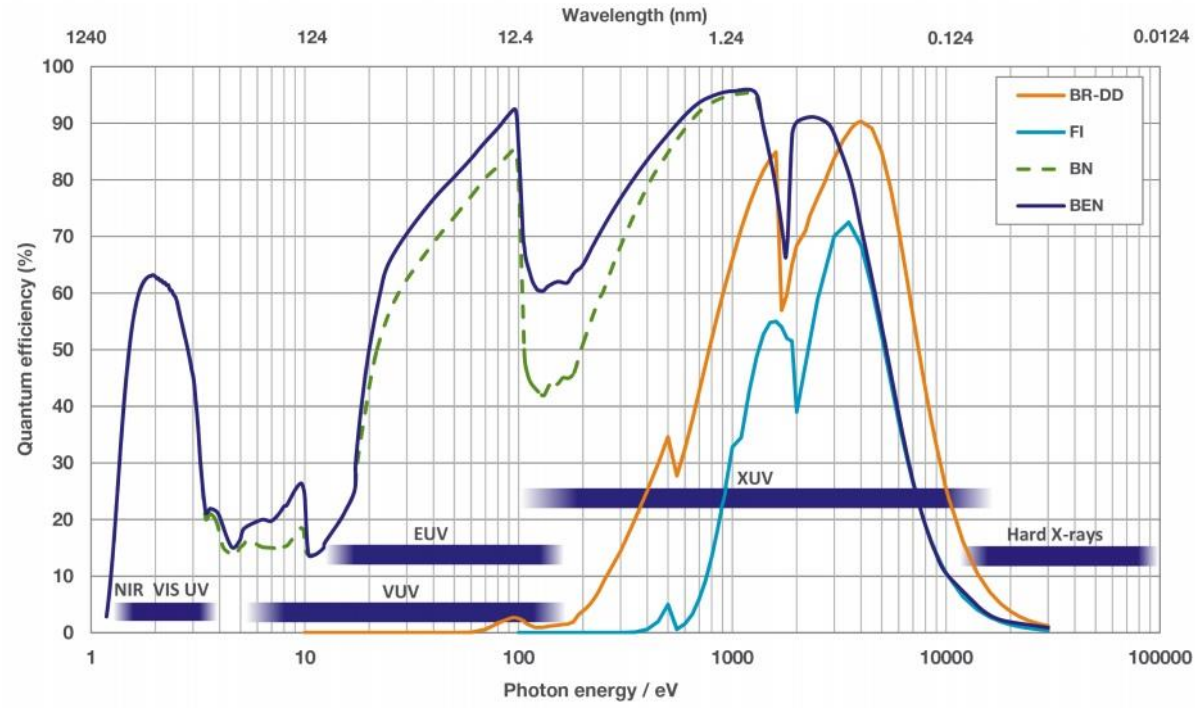

Figure 4.26. quantum efficiency as a function of X-ray energy for ANDOR Ikon-M series. The BN model is the one used in this thesis.

Since the Andor efficiency is lower than Timepix for this range of energy, filters are not required in front of the detector.

Unlike Timepix, this kind of detector is used in vacuum and comes with a knife-edge sealed flange, which provides an effective vacuum seal.

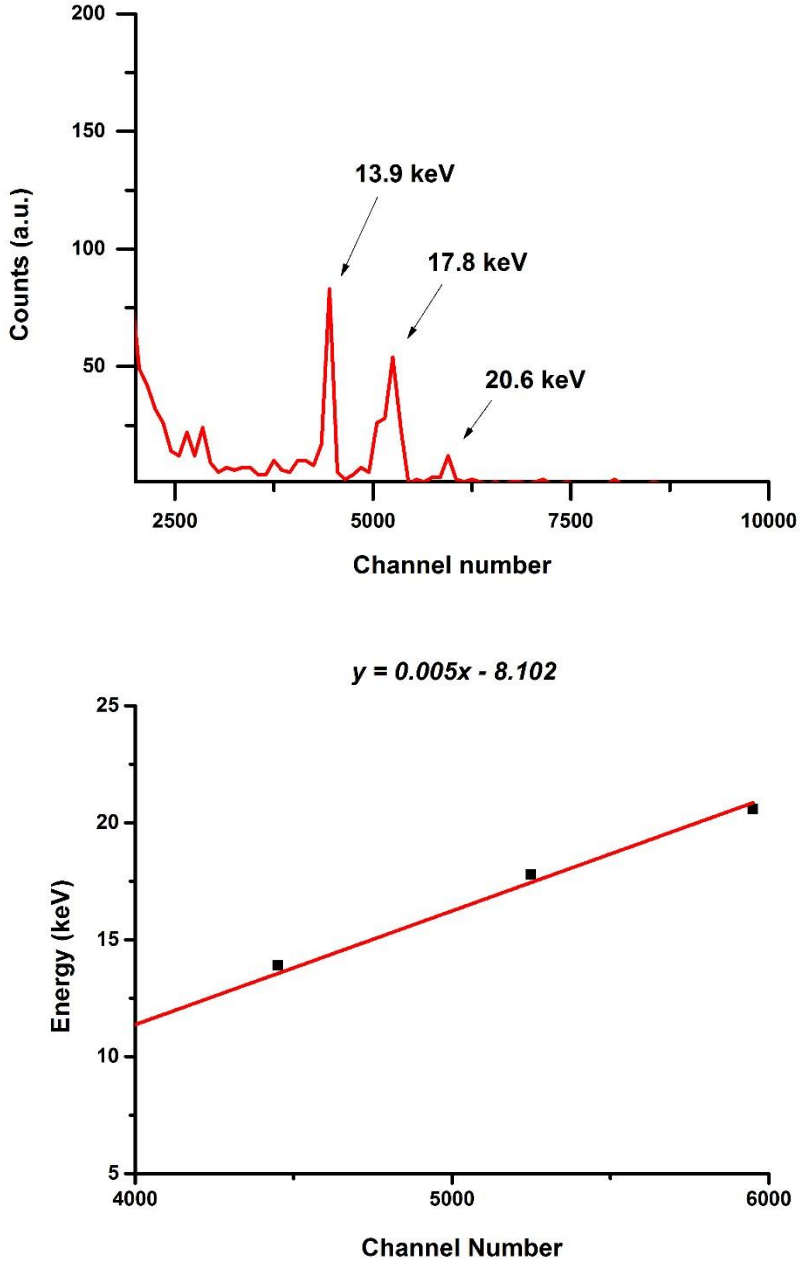

Figure 4.27. Top: Am-241 raw spectrum measured with the ANDOR camera. Bottom: energy calibration equation obtained for the X-ray detector.

The X-ray camera was calibrated before the experiment using a similar method to the calibration of Timepix. In this case, the camera is attached to a short vacuum pipe, which is closed by a thin (3 mm) Perspex window. The whole

setup is kept in vacuum using a small dry pump. The sealed source is then attached to the Perspex window.

The same americium source (Am-241) used for the calibration of Timepix is used for calibrating the ANDOR camera without placing an Al filter in front of the detector. The americium source provides three spectral peaks at 13.9, 17.8 and 20.6 keV. The ANDOR camera has a thinner sensor than Timepix. Because of this, the efficiency at higher energy is reduced and therefore the 26 and 60 keV peaks cannot be used for the calibration.Since the quantum efficiency of this camera at this energy is low (less than 10% according to the manufacturer's specification) the camera is left recording overnight to obtain a good signal. The measured spectrum and the calibration curve is shown in Figure 4.27.

The characterisation of the X-ray source after the upgrade of the laser system has been performed in a similar way to the previous experiment described in section 4.4. The most stable electron beam was obtained for a height between nozzle and laser beam of 4 mm. The optimum gas backing pressure is found to be 45 bar, corresponding to a plasma density of $1.5\times10^{19}\ \mathrm{cm}^{-3}$.

The spatial distribution has been measured using imaging plates placed just after the interaction chamber. Five sets of measurements, each corresponding to the accumulation of 100 laser shots, have been performed. The half-angle divergence has been estimated at 101.1 ± 10.6 mrad using the same method described in the previous section. An example spatial distribution on an imaging plate is shown in Figure 4.28.

The divergence is larger than in the previous experiment. Unlike the previous experiment where the spatial distribution measurements have been performed in single shot. In this case the spatial distribution measurement corresponds to an accumulation of 100 laser shots, thus the larger divergence can be explained by variations in X-ray beam pointing (see Figure 4.15 in the previous section).

The image plates have also been used to do a quick estimation of the critical energy using metal filters, following the same method used in the previous experiment. The critical energy is 5.6 ± 2.2 keV, obtained from the average of 5 sets of measurements, each corresponding to the accumulation of 100 laser shots per measurement. An example metal filter image can be seen in Figure 4.28.

The X-ray spectrum has been measured using the ANDOR camera described above. As previously explained, these detectors work in vacuum. For this reason, the camera is attached directly to the beamline after the electron spectrometer (see Figure 4.29). The beamline is then evacuated using two small turbo pumps.

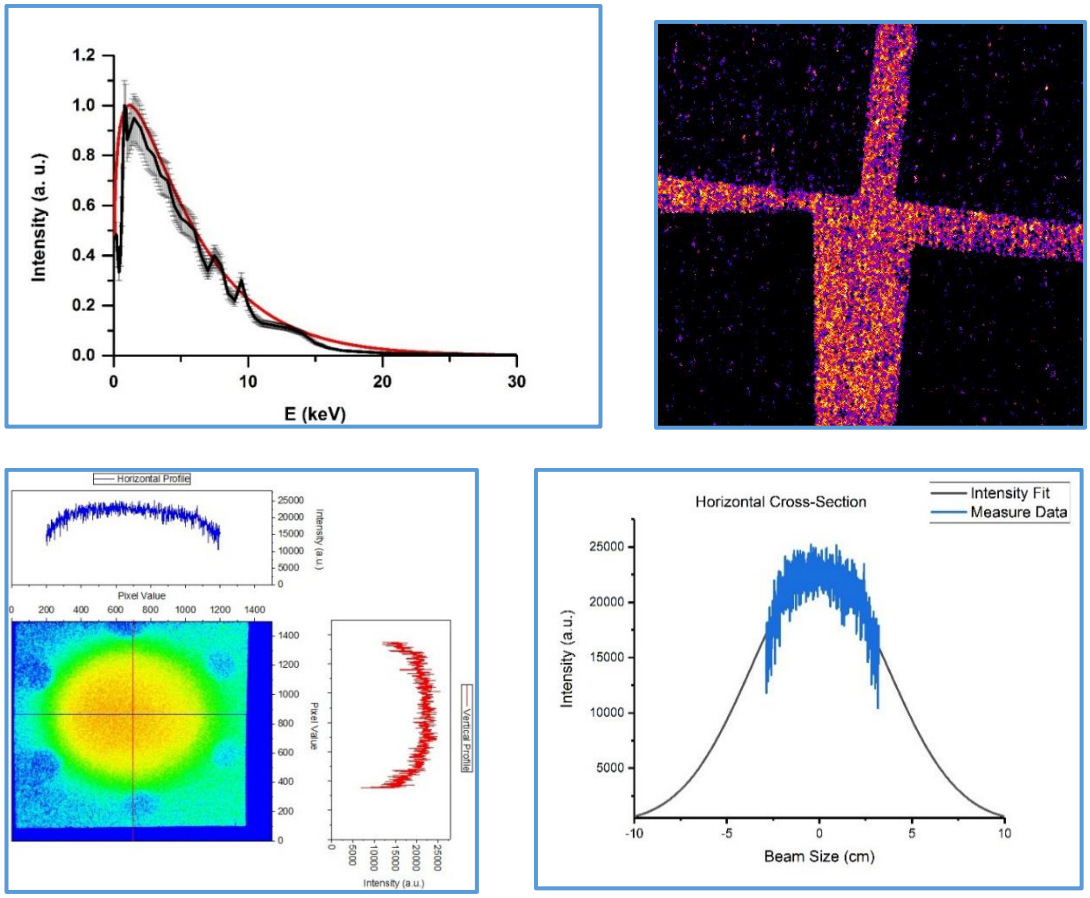

Figure 4.28. Top left: X-ray spectrum recorded with the ANDOR camera. The spectrum is corrected for the attenuation of the Al filter and quantum efficiency. The shaded grey area gives the measurement error. Top right: false colour image of the shadow left by metal filters on imaging plate after 100 laser shots. The top left one corresponds to Ag 0.05 mm, top right 0.5 mm Al, bottom right Ti 0.1 mm and bottom left 0.1 mm. Bottom left: false colour image showing the X-ray spatial distribution averaged over 100 shots. Bottom right: horizontal profile fitted to equation 4.14.

To block the laser and prevent damage to the detector, an aluminium filter is placed in a retractable pop-in actuator just before the beamline electron spectrometer.

Figure 4.28 shows an example of the recorded X-ray spectrum, corresponding to an accumulation of 1000 laser shots. The analysis of the data is undertaken using the same procedure as for the previous experiment. A fit based on a synchrotron-like spectrum indicates a critical energy of 4.1 keV, in good agreement with the result obtained from the metal filters.

4.5.3. Laser-driven phase-contrast microscopy of thin wires

After the re-characterisation of the X-ray source, an experiment has been setup on the ALPHA-X beamline to explore the potential of the betatron X-ray source for phase-contrast microscopy. For this purpose, a set of thin wires are inserted into the beamline and imaged using the ANDOR X-ray camera. The wires comprise a 300 μm nylon wire, 50 μm Ni, 25 μm Cu, 10 μm Cu, according to manufacturer's specifications, and a strand of hair. The phase-contrast imaging technique used is free space propagation because of the poly-chromaticity of the X-rays and the simplicity of the method.

To study the effect of the object-detector distance on the image contrast, the wires are inserted at three different positions in the beamline. Unlike the Timepix experiment, the beamline is evacuated because the critical energy of the X-rays is lower and the number of photons is lower (which can be observed from the fact that it has not been possible to acquire single shot metal filter images as in the Timepix experiment). This avoids attenuation from the air and allows more photons to reach the ANDOR X-ray camera. The experimental setup is shown in the following Figure:

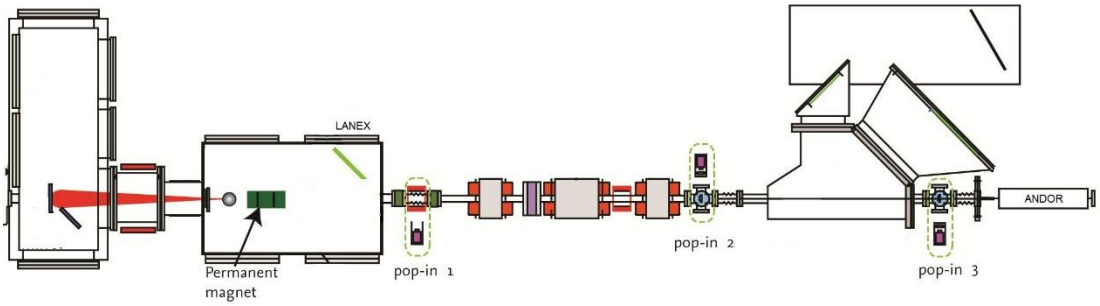

Figure 4.29. Schematic of the XPCi experiment using the X-ray beam source produced on the ALPHA-X beamline. The wires have been inserted, in turn, in pop-in actuators 1, 2 and 3. The source-detector distance has been kept constant and equal to 3.4 m. The object-detector distance when the wires are inserted in pop-in 1, pop-in 2 and pop-in 3 are 2.35 m, 1.10 m and 0.25 m respectively.

The permanent magnet is still used to bend the electrons away and the lanex screen remains in the same position for electron beam monitoring purposes. The distance between the source and the ANDOR camera is 3.4 m and is kept fixed for the whole experiment. The distance between object and detector is different for each case. The following table summarises the object-detector distances and corresponding magnifications for each case:

Table 4.5. Summary of object-detector distances and corresponding magnification depending on the wires position.

	Object-detector distance (m)	**Magnification**
Pop-in 1	2.35	3.2
Pop-in 2	1.10	1.5
Pop-in 3	0.25	1.1

The resolution of the image is set by the pixel size of the ANDOR camera, which is 13.3 μm. For the given magnifications this allows resolution of details down to ~4 μm when wires are in pop-in 1, ~9 μm in pop-in 2 and ~11 μm in pop-in 3. The transverse coherence length can be calculated using equation 4.21. For a 4 keV X-ray energy, 1 μm source size and 3.40 m source to detector distance this is ~1 mm.

The number of laser shots used for each position of the wires in the beamline is 2000. The conditions of the experiment remained constant for the three

positions, *i.e.*, height between nozzle and laser 4 mm and backing pressure 45 bar (1.5×10^{19} cm^{-3}).

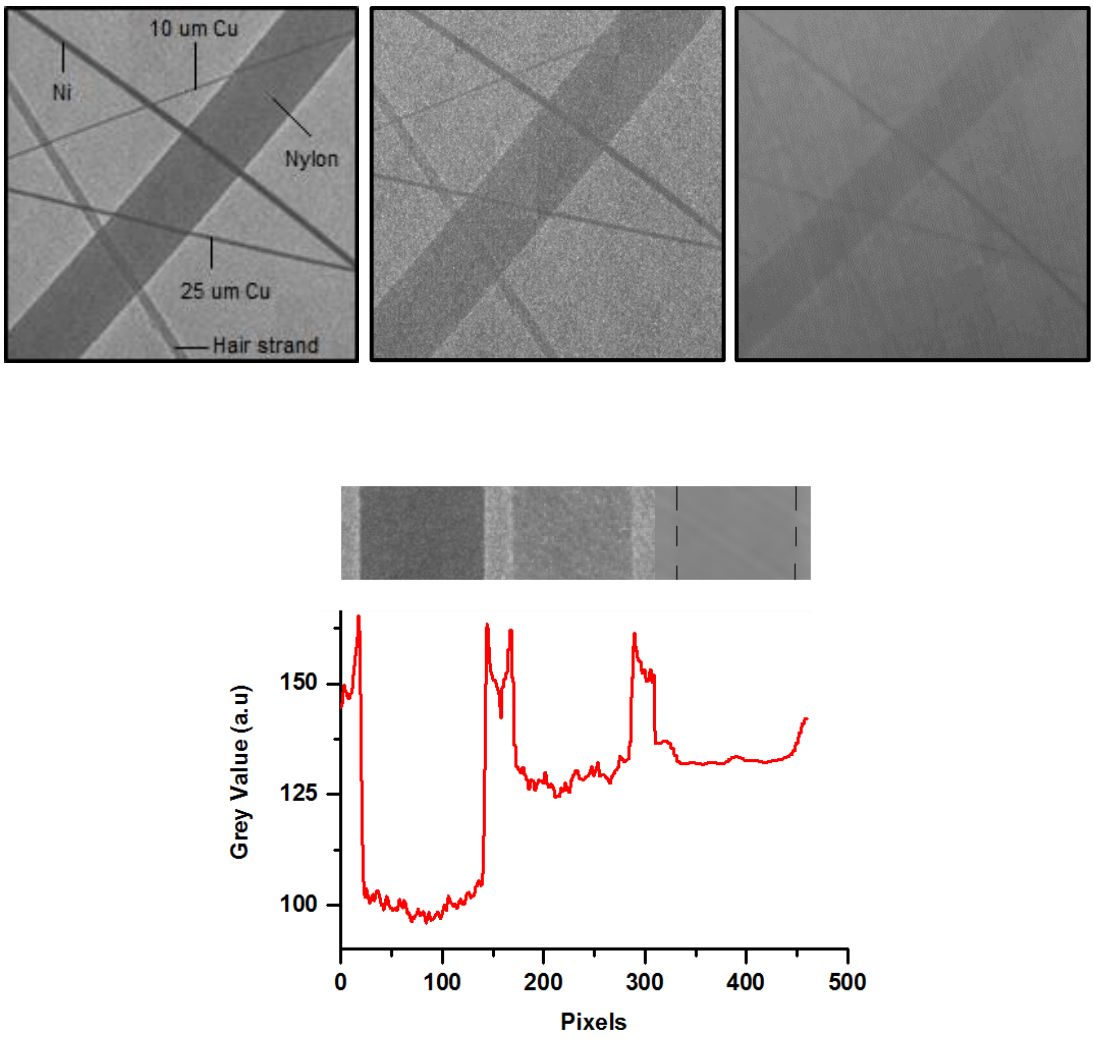

Figure 4.30. Top: image obtained after 2000 shots for wires placed in pop-in 1 (left), pop-in 2 (centre) and pop-in 3 (right). Bottom: Line out of the nylon wire when imaged by the X-rays in each of the three pop-ins (left 1, mid 2, right 3) in turn.

It is possible to observe the influence of the object-detector distance in the top images of Figure 4.30. When the wires are placed in pop-in 1, further away from the detector, the contrast is highly enhanced. However, when the object is placed in pop-in 3 the distance between object and detector is not long enough for phase-contrast to develop effectively and only absorption contrast is recorded. When the wires are placed in the pop-in 2 an intermediate situation occurs with the image showing a higher contrast than in pop-in 3 but lower than in pop-in 1.

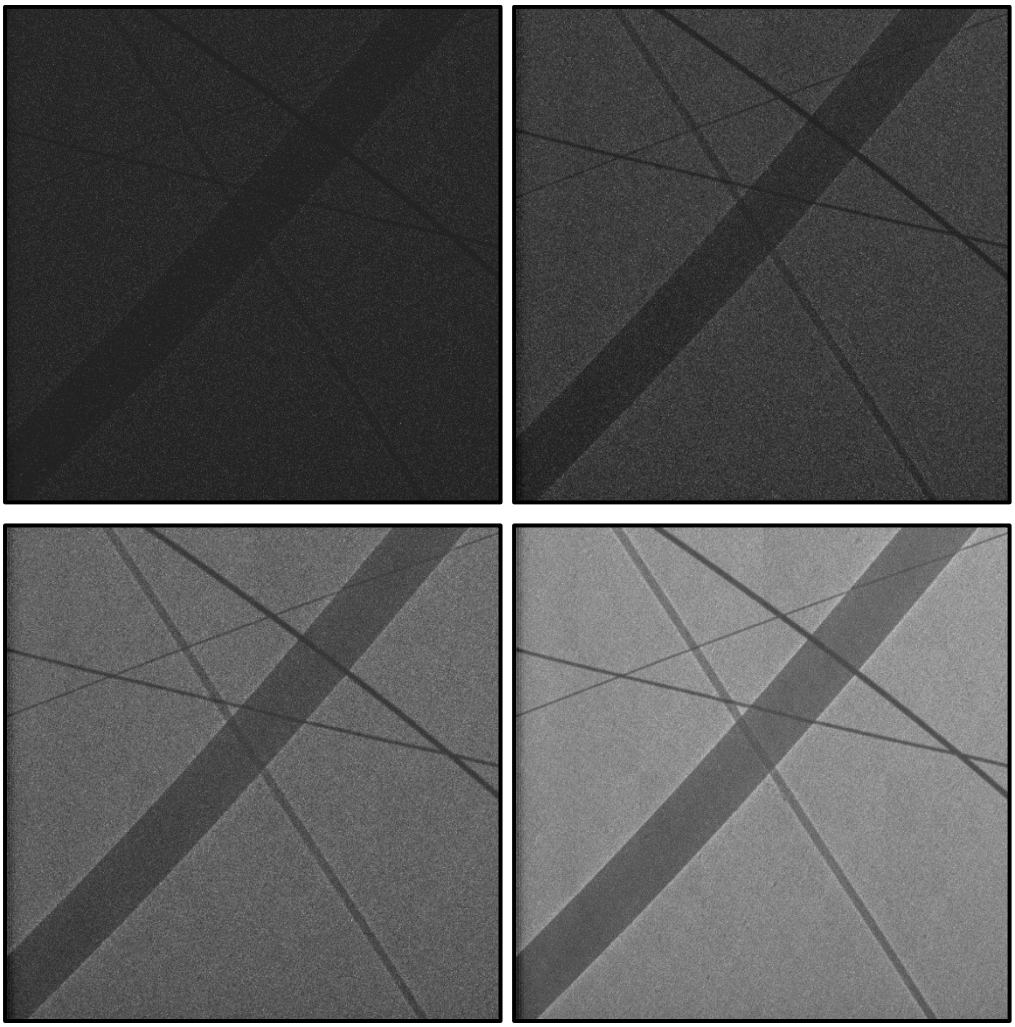

Figure 4.31. Top left: image recorded of wires in pop-in 1 after 50 laser shots. Top right: image recorded of wires in pop-in 1 after 200 shots. Bottom left: image recorded of wires in pop-in 1 after 500 laser shots. Bottom right: image recorded of wires in pop-in 1 after 2000 laser shots.

The contrast can be calculated using equation 4.22. For the nylon wire, it is 0.26 when the wires are placed in pop-in 1. When the wires are placed in pop-in 2 the contrast goes down to 0.12. For the wires placed in pop-in 3 the contrast goes down to 0.02. For this source-detector distance in particular, a change on the object-detector distance of 1 m means 6 times less contrast.

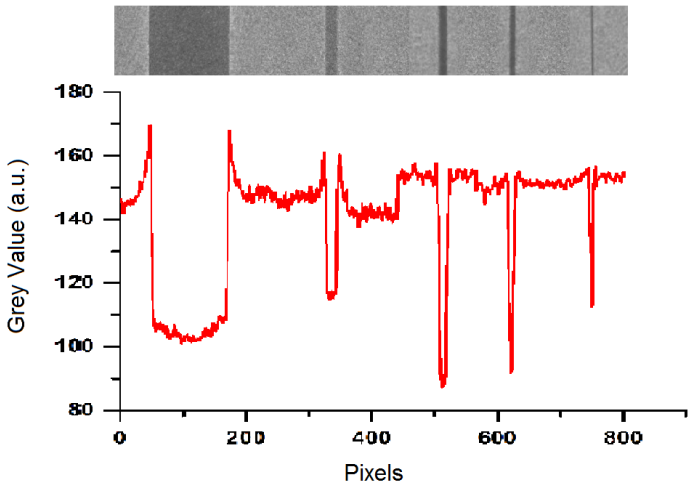

Figure 4.32. Line out of wires imaged by the betatron X-rays when placed in pop-in 1. From left to right, 300 μm nylon, hair strand, 50 μm Ni, 25 μm Cu and 10 μm Cu wire.

The edge enhancement is stronger in the nylon wire and in the hair strand than in the Ni and Cu wires. This can be observed in the line out showed in Figure 4.32, which corresponds to the wires placed in pop-in 1. This is due to the fact that both nylon and hair are light materials. In the case of Ni and Cu, the absorption contribution to the image will be higher.

4.5.4. Laser-driven micro-tomography feasibility study:

After showing the feasibility of the ALPHA-X betatron X-ray source for microscopic studies, the next step is to explore the possibility of using the X-ray source for micro-tomography applications. In this section, an absorption based tomography is presented.

Recently, the use of a gas cell to produce 50 keV critical energy betatron X-rays for tomographic studies of bone has been demonstrated [47] using the Astra-Gemini laser at the Rutherford Appleton Laboratory. Full tomography of insects has also been demonstrated, [48] using gas cells.

Here we explored the feasibility of employing betatron radiation to perform tomographic studies of smaller samples. In this case, the object of study is a set of two wires that form the ALPHA-X logo shape. The wires used are 50 μm tungsten and 300 μm nylon wires, according to manufacturer's specifications. This object is chosen for simplicity as a proof of principle experiment.

The experiment is performed in the ALPHA-X beamline under the same experimental conditions (in terms of electron and X-ray beams) described from section 4.5 onwards. To reduce the attenuation of X-rays in air, the beamline is evacuated, except for a short gap were the sample to be imaged is inserted. The two ends are closed using 25 μm thick mylar windows, instead of thicker Perspex, to reduce transmission losses. A 25 μm Al foil is inserted just before the ANDOR camera to prevent laser damage.

The permanent magnet deflects the electron beam onto the previously described Lanex screen, which is imaged using a 12 bit Point Grey Research Flea camera. The X-ray beam propagates through the sample, which is placed on a rotation stage. The level of the rotation stage is checked with a spirit level.

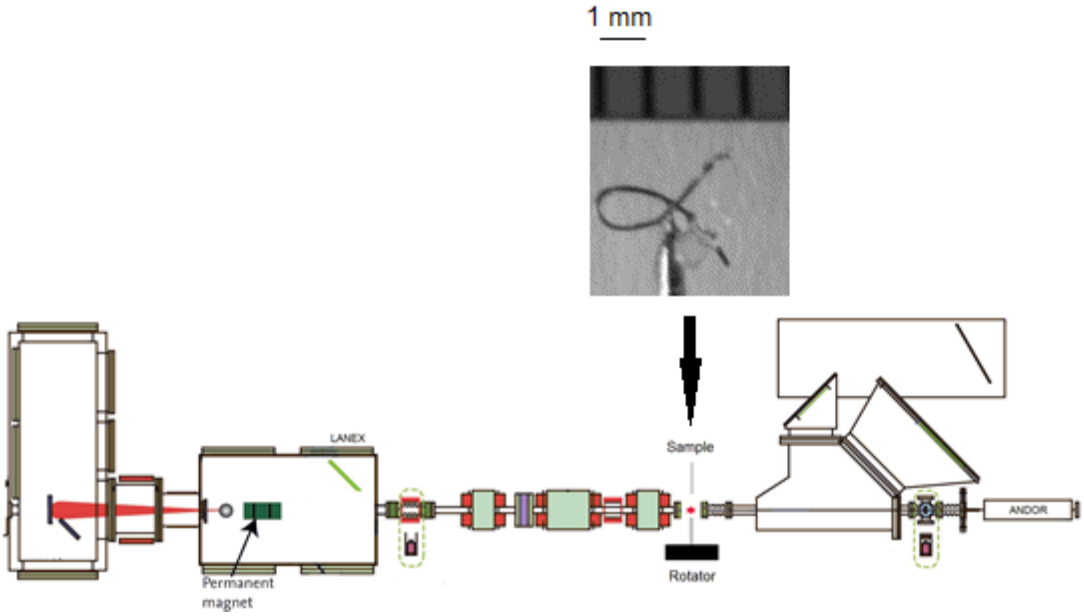

Figure 4.33. Experimental setup for the microtomography experiment. The sample is placed in a short air gap of 5 cm between vacuum pipes. The ANDOR camera is set at the end of the beamline.

The distance between sample and detector is set to 1.10 m and the source to detector distance is 3.40 m, which yields a magnification factor of 1.5. The X-ray projections are measured mainly at intervals of 5 degrees from 0 to 140° and from 270° to 360°. A total number of 41 projections are recorded. Each projection is recorded using 500 laser shots at a repetition rate of 0.5 Hz. This gives an irradiation time of 16.5 minutes per projection and a total experimental irradiation time of 11.3 hours.

The following Figure shows raw projections recorded during the experimental run:

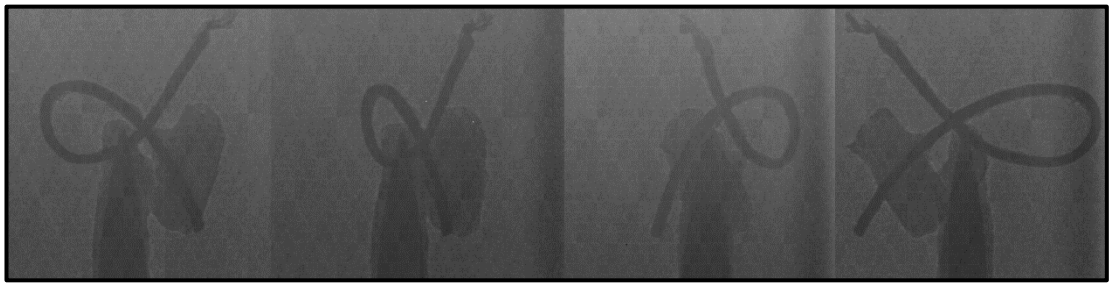

Figure 4.34. Four raw projections recorded by the ANDOR X-ray camera during the micro-tomography experimental run. It can be seen that the contrast changes between projections.

Prior to performing the reconstruction, the raw projections are corrected using the flat field correction method. In X-ray CT scanning, fixed-pattern noise degrades the spatial resolution and leads to artefacts in the reconstructed images. This noise can be removed using the flat field correction technique, which is commonly used in computed tomography.

In the flat field correction technique, images without an object present are taken with and without the X-ray beam on. These images are called flat fields (FF) and dark fields (DF). Based on these images each projection (P) taken with the object in position can be normalised to a new image (N) using the following equation:

$$N = \frac{P - DF}{FF - DF}. \tag{4.25}$$

The main problem of the flat field correction technique is that it relies on the stability of the X-ray source and detector sensitivity. Two examples of projections with and without correction are shown in the following Figure:

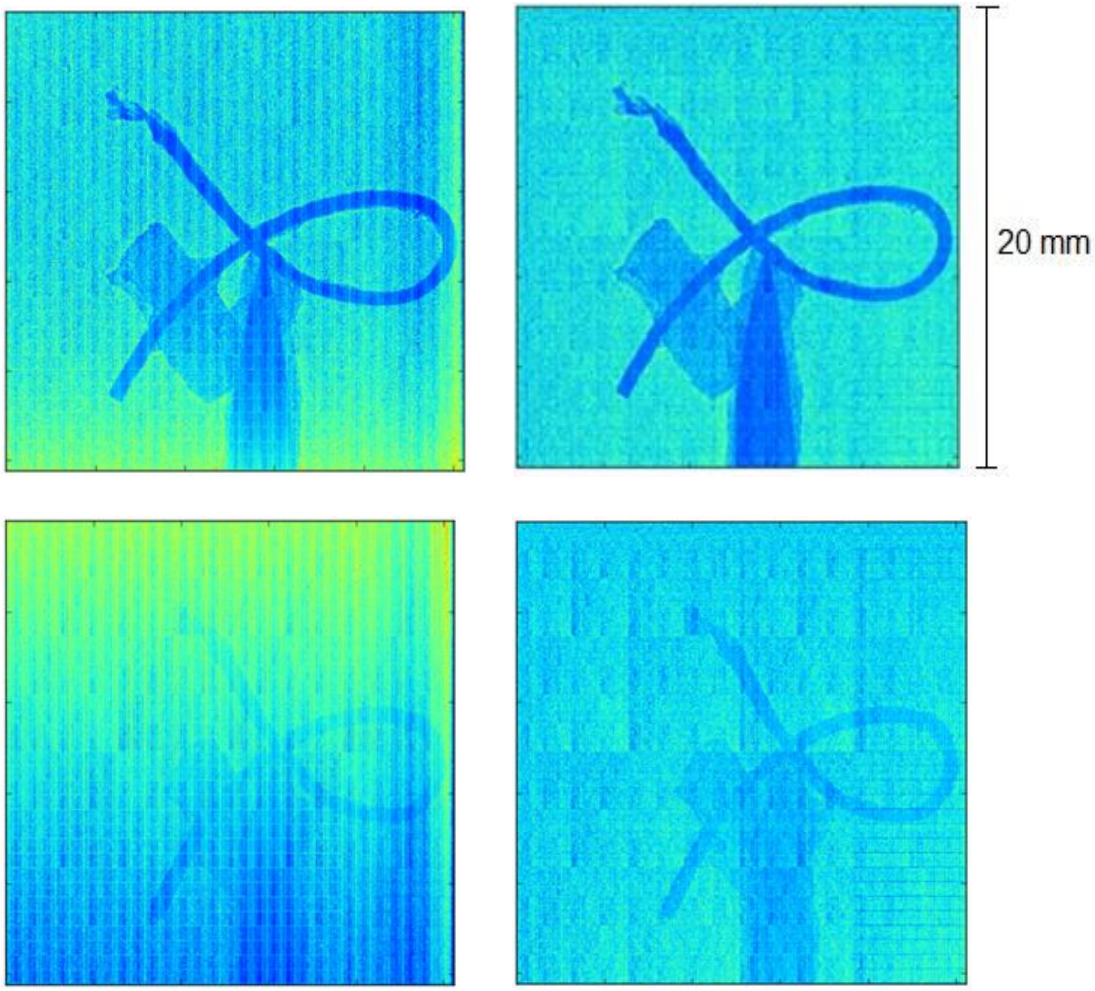

Figure 4.35. Left: two examples of raw false colour projections without flat field correction. Right: same projections corrected using the flat field technique.

From Figure 4.35. it can be seen that in this case the flat field correction improves the projection images. However, it is clear that the contrast generated by the sample varies strongly between projections. This is due to the long irradiation time required for each projection, as well the total duration of the experiment. The LWFA relies on the stability of the high power laser system. Small changes in temperature or small vibrations in the laser room can slightly misalign the laser system. This is very likely to occur in long experimental runs like the one described here, leading to fluctuations in both electron and X-ray beams, which affect the contrast of the projections.

Although the number of acquired projections is small and the quality of the images is not optimum (even after flat field correction), the reconstruction of

the object has been successful. This has been performed by Dr Silvia Cipiccia. The software used for the tomographic reconstruction was Tomopy [49]. The rendered 3D reconstruction was performed using Avizo 3D visualisation software [50].

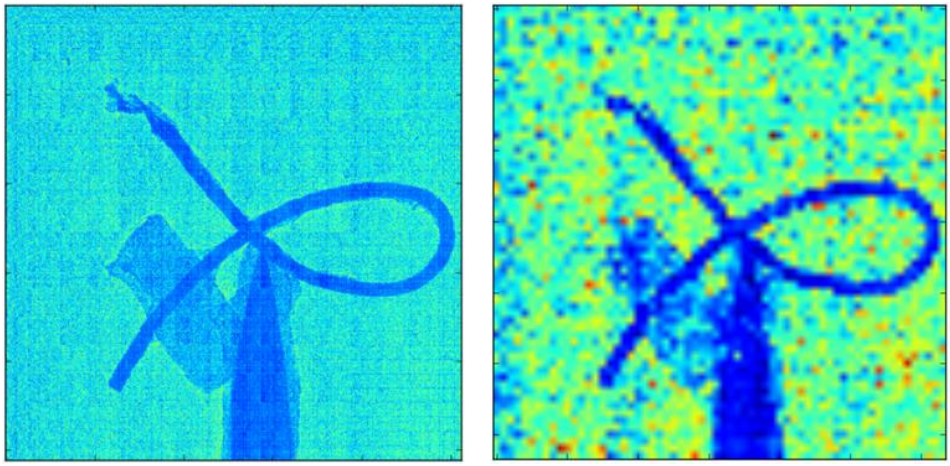

Figure 4.36. Left: example of unbinned projection. Right: same projection binned to 64x64.

In order to obtain an optimum tomographic reconstruction of the object the projections are usually taken at equally spaced angles. Moreover, the number of projections has to be bigger or at least equal to the number of pixels of the image [51]. This is not the case in this experiment for obvious time constraints due to the long exposure time required per projection. Therefore, the reconstruction is in this case under-sampled.

A solution to this is to bin the images. In this case, all the projections have been binned to 64x64 pixels. An example of one binned and un-binned projection can be seen in Figure 4.36.

Since the number of projections is low, an iterative reconstruction algorithm has been used. For this reconstruction, the iterative algorithm used in Tomopy is the osplm_hybrid. The python source code of this algorithm can be found in the Tomopy documentation [49].

Iterative algorithms search for the correct solution by performing multiple iteration steps. In general, this yields a better reconstruction than using back-

projection methods, although at the cost of longer computational times. For this reconstruction, a total number of 150 iterations have been used.

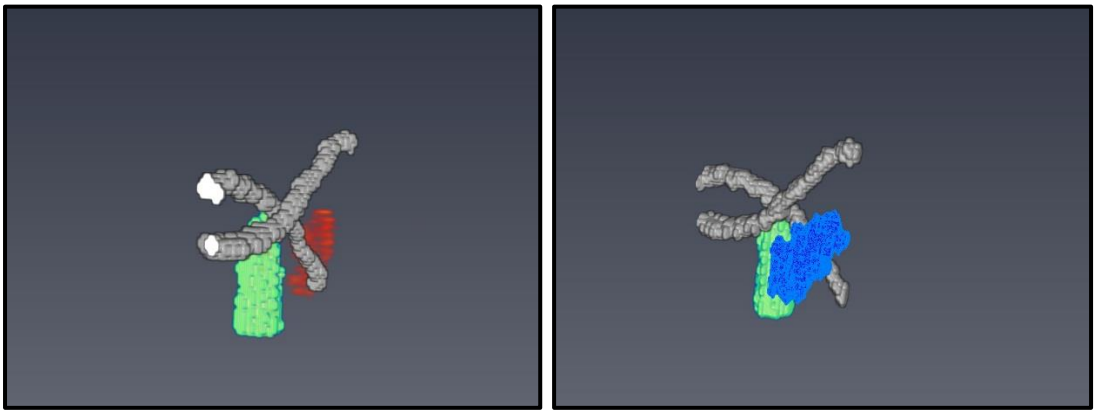

Figure 4.37. 3D reconstruction performed using the betatron X-rays produced at the ALPHA-X beam line. Tomopy and Avizo softwares have been used for the reconstruction. The iterative reconstruction method has been used with a total number of 150 iterations.

Although there are a wide variety of iterative algorithms, they always start with an assumed image. From this assumed image, the algorithm computes projections which are then compared to the measured set of projections. Finally, the initially assumed image is updated based on the difference between the calculated and the measured projections.

Figure 4.37 shows the 3D reconstruction achieved. A total number of 64 cross-sectional slices of 203 μm thickness have been put together to perform the reconstruction. The whole of the alpha-shaped wire is not observed due to a displacement in the rotation axis meaning this in some of the projections the wire is outside of the field of view.

Figure 4.38 shows an example of frontal, coronal and sagittal views similarly to the ones that would be obtain from a CT scan.

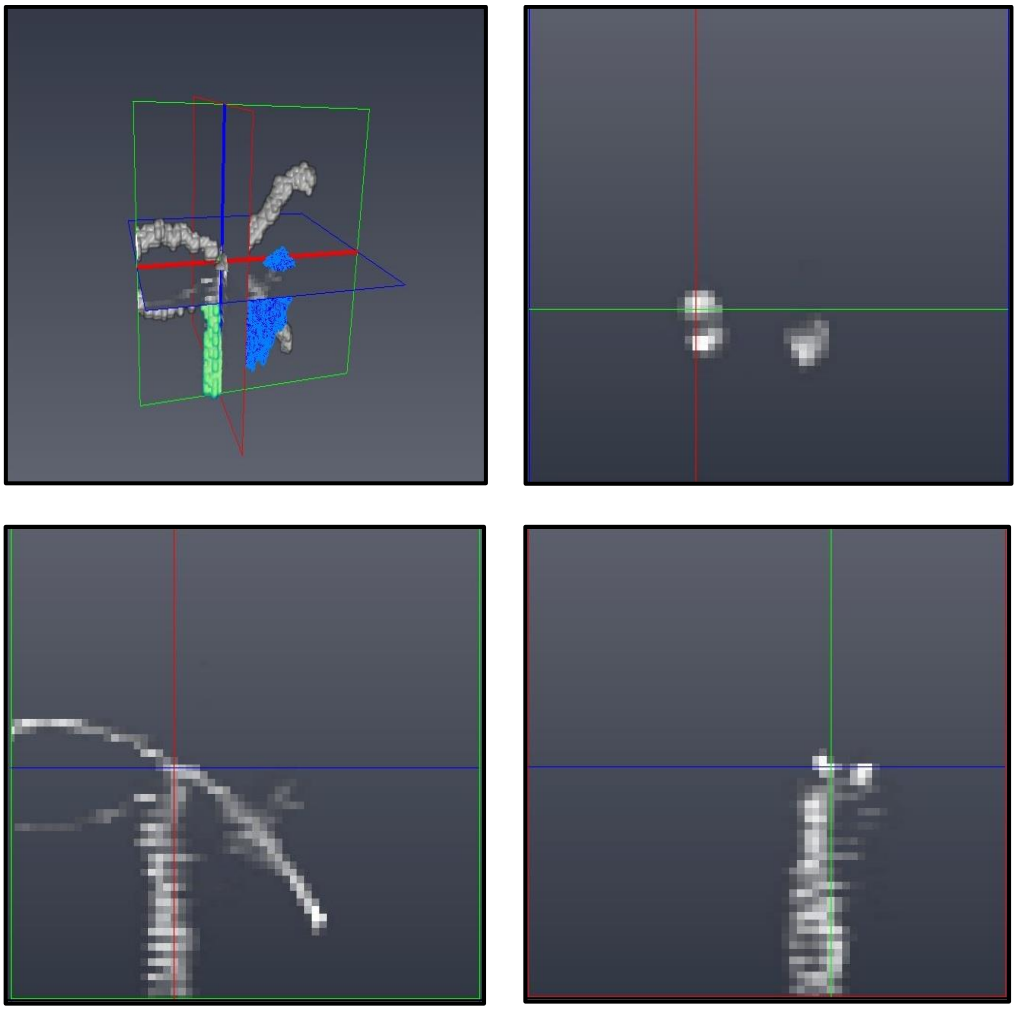

Figure 4.38. Top left: 3D reconstruction of the sample. Top right: example of coronal slice. Bottom left: example of sagittal slice. Bottom right: example of frontal slice. This Figure represents the typical way a CT scan would be presented.

4.5.5. Summary and conclusions

In the second part of this Chapter we have successfully tested the feasibility of using the betatron X-rays produced by the ALPHA-X LWFA for microscopy and micro-tomographic imaging. The results are encouraging and represent a good starting point for future imaging application developments.

The XPCi results obtained in the first experiment using Timepix and imaging plates (section 4.4) have been expanded in this second experiment. Here we have obtained XPCi of wires as thin as 10 μm of exceptional quality. This proof of principle experiment shows the potential of the betatron X-rays for microscopy imaging.

An interesting next step would be to increase the magnification of the LWFA X-ray microscope. This can be achieved by placing the sample closer to the plasma accelerator. By increasing the magnification, smaller features in the samples can be distinguished. Although challenging, it would be interesting, for instance, to explore the possibility of imaging the internal structure of a hair strand using a LWFA X-ray microscope. This is normally done using electron microscopes. For this, the sample has to be in vacuum, which is a limitation of this type of microscopes. Also, samples are normally dehydrated therefore distorting both sample and image.

Very recently, tomography of biological samples using the betatron X-rays have been reported [47, 48]. However, here we present the smallest sample ever imaged by tomography using betatron X-rays from a LWFA, to the best of this author's knowledge, demonstrating the applicability of the betatron X-rays for micro-tomography imaging.

Summarising the micro-tomography experiment, several projections of the sample have been taken proving that with a sufficient number of projections micro-tomographic reconstruction is possible. In this experiment, each projection is recorded using 500 laser shots. The total number of projections recorded is 41.

The number of projections recorded was not higher due to experimental time limitations. However, despite the low number of projections, both the micro-tomography and the 3D reconstruction have been successful accomplished and all the components of the sample are clearly visible. The obvious way to improve the quality of the results would be to take more projections. Ideally, at least 1 projection per degree would be necessary for high quality tomographic reconstruction.

An improvement in the stability of LWFA electron beams, with a corresponding improvement in the stability of the betatron X-rays, would also be desirable. Some studies [52, 53] have shown enhanced stability of electron beams when gas-filled dielectric capillary tubes or gas cells are used instead of a gas jet.

Dielectric capillary tubes or gas cells of similar dimensions provide a more stable and repeatable gas density distribution. Also, the fact that this gas distribution is shock-free increases the stability of LWFA generated electron beams.

Another parameter where there is scope for improvement is increasing the repetition rate of the high power laser system. The betatron X-ray source is pulsed and therefore the exposure time is very small for each projection. This means that the main limitation in the scanning time and the number of projections that can be measured is just limited by the repetition rate of the laser.

The development of high power laser systems operating at high repetition rates of the order of 1 kHz is indeed challenging. Issues regarding higher gas loading on the vacuum system or the potential cumulative laser damage on the compressor grating do not have a straight forward solution. Moreover, cumulative laser damage to the dielectric capillary tube or the gas cell would occur if these plasma accelerators are used.

However, if these challenges are overcome, these high repetition rate systems may allow construction of laboratory-scale high brightness X-ray sources, which would be very useful to a wide variety of imaging applications.

Chapter references:

1. Shah, R.C., et al., *Coherence-based transverse measurement of synchrotron x-ray radiation from relativistic laser-plasma interaction and laser-accelerated electrons.* Physical Review E, 2006. **74**(4): p. 045401.
2. Rousse, A., et al., *Production of a keV X-Ray Beam from Synchrotron Radiation in Relativistic Laser-Plasma Interaction.* Physical Review Letters, 2004. **93**(13): p. 135005.
3. Kneip, S., et al., *Bright spatially coherent synchrotron X-rays from a table-top source.* Nature Physics, 2010. **6**(12): p. 980-983.

4. Cipiccia, S., et al., *Gamma-rays from harmonically resonant betatron oscillations in a plasma wake.* Nature Physics, 2011. **7**(11): p. 867-871.
5. Kneip, S., et al., *X-ray phase contrast imaging of biological specimens with femtosecond pulses of betatron radiation from a compact laser plasma wakefield accelerator.* Applied Physics Letters, 2011. **99**(9): p. 093701.
6. Fourmaux, S., et al., *Single shot phase contrast imaging using laser-produced Betatron x-ray beams.* Optics Letters, 2011. **36**(13): p. 2426-2428.
7. Zernike, F., *Phase contrast, a new method for the microscopic observation of transparent objects.* Physica, 1942. **9**(7): p. 686-698.
8. Zernike, F., *How I Discovered Phase Contrast.* Science, 1955. **121**(3141): p. 345-349.
9. Bonse, U. and M. Hart, *An X-Ray Interferometer.* Applied Physics Letters, 1965. **6**(8): p. 155-156.
10. Momose, A. and J. Fukuda, *Phase-contrast radiographs of nonstained rat cerebellar specimen.* Medical Physics, 1995. **22**(4): p. 375-379.
11. Momose, A., et al., *Phase-contrast X-ray computed tomography for observing biological soft tissues.* Nat Med, 1996. **2**(4): p. 473-475.
12. Talbot, H.F., *LXXVI. Facts relating to optical science. No. IV.* The London and Edinburgh Philosophical Magazine and Journal of Science, 1836. **9**(56): p. 401-407.
13. Wilkins, S.W., et al., *Phase-contrast imaging using polychromatic hard X-rays.* Nature, 1996. **384**(6607): p. 335-338.
14. Bonse, U. and M. Hart, *Small angle X-ray scattering by spherical particles of Polystyrene and Polyvinyltoluene.* Zeitschrift für Physik, 1966. **189**(2): p. 151-162.
15. Hirai, T., et al., *Refraction contrast 11×-magnified X-ray imaging of large objects by MIRRORCLE-type table-top synchrotron.* Journal of Synchrotron Radiation, 2006. **13**(5): p. 397-402.

16. van Heekeren, J., et al., *Characterization of an x-ray phase contrast imaging system based on the miniature synchrotron MIRRORCLE-6X.* Medical Physics, 2011. **38**(9): p. 5136-5145.
17. Bech, M., et al., *Hard X-ray phase-contrast imaging with the Compact Light Source based on inverse Compton X-rays.* Journal of synchrotron radiation, 2009. **16**(1): p. 43-47.
18. Yamada, K., et al., *A trial for fine and low-dose imaging of biological specimens using quasi-monochromatic laser-Compton X-rays.* Nuclear Instruments and Methods in Physics Research Section A: Accelerators, Spectrometers, Detectors and Associated Equipment, 2009. **608**(1, Supplement): p. S7-S10.
19. Olivo, A. and R. Speller, *A coded-aperture technique allowing x-ray phase contrast imaging with conventional sources.* Applied Physics Letters, 2007. **91**(7): p. 074106.
20. Olivo, A. and E. Castelli, *X-ray phase contrast imaging: From synchrotrons to conventional sources.* Rivista Del Nuovo Cimento, 2014. **37**(9): p. 467-508.
21. Weitkamp, T., et al., *X-ray phase imaging with a grating interferometer.* Optics Express, 2005. **13**(16): p. 6296-6304.
22. Pfeiffer, F., et al., *Phase retrieval and differential phase-contrast imaging with low-brilliance X-ray sources.* Nature physics, 2006. **2**(4): p. 258-261.
23. Snigirev, A., et al., *On the possibilities of x-ray phase contrast microimaging by coherent high-energy synchrotron radiation.* Review of scientific instruments, 1995. **66**(12): p. 5486-5492.
24. *Born M. and Wolf E., Principles of Optics, 6th Edition. (Pergamon Press, 1959, Oxford, UK).*
25. Jakůbek, J., *Semiconductor Pixel detectors and their applications in life sciences.* Journal of Instrumentation, 2009. **4**(03): p. P03013.
26. Llopart, X., et al., *Timepix, a 65k programmable pixel readout chip for arrival time, energy and/or photon counting measurements.* Nuclear Instruments and Methods in Physics Research Section A: Accelerators,

Spectrometers, Detectors and Associated Equipment, 2007. **581**(1–2): p. 485-494.

27. Delpierre, P., et al., *XPAD: A photons counting pixel detector for material sciences and small-animal imaging.* Nuclear Instruments and Methods in Physics Research Section A: Accelerators, Spectrometers, Detectors and Associated Equipment, 2007. **572**(1): p. 250-253.
28. Llopart, X., et al., *Medipix2: a 64-k pixel readout chip with 55-μm square elements working in single photon counting mode.* IEEE Transactions on Nuclear Science, 2002. **49**(5): p. 2279-2283.
29. Shanks, R., *Comprehensive characterisation of laser plasma wakefield accelerated electrons.* Ph.D. thesis, University of Strathclyde, 2012.
30. http://aladdin.utef.cvut.cz/ofat/Others/Pixelman/Pixelman.html
31. *www.nist.gov/pml/atomic-spectra-database*
32. Savitzky, A. and M.J. Golay, *Smoothing and differentiation of data by simplified least squares procedures.* Analytical chemistry, 1964. **36**(8): p. 1627-1639.
33. Schnell, M., et al., *Optical control of hard X-ray polarization by electron injection in a laser wakefield accelerator.* Nature Communications, 2013. **4**.
34. Fraser, G., *X-ray Detectors in Astronomy.* Cambridge and New York, Cambridge University Press, 1989, 312 p., 1989. **1**.
35. Tsunemi, H., et al., *Detection of X-ray polarization with a charge coupled device.* Nuclear Instruments and Methods in Physics Research Section A: Accelerators, Spectrometers, Detectors and Associated Equipment, 1992. **321**(3): p. 629-631.
36. Tsunemi, H., et al. *Application of a charge-coupled device as an x-ray polarimeter*. in *SPIE's 1993 International Symposium on Optics, Imaging, and Instrumentation*. 1994. International Society for Optics and Photonics.
37. Bögner, M., et al., *X-ray polarimetry—A novel application of CCDs.* Nuclear Instruments and Methods in Physics Research Section A:

Accelerators, Spectrometers, Detectors and Associated Equipment, 1996. **377**(2): p. 529-531.

38. Gehrels, T., *Planets, stars and nebulae: studied with photopolarimetry*. 1974. **23**. University of Arizona Press.
39. Everhart, T. and P. Hoff, *Determination of kilovolt electron energy dissipation vs penetration distance in solid materials.* Journal of Applied Physics, 1971. **42**(13): p. 5837-5846.
40. Reboredo, D., et al. *Phase-contrast imaging using radiation sources based on laser-plasma wakefield accelerators: state of the art and future development*. in *SPIE Medical Imaging*. 2015. International Society for Optics and Photonics.
41. Schnell, M., et al., *Characterization and application of hard x-ray betatron radiation generated by relativistic electrons from a laser-wakefield accelerator.* Journal of Plasma Physics, 2015. **81**(04): p. 475810401.
42. Hecht, E., *Hecht optics.* Addison Wesley, 1998. **997**: p. 213-214.
43. Ferrari, A., et al., *FLUKA: A multi-particle transport code (Program version 2005)*. 2005.
44. Cipiccia, S., et al., *Inclusion of coherence in Monte Carlo models for simulation of x-ray phase contrast imaging.* Optics Express, 2014. **22**(19): p. 23480-23488.
45. Schneider, C.A., W.S. Rasband, and K.W. Eliceiri, *NIH Image to ImageJ: 25 years of image analysis.* Nat Meth, 2012. **9**(7): p. 671-675.
46. *S. W. Smith, The Scientist and Engineer's Guide to Digital Signal Processing, California Technical Publishing.*
47. Cole, J., et al., *Tomography of human trabecular bone with a laser-wakefield driven x-ray source.* Plasma Physics and Controlled Fusion, 2015. **58**(1): p. 014008.
48. Wenz, J., et al., *Quantitative X-ray phase-contrast microtomography from a compact laser-driven betatron source.* Nature Communications, 2015. **6**.

49. Gürsoy, D., et al., *TomoPy: a framework for the analysis of synchrotron tomographic data.* Journal of Synchrotron Radiation, 2014. **21**(Pt 5): p. 1188-1193.
50. www.fei.com/software/amira-avizo/
51. Van Daatselaar, A., P. Van der Stelt, and J. Weenen, *Effect of number of projections on image quality of local CT.* Dentomaxillofacial Radiology, 2014.
52. Hansson, M., et al., *Enhanced stability of laser wakefield acceleration using dielectric capillary tubes.* Physical Review Special Topics - Accelerators and Beams, 2014. **17**(3): p. 031303.
53. Vargas, M., et al., *Improvements to laser wakefield accelerated electron beam stability, divergence, and energy spread using three-dimensional printed two-stage gas cell targets.* Applied Physics Letters, 2014. **104**(17): p. 174103.

Chapter 5: Imaging with laser-driven bremsstrahlung radiation

5.1 Introduction to laser-driven bremsstrahlung imaging

Gamma-ray sources produced via bremsstrahlung are commonly used in medical, industrial and scientific research applications. Bremsstrahlung or “braking radiation” is produced by the deceleration of a charged particle, typically an electron, slowing down in matter. Bremsstrahlung radiation is currently used for single-shot measurements or applications that require high flux, high energy and very small source size.

Bremsstrahlung radiation is currently produced using conventional particle accelerators where high-energy electron beams are converted into gamma-ray beams as they slow down in a dense target, such as tungsten, tantalum or lead. A good example of this is a medical LINAC, where electrons are accelerated to an energy of around 10 MeV and focused onto a dense target to produce a medical X-ray beam for the treatment of cancer.

High energy electron beams from laser-plasma accelerators have been already used to produce high flux and small size [1-4] bremsstrahlung X-ray sources. Radiographic images using laser-driven bremsstrahlung sources have also already been produced [5, 6].

The advantage of this type of acceleration concept is the ability to produce electron beams with an energy of around 150 MeV in mm distances. This leads to very high energy X-ray bremsstrahlung beams, which reduces the costs by using a compact table-top technology. Higher energies and doses are used in non-destructive inspection of industrial material. Moreover, an energy of 15-30 MeV is required to transmute nuclear waste or produce radionuclides [7].

In this Chapter, we investigate the use of the ALPHA-X bremsstrahlung X-ray source for imaging applications. Specifically, we explore the possibility of producing tomographic images, which may find uses in industrial applications.

The first part of this chapter presents a brief overview of the physics of the bremsstrahlung process. The second section describes the experimental set-up used for the characterisation of the electron beam produced in the ALPHA-X beamline. The third part presents Monte Carlo simulations for characterising the bremsstrahlung X-ray source. The following section shows tomographic results obtained and describes the analysis of the images obtained. Finally, conclusions and a summary are presented in the last section.

5.2 Bremsstrahlung radiation production mechanism

It is well known that charged particles emit electromagnetic radiation when they are accelerated or decelerated. Particles passing through matter are scattered and lose energy by collisions. This causes the particles to deaccelerate and emit electromagnetic radiation. Typically, bremsstrahlung is produced by electrons colliding with atomic nuclei.

A derivation of the bremsstrahlung properties, *i.e.* total radiation emitted, angular distribution and frequency spectrum, can be found in “Classical electrodynamics” by J. D. Jackson [8].

The radiation emitted in a bremsstrahlung process can be calculated using the Liénard-Wiechert potentials, obtaining the following angular distribution of the radiated power:

$$\frac{dP(t')}{d\,\Omega} = \frac{e^2}{4\pi c}\frac{\left|\bar{n}\times\left\{\left(\bar{n}-\bar{\beta}\right)\times\dot{\bar{\beta}}\right\}\right|^2}{\left(1-\bar{n}\cdot\bar{\beta}\right)^5}, \tag{5.1}$$

where $\beta = v/c$ is the particle velocity normalised to the speed of light. The total instantaneous radiated power can be obtained by integrating equation 5.1 over all solid angles. In the bremsstrahlung case $\beta \parallel \dot{\beta}$, thus:

$$P = \frac{2e^2}{3M^2c^3}\left(\frac{dp}{dt}\right)^2, \tag{5.2}$$

where M is the particles mass and p the momentum. This is a generalisation of the Larmor formula [8].

The rate of change in momentum is equal to the change in energy of the particle per unit distance. Therefore,

$$P = \frac{2e^2}{3M^2c^3}\left(\frac{dE}{dx}\right)^2, \tag{5.3}$$

where the term dE/dx is the energy lost by the particle per unit of path length.

In the nonrelativistic limit the total energy radiated by a particle of mass M going through a unit of thickness matter that contains N fixed charges Ze per unit volume is [8]:

$$\frac{dE_{rad}}{dx} = \frac{16}{3}NZ\left(\frac{Ze^2}{hc}\right)\frac{z^4e^4}{Mc^2}, \tag{5.4}$$

where Z is the atomic number. It is interesting to compare the energy loss by emitted radiation and the energy loss due to collisions [8]:

$$\frac{dE_{rad}}{dE_{coll}} = \frac{4z^2}{3\pi}\frac{Z}{137}\frac{m}{M}\left(\frac{v}{c}\right)^2\frac{1}{lnB_q}, \tag{5.5}$$

where *m* is the electron mass. The factor m/M appears because the radiative loss involves acceleration of the incident particle and the energy loss by collisions involves the acceleration of an electron. B_q is given by:

$$B_q = \frac{2\gamma^2\beta^2mc^2}{h\langle w\rangle}, \tag{5.6}$$

where w is the mean excitation energy [8].

Looking at equation 5.5 it is clear that for non-relativistic particles, *i.e.* $v \ll c$, the radiative energy losses are almost negligible compared with energy collision losses.

The screening effect of the electronic atoms has to be taken into account in the relativistic case. At higher energy, where complete screening occurs, the energy loss by radiation is [8]:

$$\frac{dE_{rad}}{dx} \cong \left[\frac{16}{3} N \left(\frac{Z^2 e^2}{hc}\right) \frac{z^4 e^4}{M^2 c^2} ln\left(\frac{233M}{Z^{1/3} m}\right)\right] \gamma M c^2. \quad (5.7)$$

Equation 5.7 shows that eventually the radiative losses become proportional to the particles energy. In this case, the ratio between radiation losses and collision losses is [8]:

$$\frac{dE_{rad}}{dE_{coll}} \cong \frac{4z^2}{3\pi} \frac{Z}{137} \frac{m}{M} \frac{ln\left(\frac{233M}{Z^{1/3} m}\right)}{ln(B_q)} \gamma. \quad (5.8)$$

As the energy increases the radiative losses become more important than the collision losses and for ultra-relativistic particles this is the dominant energy loss mechanism. It is important to note that at relativistic particle energies the photons are emitted in a narrow opening angle of $1/\gamma$.

It is useful to define a radiation length X_0 which is the distance travelled by a particle before its energy falls to $1/e$ of its initial value [8]:

$$X_o = \left[4N \frac{Z(Z+1)e^2}{hc} ln\left(\frac{233M}{Z^{1/3} m}\right) \left(\frac{z^2 e^2}{Mc^2}\right)^2\right]^{-1}. \quad (5.9)$$

This quantity is often expressed in g/cm^2. For electrons, some representative values are shown in the following table [9]:

Table 5.1. Radiation length values for representative materials used in research environment.

	Al	***Cu***	***W***	***Pb***
X₀ (g/cm²)	*24.0*	*12.9*	*5.8*	*5.8*

In order to use bremsstrahlung in real world applications it is important to know the spectrum of the radiation emitted. Many studies have been performed on this topic. For electrons, Koch and Motz [10] published a summary of the bremsstrahlung cross-section formulas and related data. Particularly interesting are the dependences of the bremsstrahlung spectrum on the electron energy and the photon angle.

Dr Silvia Cipiccia explored in her PhD thesis [11] the dependence of the bremsstrahlung spectrum on the source size, divergence and conversion

efficiency (defined as the ratio between bremsstrahlung photons produced and the total incoming electron flux) using the Monte Carlo code Geant4 [12]. Those parameters allow the tuning of the properties of the radiation emitted during the bremsstrahlung process. The properties required for the radiation emitted will depend on each application: some applications may require short exposures times and others may require a high gamma-ray flux for instance. LWFA technology allows the tunability of the incoming electron beam and therefore the tunability of the photons emitted via the bremsstrahlung process. A summary of the numerical results found by Dr Silvia Cipiccia are shown in the table 5.2 from [11].

Table 5.2. Summary of the effects of increasing the parameters listed in the first column on the Bremsstrahlung radiation properties given in the heading. Symbols ">" means increasing, "<" decreasing and "–" no change.

	Conversion efficiency (%)	**Source size**	**Gamma divergence**	**Pulse duration**
electron energy	-	-	<	-
electron divergence	-	>	-	-
Z material	>	-	>	No trend
Target thickness	>	-	>	>
Source-target distance	-	>	-	-

Ben-Ismail *et al.* [13] did a similar study using the same Monte Carlo code (GEANT4) and comparable electron beam parameters, applicable to LWFAs. The results of both studies show good agreement.

5.3 Experimental setup

An experiment to demonstrate the suitability of laser-driven bremsstrahlung radiation for imaging applications has been performed on the ALPHA-X beam line at the University of Strathclyde. The main objective of this experiment is to perform a tomographic scan using laser-driven bremsstrahlung radiation. To

the best knowledge of the author, this is the first LWFA driven bremsstrahlung tomographic scan.

The object imaged is a hexagonal prism made of lead placed in a small sand container. Radioactive waste is commonly stored inside cement or concrete barrels filled with sand. This configuration aims to reproduce the storage environment of radioactive waste to explore the possible application of the gamma-ray source for radioactive waste monitoring and assay purposes.

The experiment has been performed after the upgrade of the TOPS laser system (see Chapter 3 for details). The first objective of this experiment is to optimise and measure the energy spectrum and the charge of the electron beam produced. For this, an ultra-intense laser pulse of 1 J energy on target, 800 nm wavelength, 35-40 fs pulse duration and 40 μm spot size is focused at the entrance of a 3 mm long supersonic gas jet. More details on the laser system and the gas jet-nozzle system used in the experiment can be found in Chapter 3 of the PhD thesis.

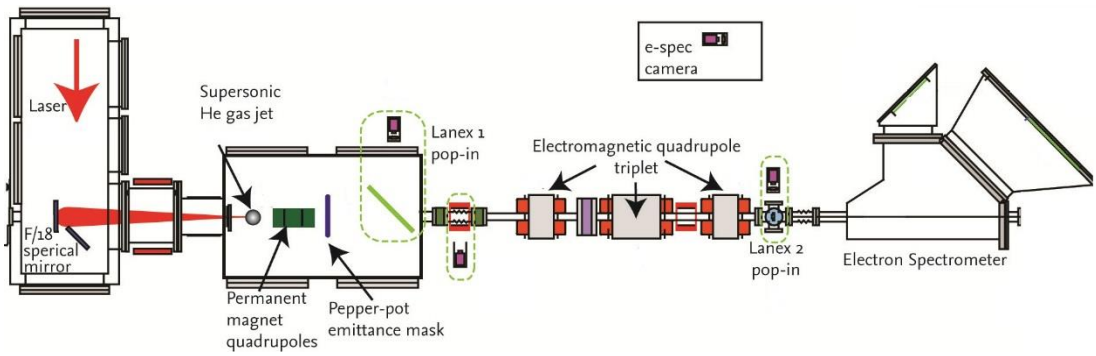

Figure 5.1. Schematic of the experimental setup of the first part of the laser-driven bremsstrahlung imaging experiment.

After focusing the laser system onto the target, the electron beam is optimised by imaging Lanex 1. To do this, the gas jet-nozzle is moved with micrometre precision until a stable electron beam is observed. The optimum height is found to be 4.5 mm for a backing pressure of 35 bar, which corresponds to a plasma density of $1.3\times10^{19}\ \mathrm{cm}^{-3}$ according to FLUENT simulations (see Chapter 3 for more information). A set of permanent quadrupoles (PMQs) are placed in the interaction chamber to optimise the transport of the electron beam. They

reduce the divergence of the electron beam, improve the pointing stability and filter out the low energy component of the electron bunch produced.

Once the gas jet position for the most stable electron beam is found, Lanex 1 is removed and the electron beam propagates through the ALPHA-X beamline. The electron energy spectrum is then measured (see Figures 5.2 and 5.3) using the electron spectrometer described in Chapter 3 of this thesis.

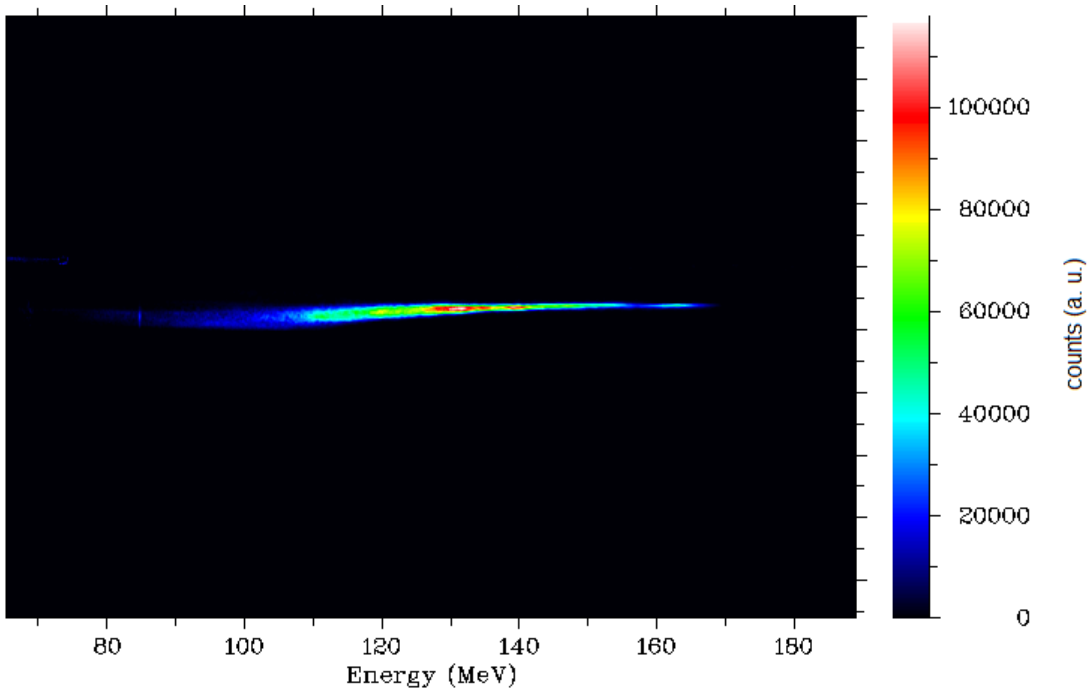

Figure 5.2. False colour image showing accumulated 500 shots of electron spectra recorded using the electron spectrometer during the experiment.

The electron beam energy measured during this part of the experiment is 119.3 ± 18.6 MeV (rms) averaged over 500 laser shots (see Figure 5.3). The beam transport is optimised using the electromagnetic quadrupole triplet described in Chapter 3 of the thesis. Simulations using MAD-X [14] have been performed by Dr Enrico Brunetti to optimise the electron beam transport. MAD scripting language is the standard to describe particle accelerators, simulate beam dynamics and optimise beam optics.

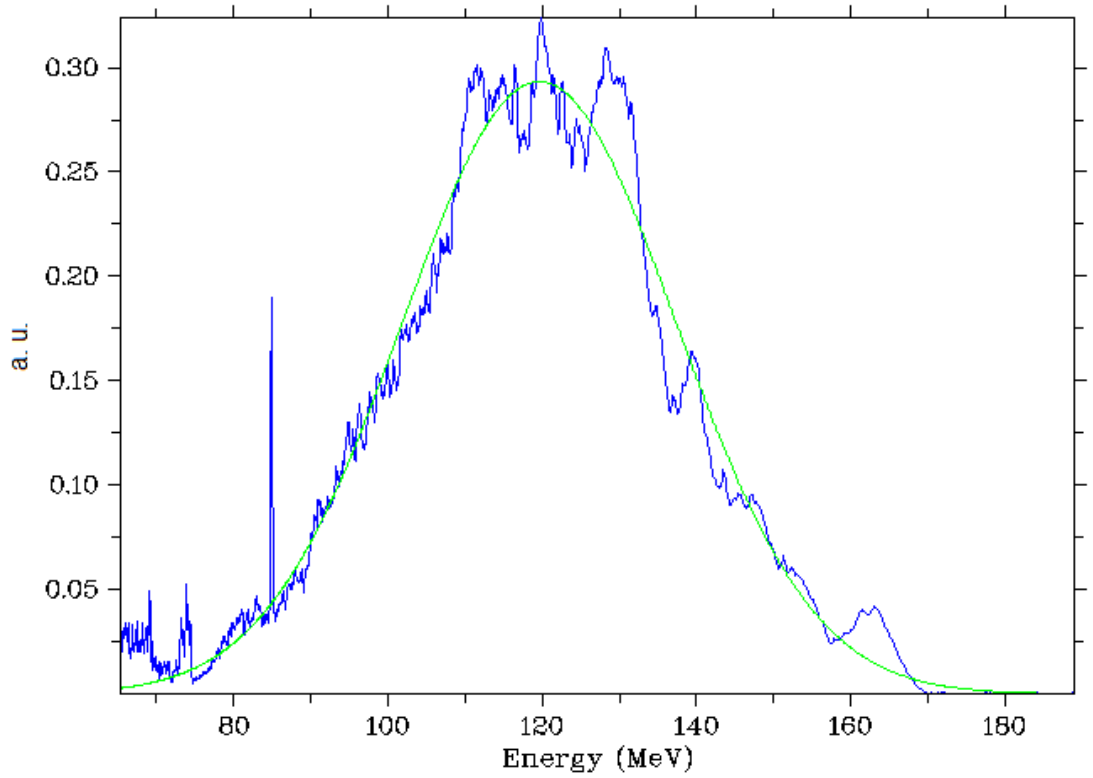

Figure 5.3. Accumulated averaged electron energy spectra over 500 shots. The energy measured is 119.3 ± 18.6 MeV (rms).

The beam line, including PMQs and EMQs (see Chapter 3 for details), was modelled with MAD-X and the currents of the three electrodynamic quadrupoles were varied between 0 and 20 A, trying to obtain an electron beam spot size (sigma) of about 0.6 mm after 2.5 m propagation for an energy of 130 MeV.

A matching problem consists of a set of equations $\vec{c} = \vec{f}(\vec{v})$, where $\vec{c}$ is a vector of constraints, $\vec{v}$ a vector of variables and $\vec{f}$ a vector field describing the beam line components. Here the variables are the quadrupole currents and the constraints are a spot size smaller than 1 mm going through the EMQs and a final spot size of about 0.6 mm. The optimum currents are found with an iterative algorithm that minimises the sum of squares of the constraint equations using their numerical derivatives. The optimum currents are found to be 9.7 A, 8.1 A and 18.0 A respectively.

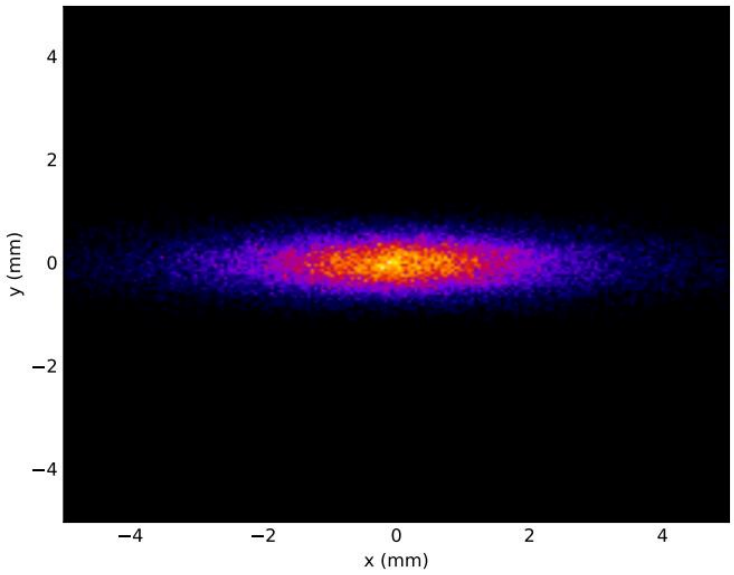

Figure 5.4. Geant4 simulated electron beam spot profile for an electron energy of 130 MeV, 2 mrad rms divergence after going through a set of quadrupoles with currents of 9.7 A, 8.1 A and 18.0 A (courtesy of Dr Enrico Brunetti).

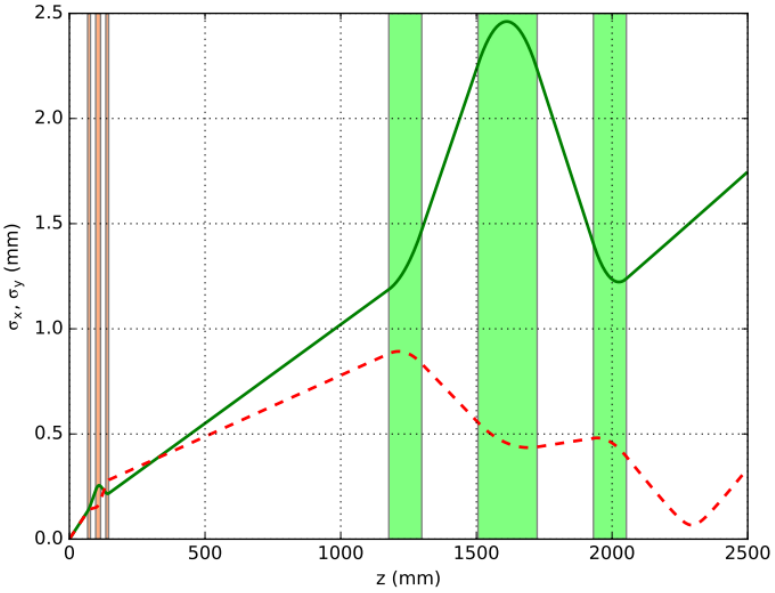

Figure 5.5. Geant4 simulated electron beam envelope for an electron energy of 130 MeV, 2 mrad rms divergence after going through a set of quadrupoles with currents of 9.7 A, 8.1 A and 18.0 A. The green line represents σ_x and the red dotted line σ_y (courtesy of Dr Enrico Brunetti).

To evaluate the performance of this beam line configuration for an electron beam with a large energy spread, additional simulations have been undertaken using Geant4. The electron beam spot profile and envelope obtained for a 130 MeV electron beam with 5% energy spread, 2 mrad rms divergence and currents of 9.7 A, 8.1 A and 18.0 A are shown in Figures 5.4 and 5.5

respectively. It can be seen that the focusing works well only for one axis and that the spot is elliptical. This is unavoidable because the spot position is very close to the last quadrupole (just after Lanex 2).

The electron bunch charge per laser shot is measured just after Lanex 2. This is also where the converter is placed in the next step of the experiment. Therefore, measuring the electron beam charge at this point gives a good estimate of the total electron beam charge in the converter, which is typically smaller than the charge produced by the laser-plasma accelerator since some electrons are lost during propagation through the beam line. In particular, the PMQs are optimised for an energy of 130 MeV and deflect away the low-energy component of the electron beam.

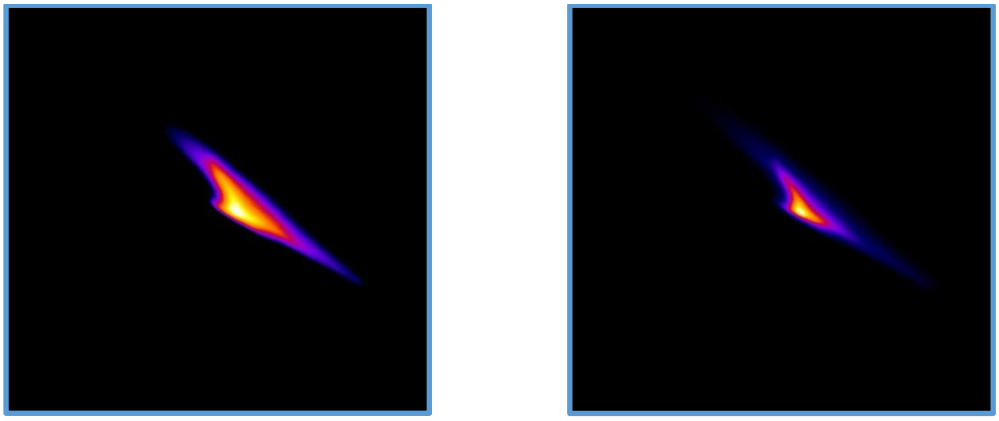

Figure 5.6. Left: false colour logarithmic scale of one of the irradiated imaging plates during the experiment. Right: false colour electron charge image after performing the corresponding analysis explained in Chapter 3 of this thesis.

Measurements of the beam charge are made using imaging plates (IP). The procedure for analysing the imaging plates is described in Chapter 3. In brief, after an IP is irradiated it is scanned and then converted from a logarithmic greyscale to physical units using equation 3.6. After this, the PSL number is corrected by the fading effect and available parameters.

Each IP is irradiated with 10 shots and a total number of 5 measurements are taken, corresponding to 50 laser shots in total. The measured charge varies significantly, with average values ranging between 1.5 and 5 pC per laser shot. This is due to instabilities in the laser gas jet system, which is expected from a

LWFA. An average of the 5 measurements (50 laser shots) provides a charge of 2.3 ± 1.1 pC per laser shot (Figure 5.6).

After completing the characterisation of the electron beam, the bremsstrahlung imaging experiment is started. The experimental setup is shown in Figure 5.7. To keep the same electron beam parameters as in the first part of the experiment, the nozzle height is set again to 4.5 mm and the backing pressure to 35 bar. No adjustments are made to the laser system between experiments, apart from routine alignment. As in the first part of the experiment, the electron beam is first optimised by looking at Lanex 1. Once a stable electron beam is achieved, this Lanex screen is withdrawn and the beam propagates through the beamline.

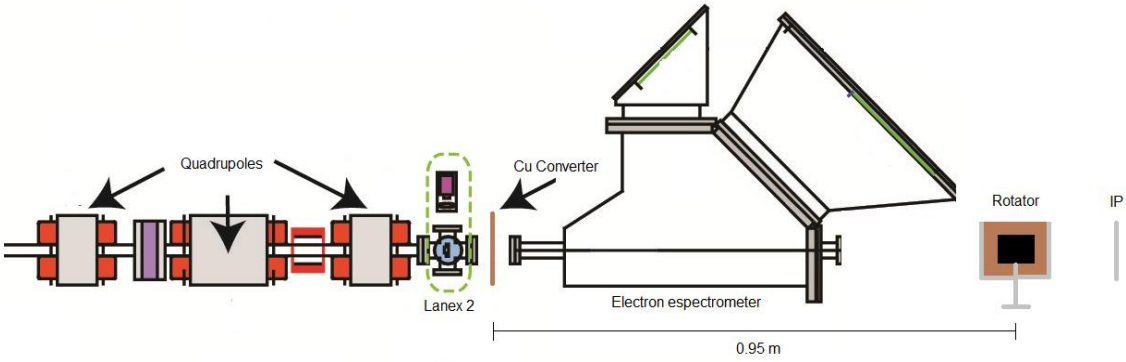

Figure 5.7. Schematic of the experimental setup of the second part of the bremsstrahlung imaging experiment. The experimental setup before the quadrupoles is similar to the one in Figure 5.1.

The electron beam is then converted to bremsstrahlung radiation in a 1 mm thick copper target placed just before the electron spectrometer. To reduce the level of parasitic radiation produced by the interaction of the electron beam with the object to radiograph, the electron spectrometer is switched on for the whole experimental run. This prevents secondary electrons produced in the converter from propagating downstream towards the experiment.

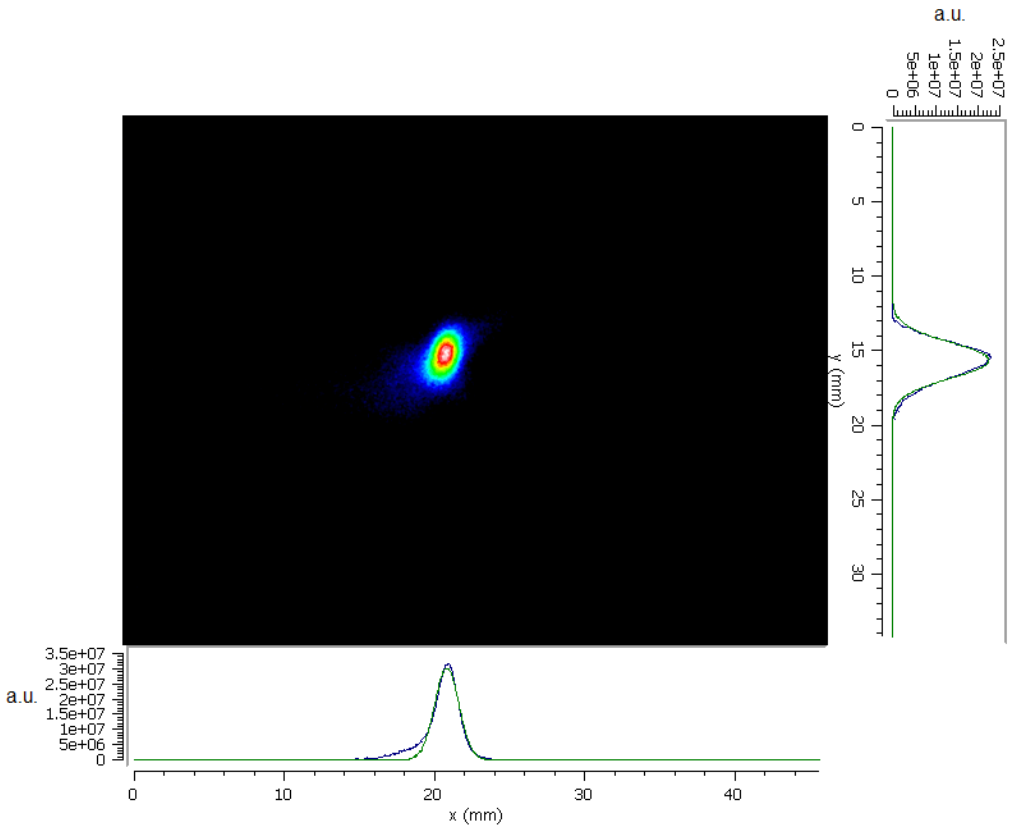

Figure 5.8. Example of lanex 2 shot. This lanex screen is placed just before the Cu converter. Two Gaussian fits have been performed for each axis. The electron beam spot size (sigma) for this specific shot was 1.3 mm in the x axis and 1.2 mm in the y axis.

The converter is placed just after lanex 2 (see Figure 5.7), which is used to monitor the electron beam to ensure, firstly, that it is stable and secondly that it impinges on the Cu converter during the whole experimental run. Lanex 2 screen is then withdrawn and each projection recorded. It is inserted typically every 5 projections to check that the electron beam quality is still good. A sample shot on Lanex 2 is shown in Figure 5.8 and an accumulated image for 200 consecutive shots is shown in Figure 5.9.

Averaging over 200 shots the spot size (sigma) in the x axis is 3.8 mm and in the y axis 1.2 mm. These parameters, together with the measured energy and charge, have been used as parameters for Monte Carlo simulations to estimate the X-ray spectrum of the bremsstrahlung radiation produced.

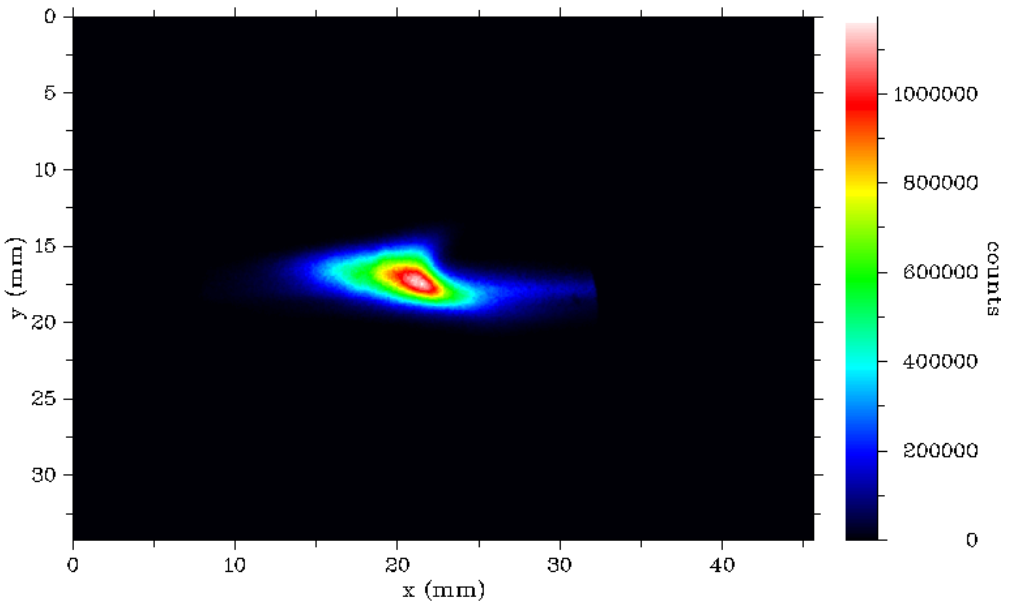

Figure 5.9. Accumulated image for 200 shots in lanex 2. The average electron beam spot size (sigma) is 3.8 mm in the x axis and 1.2 mm in the y axis.

The object to be imaged, a lead hexagonal prism of 5 cm height and 2 cm thickness, is placed in a 6 cm diameter sand container. This arrangement attempts to replicate a container filled with sand and radioactive material. The container is placed on a rotator with 1º accuracy. A spirit level is used to ensure the rotational stage is set flat and normal to the beam. The distance between the Cu converter and the rotator is 0.95 m and the distance between the rotator and the detector is 10 cm.

Each projection is recorded using an image plate (Fujifilm BAS-SR model), which has a maximum resolution (set by the scanner, *i.e.* Fujifilm FLA700 reader) of 50 μm [15]. More details can be found in Chapter 3.

All projections are recorded on the same imaging plate, which is scanned and then erased each time after irradiation. To ensure that the imaging plate is placed in the same position in the beam line for each projection, a suitable holder has been designed for the imaging plate to ensure reproducibility of the positioning the imaging plate.

A total number of 72 projections have been recorded. Each projection has been recorded with 200 laser shots.

5.4 Monte Carlo simulations for the characterisation of the ALPHA-X bremsstrahlung X-ray beam

Monte Carlo simulations using FLUKA [16, 17] and Flair [18] have been undertaken to estimate the spectrum and spatial distribution of the bremsstrahlung X-ray beam produced during the experimental run. To ensure that the simulation is as accurate as possible, the parameters corresponding to these measured during the experimental run have been used. The electron beam energy used is 119.3 ± 18.6 MeV (obtained experimentally from an average over 500 shots). The spot size of the electron beam (sigma) is 3.8 mm in the x axis and 1.2 mm in the y axis. The resulting distribution and X-ray spectrum are normalised to the average number of electrons per laser shot *i.e.* 2.3 pC or 1.4×10^{7} electrons.

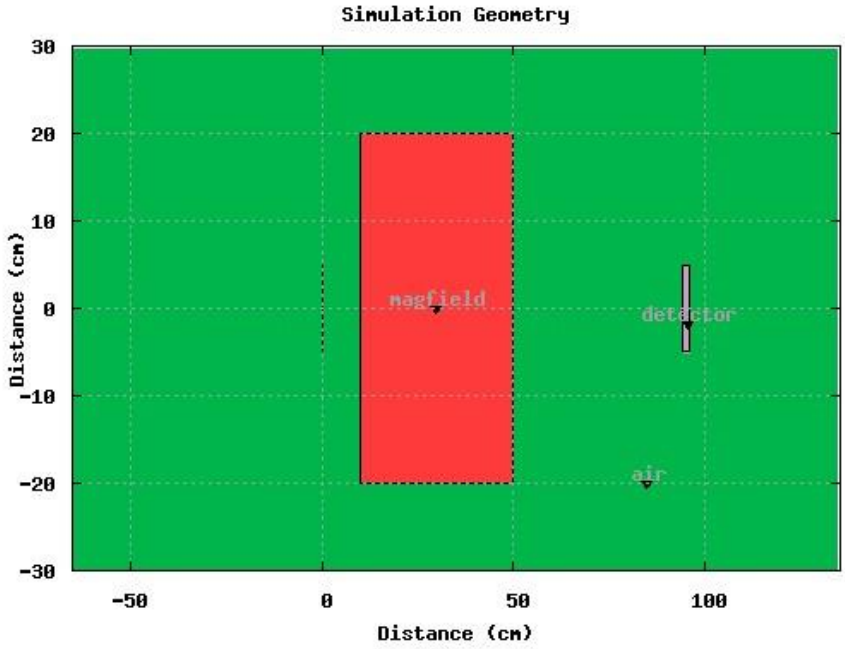

Figure 5.10. Top view of the geometry of the Monte Carlo simulation. The main three regions of the simulation can be seen in the Figure: the copper converter on the left, the magnetic field on the centre and the detector on the right. The green area is air.

The geometry of the simulation is shown in Figure 5.10. It comprises three regions. One region corresponds to the copper converter. The second one

corresponds to the region where the magnetic field bends the electrons away (emulating the electron spectrometer in the second part of the experiment) and the last region including a detector on the beam line axis, which is where the X-ray spatial distribution and spectrum are scored. All elements are placed in air.

Any result in a FLUKA simulation is obtained by adding the contributions to the "score" of a detector defined by the user, which represents the behaviour of a measurement instrument. Each detector type is designed to estimate different quantities and the final score is a statistical estimate of the average value of the corresponding population.

The statistical standard deviation is obtained by running several independent calculations (or "cycles" in FLUKA) in the same way as several experimental runs are performed to obtain the experimental mean value of a certain quantity. FLUKA therefore relies on the Central Limit Theorem to calculate the mean value of a scored quantity and for determining the error of the mean. The theorem states: "the distribution of an average tends to be Normal even when the distribution from which the average is computed is decidedly non-Normal".

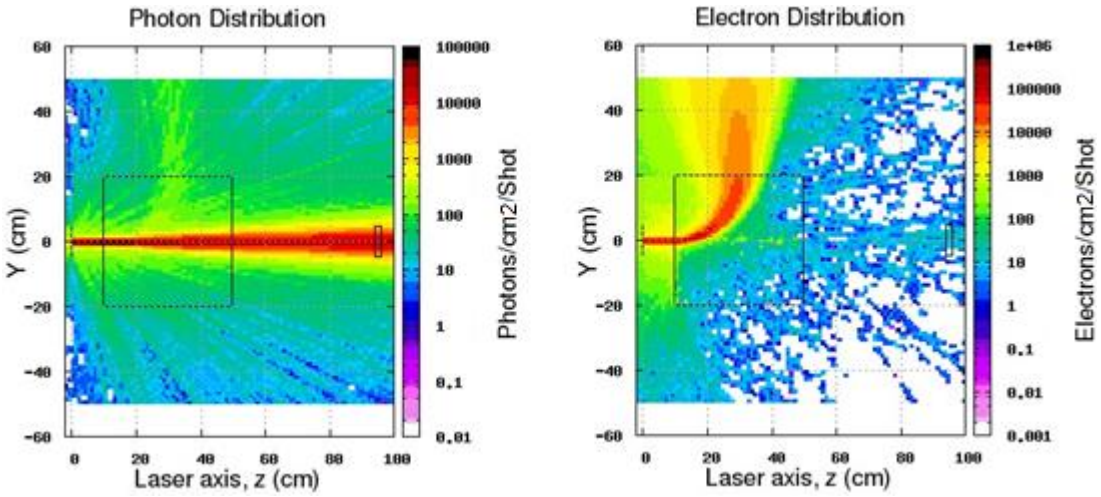

Figure 5.11. Left: USRBIN 3D colour plot showing the bremsstrahlung photon distribution in the simulation geometry. Right: same as the left picture, but this time the electrons are scored. It can be seen the electrons being bent away by the magnetic field. The number of electrons reaching the detector is negligible.

This is the main reason why several cycles are required to simulate correctly a Normal distribution and then sum up and average the results. Five cycles

have been undertaken to obtain all the simulation results shown in this section, apart from the energy spectra, for which 10 cycles have been undertaken. 20,000 primary particles (electrons) are simulated each cycle.

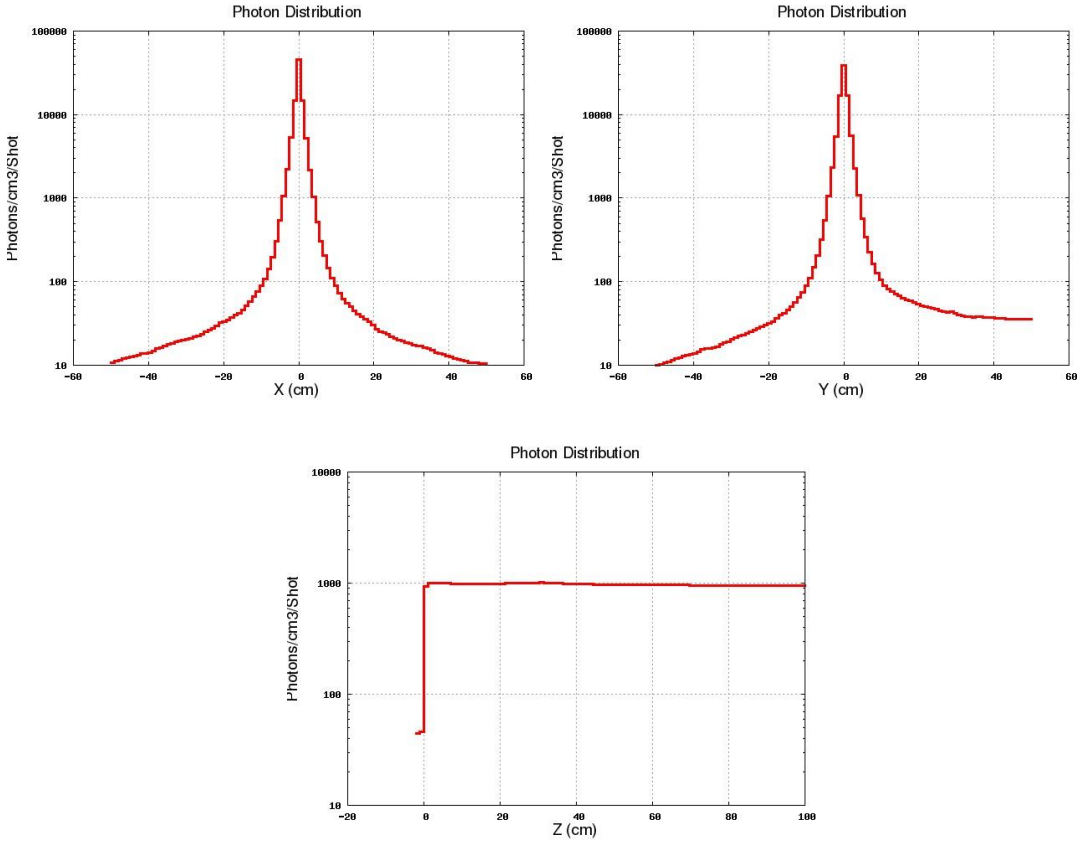

Figure 5.12. Simulated X-ray photon distributions in the Z axis (longitudinal axis), Y (horizontal axis) and X axis (vertical axis). All the simulations have been performed using 20,000 primary particles and 10 cycles. The coordinate (0, 0, 0) represents the centre of the copper target.

The photon fluence (photons/cm^2/shot) was estimated with the USRBIN score, which uses a uniform spatial mesh that is independent of geometry (binning). USRBIN results are presented in Figure 5.11, which shows two colour plots, one for the electrons produced during the interaction of the main electron beam with the converter and one for the X-ray beam produced. It can be seen that the amount of electrons reaching the detector is negligible. These secondary electrons are produced by the interaction of the bremsstrahlung photons with air. This has been checked by running the same simulation substituting the air for vacuum in the geometry. By doing this, the number of electrons reaching the detector is observed to be zero.

Figure 5.12 shows the simulated photon distribution in the X (vertical axis), Y (horizontal axis) and Z axis (longitudinal and laser axis).

The bremsstrahlung radiation divergence is estimated by taking a cross-section of the beam at 80 cm from the converter. Similar to the divergence estimation performed in Chapter 4, the cross-section is fitted to equation (4.14) and the beam waist obtained from the fit (see Figure 5.13). Equation 4.2 is then used to estimate the half-angle divergence. This is done for both x and y axes. The half-angle divergences obtained are 35.7 mrads for the x axis and 34.5 mrad for the y axis.

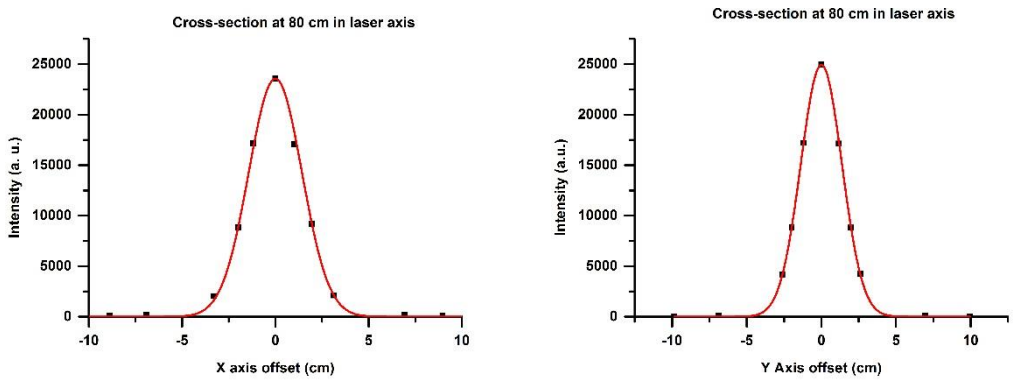

Figure 5.13. Simulated bremsstrahlung cross-sections for both x and y axes at 80 cm along the laser axis z, respectively. The simulated divergence has been calculated from the fits.

The fluence averaged over the volume of the detector geometry region is calculated using the USRTRACK option. This is a “track-length estimator”, which estimates the fluence as volume density of particle trajectory lengths. The simulated X-ray energy spectrum can be seen in Figure 5.14.

As expected, by energy conservation, the energy of the photons emitted extends up to around 120 MeV, which corresponds to electrons that lose all their energy in successive interactions within the converter. From the energy spectrum it is possible to estimate the total number of photons per laser shot according to the simulation. This is done by integrating the energy spectrum over the whole energy range. The result of the integration yields a total number of 7.5×10^{6} photons/shot.

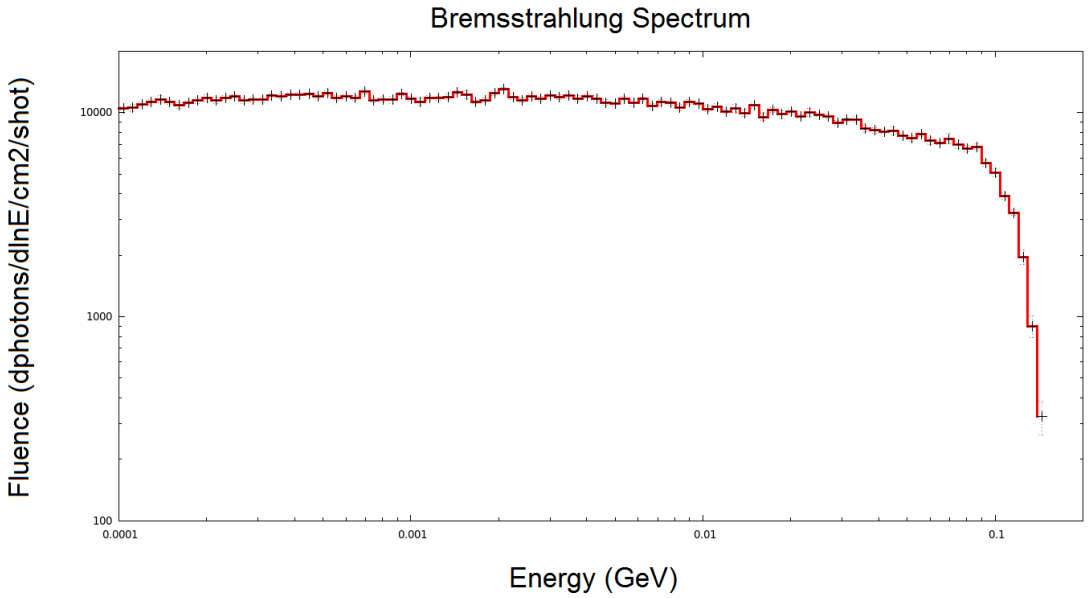

Figure 5.14. Simulated X-ray spectrum of the bremsstrahlung radiation produced. Both x and y axes are in logarithmic scale. Spectrum simulated using the USRTRACK Fluka card which calculates fluence as a function of energy. Results are normalised to the number of electrons per laser shot hitting the Cu converter.

5.5 Experimental results and analysis

A total number of 72 projections have been recorded. The total number of laser shots per projection is 200. The laser repetition rate for this experiment is 0.5 Hz. This gives a total irradiation time per projection of around 7 minutes. Two background measurements are recorded, corresponding to 200 laser shots on an imaging plate without the object in position. One background measurement is performed before recording the projections and one after all the projections have been recorded.

Each imaging plate is scanned immediately after irradiation to avoid excessive fading. The imaging plates are wrapped in Al foil to avoid exposure to ambient light (which could erase the projection recorded on the imaging plate). Most of the analysis is performed using imageJ [19].

Figure 5.16 shows example images of raw recorded projections (without post-processing). The lead hexagon can be clearly seen. Also, in most of the projections the aluminium rod that holds the hexagon to the rotator can be seen, as well as the cap of a screw that helps to hold the hexagon in position. The projections look very similar due to the simplicity of the object. It can also

be seen that the image quality of some projections is higher than others. This is due to instabilities in the electron beam produced, which is due to instabilities in the laser-gas jet system, which are very common in LWFAs.

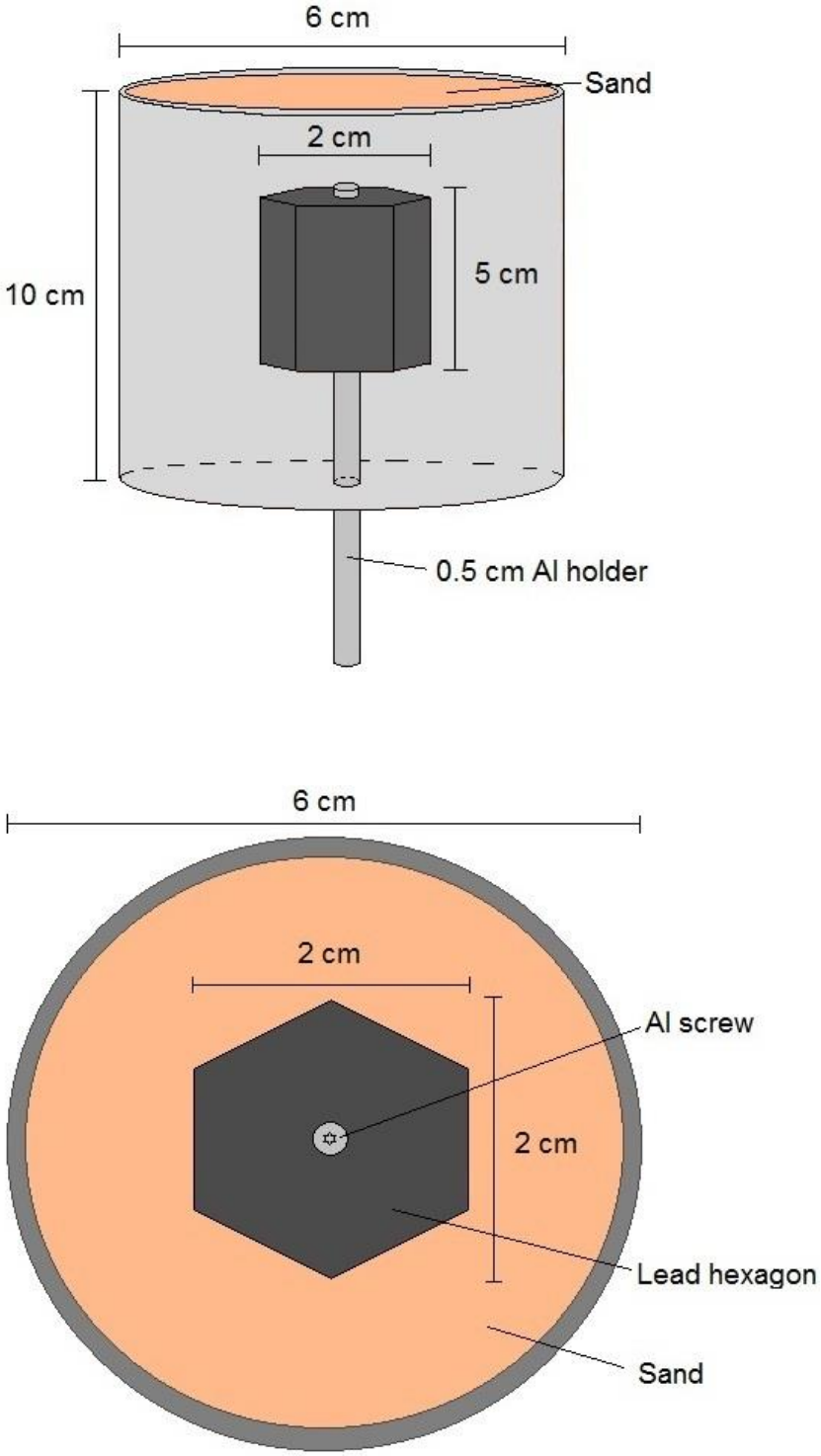

Figure 5.15. Top: lateral view of the lead hexagon inside the sand container. Bottom: top view of the lead hexagon inside the sand container.

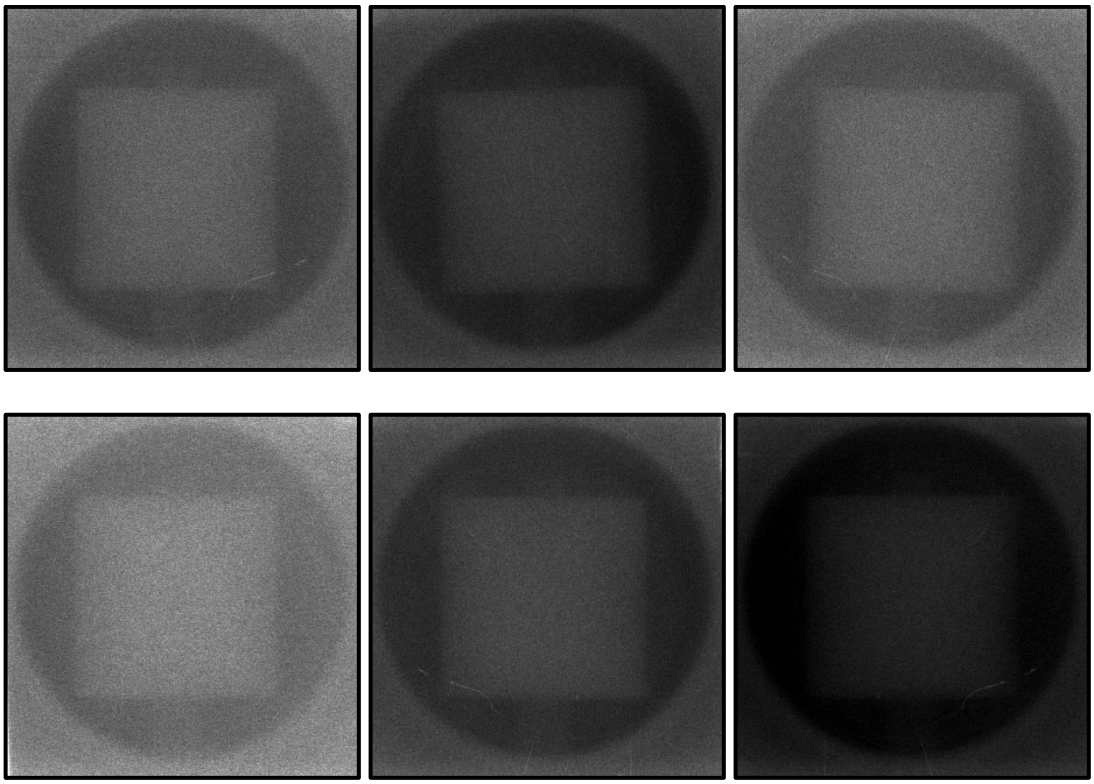

Figure 5.16. Raw projections examples recorded on the imaging plates during the experiment.

Although the imaging plates are always in the same position and orientation in the beam line (as previously mentioned, thanks to a slit designed for this purpose) they are not always read in the same position in the imaging plate scanner. The reading of each imaging plate is performed without any ambient light (and therefore in absolute darkness). Because of this, the scanned images corresponding to each projection appear slightly rotated.

This rotation was corrected using an imageJ template matching plugin described in detail in the following PhD thesis [20]. This plugin looks for a landmark (which in our case is the hexagon) or the most similar pattern in every image of the stack. Then it moves each image so that the landmark pattern will be exactly in the same position throughout the whole image stack.

The template matching method used was the normalised cross-correlation. In this method for each pixel of the image, the normalised cross-correlation coefficient (NCCC) between the landmark and the pixels in the image of interest is calculated. A perfect match would give a NCCC value of +1 while a

comparison with an entirely unrelated landmark gives a NCCC of 0. If the NCCC is equal to -1 this would mean a perfect match but with inverted grayscale values.

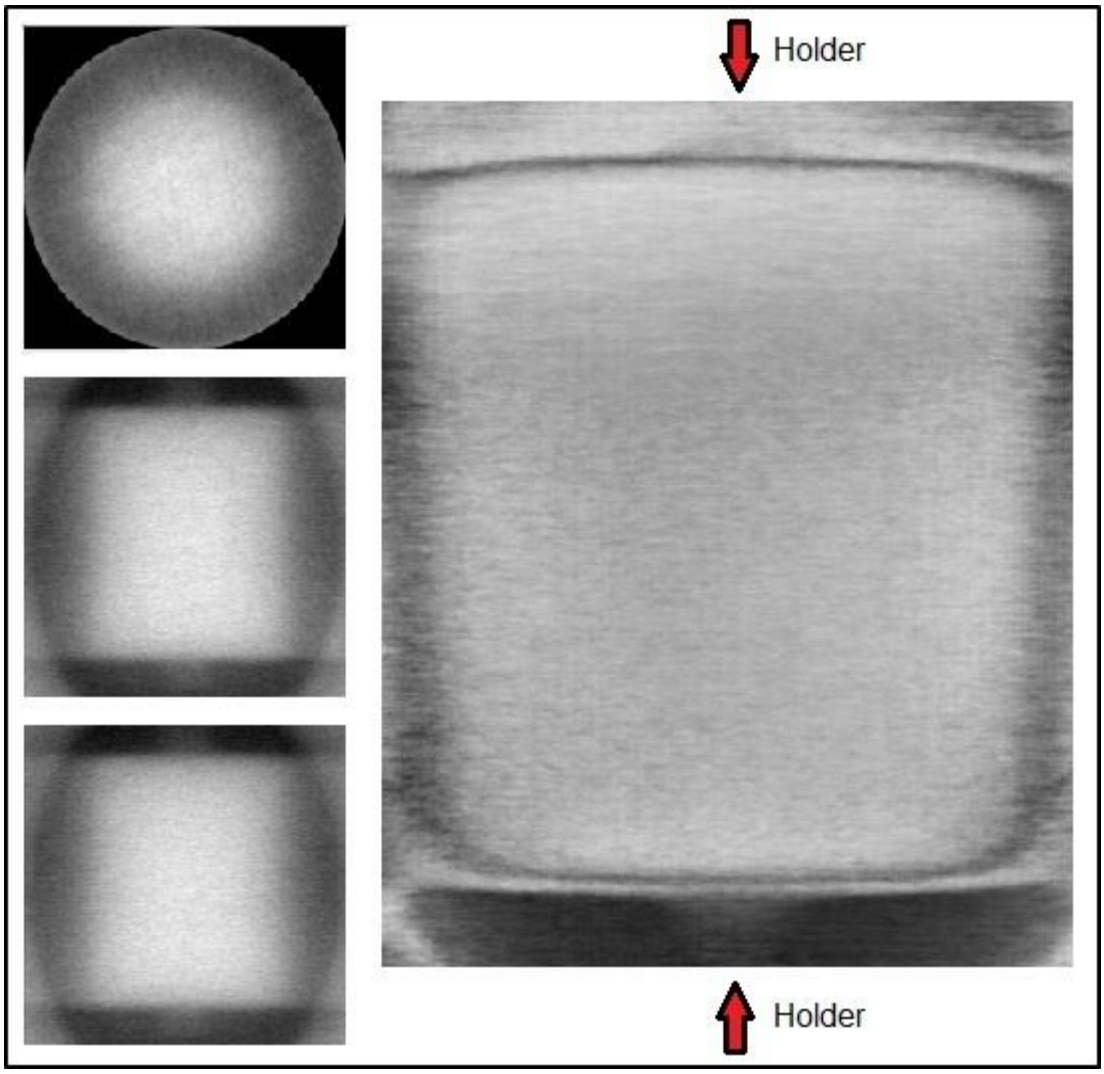

Figure 5.17. LHS: example of a transverse, coronal and sagittal slices similarly to what is obtain in a CT scan. RHS: 3D volume reconstruction from the slices on the lhs.

Since it is a normalised correlation the NCCC computation corrects for any background image intensity variations and differences in lighting and contrast. The normalisation is performed as usual by subtracting the mean at each step and dividing by the standard deviation.

A first tomography attempt was performed without further analysis (*i.e.* without noise removal). The tomography slices have been performed by Dr Dima Maneuski using an in house developed software based on the filtered back

projection method [21]. The 3D reconstruction is performed using the imageJ plugin 3D volume viewer. The results can be seen in Figure 5.17. A total number of 660 slices in the transverse plane have been obtained. Although the quality of the images is not very high, the three main objects can be distinguished: the lead hexagon and the two aluminium holders.

The flat field correction technique is used to obtain a better image quality and a better reconstruction. Two flat field images without object were taken during the experiment. One before starting recording projections and another one just after finishing recording projections.

Two sample projections with flat field correction applied are shown in the following figure:

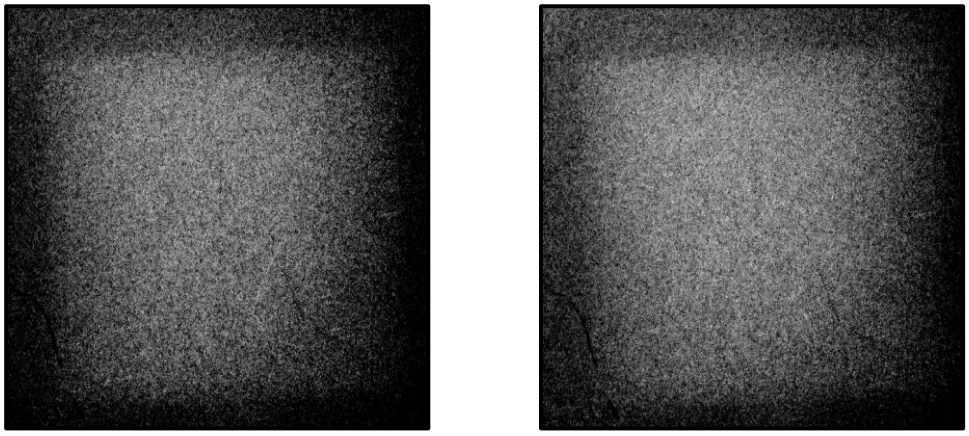

Figure 5.18. Example of two projections after using the flat field correction technique.

It can be seen that the quality of the images is very poor after the correction. This is mainly due to instabilities in the laser-gas jet system which affect the reproducibility of the electron beam and therefore the X-ray bremsstrahlung source. As mentioned in Chapter 4, this technique relies strongly on the stability of the X-ray source.

A better result is obtained using the Fourier method. In this method, filters are used to eliminate the blurring that appears when back-projecting the data.

As the name implies, this method uses fast Fourier transforms (FFTs). Initially, the data is transformed from the spatial domain to the frequency domain, which can be expressed as:

$$F(v_x, v_y) = Ff(x, y), \tag{5.11}$$

where $F(v_x, v_y)$ is the Fourier transform of $f(x, y)$ and F denotes the Fourier transformation.

After this, a filter $H(v)$ is applied in the frequency domain:

$$F'(v) = H(v) \cdot F(v), \tag{5.12}$$

where $F'(v)$ is the filtered projection in the frequency domain.

Finally, to obtain the filtered projections the inverse Fourier transformation (IFFT) is applied to return to the spatial domain.

The following Figure shows an example of this method applied to one of the data projections:

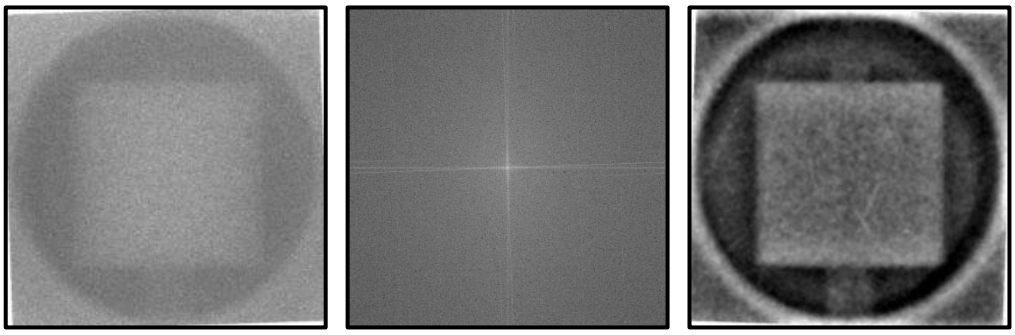

Figure 5.19. LHS: raw projection without filtering. Centre: FFT of lhs image. RHS: result after filtering and IFFT applied.

The improvement in image quality is evident. A significant amount of noise has been removed from the projection and the object edges are sharper.

The Fourier method is applied to all the projections acquired during the experimental run. This analysis was carried out using imageJ. It provides both FFT functions and the bandpass filter required. A short macro has been written to make the process automatic. The imageJ macro applies an FFT to each projection. After this, it applies a band-pass filter and finally an IFFT. The macro accumulates all the projections in an imageJ stack.

A tomographic reconstruction has been performed after filtering the projections using the Fourier method. This second tomography reconstruction has been performed by Dr Dima Maneuski using the same in-house developed software

based on the filtered back projection method discussed in Chapter 4 section 4.4.6. The 3D reconstruction was performed using the imageJ plugin 3D volume viewer. The results can be seen in Figure 5.20.

A total of 660 slices in the transverse plane are obtained and the quality of the slices is enhanced and the objects are clearer.

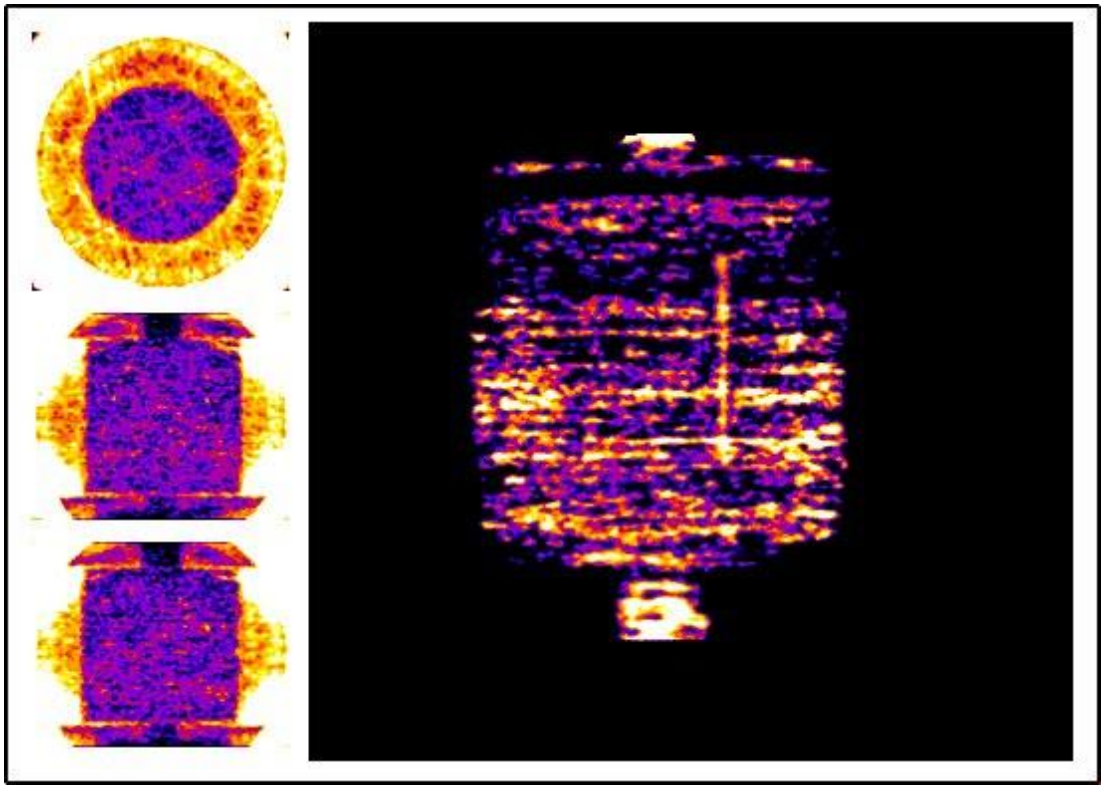

Figure 5.20. LHS: example of a transverse, coronal and sagittal slices similarly to what is obtain in a CT scan. RHS: 3D volume reconstruction from the slices on the left hand side. Fourier method has been applied to remove part of the noise.

5.6 Conclusions and summary of results

The tuneability of the LWFA bremsstrahlung source has been previously demonstrated [12] and in this chapter we have demonstrated the use of the bremsstrahlung source from a LWFA for tomographic applications. This makes the LWFA bremsstrahlung source very attractive not only for imaging applications but for probing dense matter or radioisotope production.

The results presented in this chapter are encouraging and as far as the author is concerned a LWFA has never been used for bremsstrahlung tomographic applications. Therefore, these results are a proof-of-principle of the application of LWFA technology to this kind of bremsstrahlung tomography.

The setup is simple and similar to what would be required for other LWFA applications such as radioisotope production, or even for imaging using the betatron X-ray source. This flexibility together with its table-top size makes the LWFA an attractive multi-application technology.

On the negative side, there is scope for improvement in both the quality of the projections and the tomography reconstruction. The hexagonal shape of the prism is not distinguishable in the projections or in the 3D reconstruction which shows a cylindrical shape. The main reason for this is that the difference in attenuation is not large enough to reconstruct a hexagonal shape. The use of imaging plates is also a problem, because the granularity of this detector creates many artefacts in the reconstruction.

The following factors affected the quality of the tomography reconstruction:

1. The number of projections: the number of projections taken during this experimental run was 72. The number of projections depends on the application. Normally, the number of projections taken varies between 120 and 150, depending on the complexity of the object to be scanned. For some industrial applications for which the dose is not an issue (as it is in medical imaging) the total number of projections can be thousands [22].
2. Imaging plates: This detector is not ideal for several reasons. The granularity of the imaging plates affects the quality of the images obtained. Moreover, it is a very time consuming detector since imaging plates have to be scanned, replaced and cleaned after each measurement is taken.
3. Instabilities of the laser-gas jet system: small variations in the laser-gas jet system lead to variations in the electron beam stability, which affect

the bremsstrahlung source. Another issue is the repetition rate of this technology. In the case of the ALPHA-X system the maximum repetition rate is currently 1 Hz (accelerator repetition rate) making these applications time consuming. This can be extended to 10 Hz with the current laser. However, the development of kilohertz lasers and gas jet systems will help to overcome these issues.

In this experiment, we have demonstrated that it is possible to obtain tomography reconstruction of objects inside sand containers, which is a useful tool for radioactive material inspection as previously mentioned. However, there are other industrial applications that could benefit from laser-driven bremsstrahlung tomographic imaging [23].

Manufacturers are starting to use computerised CT scanning for material inspection and to inspect the interior of microparts. For this purpose, currently X-ray tubes take thousands of projections by rotating the object to inspect, which is similar to the experiments described in this Chapter.

If the objective is to inspect low density materials, an X-ray tube is sufficient for this purpose. However, scanning denser materials requires higher photon energy. If the object to be scanned is made of materials such as steel, iron or copper, higher energy X-rays than those produced in an X-ray tube will be an advantage.

This is where the LWFA can make a difference compared with conventional X-ray sources. Another advantage is the tuneability of the electron beam energy, which enables a flexible X-ray beam to be produced and allows optimisation for each particular application.

Chapter references:

1. Cipiccia, S., et al., *A tuneable ultra-compact high-power, ultra-short pulsed, bright gamma-ray source based on bremsstrahlung radiation*

from laser-plasma accelerated electrons. Journal of Applied Physics, 2012. **111**(6): p. 063302.

2. Edwards, R.D., et al., *Characterization of a gamma-ray source based on a laser-plasma accelerator with applications to radiography.* Applied Physics Letters, 2002. **80**(12): p. 2129-2131.
3. Giulietti, A., et al., *Intense X-Ray Source in the Giant-Dipole-Resonance Range Driven by 10-TW Laser Pulses.* Physical Review Letters, 2008. **101**(10): p. 105002.
4. Glinec, Y., et al., *High-Resolution X-Ray Radiography Produced by a Laser-Plasma Driven Electron Source.* Physical Review Letters, 2005. **94**(2): p. 025003.
5. Ben-Ismaïl, A., et al., *Compact and high-quality gamma-ray source applied to 10 μm-range resolution radiography.* Applied Physics Letters, 2011. **98**(26): p. 264101.
6. Wu, Y., et al., *Laser wakefield electron acceleration for γ-ray radiography application.* Chinese Optics Letters, 2012. **10**(6): p. 063501.
7. Galy, J., et al., *Bremsstrahlung production with high-intensity laser matter interactions and applications.* New Journal of Physics, 2007. **9**(2): p. 23.
8. Jackson, J.D., *Classical Electrodynamics (John Wiley, 1999).*
9. http://pdg.lbl.gov/2009/AtomicNuclearProperties/
10. Koch, H. and J. Motz, *Bremsstrahlung cross-section formulas and related data.* Reviews of Modern Physics, 1959. **31**(4): p. 920.
11. Cipiccia, S., *Compact Gamma-ray Sources Based on Laser-Plasma Wakefield Accelerator.* Ph.D. thesis, University of Strathclyde.
12. Agostinelli, S., et al., *Geant4—a simulation toolkit.* Nuclear instruments and methods in physics research section A: Accelerators, Spectrometers, Detectors and Associated Equipment, 2003. **506**(3): p. 250-303.
13. Ben-Ismaïl, A., J. Faure, and V. Malka, *Optimization of gamma-ray beams produced by a laser-plasma accelerator.* Nuclear Instruments

and Methods in Physics Research Section A: Accelerators, Spectrometers, Detectors and Associated Equipment, 2011. **629**(1): p. 382-386.

14. http://madx.web.cern.ch/madx/
15. Fiksel, G., et al., *Note: Spatial resolution of Fuji BAS-TR and BAS-SR imaging plates.* Review of Scientific Instruments, 2012. **83**(8): p. 086103.
16. Ferrari, A., et al., *FLUKA: A multi-particle transport code (Program version 2005)*. 2005.
17. Böhlen, T.T., et al., *The FLUKA Code: Developments and Challenges for High Energy and Medical Applications.* Nuclear Data Sheets, 2014. **120**(0): p. 211-214.
18. Vlachoudis, V. *FLAIR: a powerful but user friendly graphical interface for FLUKA*.
19. Schneider, C.A., W.S. Rasband, and K.W. Eliceiri, *NIH Image to ImageJ: 25 years of image analysis.* Nature Methods, 2012. **9**(7): p. 671-675.
20. Tseng, Q., *Study of multicellular architecture with controlled microenvironment. PhD thesis.* Universite de Grenoble, 2011.
21. Claus, B.E.H. and J.W. Eberhard, *Generalized filtered back-projection reconstruction in digital tomosynthesis*. 2004, Google Patents.
22. Flisch, A., et al., *Industrial computed tomography in reverse engineering applications.* DGZ-fP-Proceedings BB, 1999. **4**(7): p. 45-53.
23. Hofmann, J., A. Flisch, and A. Obrist, *Adaptive CT scanning—mesh based optimisation methods for industrial X-ray computed tomography applications.* NDT & E International, 2004. **37**(4): p. 271-278.

Chapter 6: Summary of results and outlook

6.1 Summary of results

The aim of this work has been to study the potential use of laser-driven X-ray sources for imaging-related applications. For this purpose, the betatron X-ray source of the ALPHA-X laboratory has been characterised in terms of energy spectrum, photon flux and divergence.

The energy spectrum has been characterised for different plasma densities showing the fine tuneability of the betatron X-rays with the plasma density. A second measurement of the critical energy has been undertaken using metal filters that show a good agreement with the results given by Timepix. The divergence and the spatial distribution of the betatron X-rays has been measured using imaging plates. An easy setup method for X-ray polarisation measurements has also been shown simply by using a semiconductor pixel detector, i.e. Timepix, and further polarisation-related experiments are suggested.

Following this characterisation, a set of experiments to explore the potential of laser-driven X-ray sources for imaging applications have been performed. Concretely, it is shown the potential of the ALPHA-X betatron X-rays to be an interesting source for phase-contrast imaging applications such as biological specimens imaging, microscopy and tomographic studies.

In the discussion section of Chapter 4, a set of Monte Carlo simulations evaluating the requirements of the X-ray source for the application of bone crack imaging have been performed and concluded that a betatron X-ray source of 50 keV critical energy would be possible for imaging micro-cracks in bones with a resolution of around 1 μm.

Furthermore, the potential of the ALPHA-X laser-driven bremsstrahlung source for conventional absorption tomographic imaging has been demonstrated. A laser-driven bremsstrahlung source may find useful industrial applications such as security and cargo inspection and radioactive waste container

inspection. Medical applications such as radiosurgery or radioisotope production have also been suggested [1].

6.2 LWFA for real-world clinical imaging applications: outlook and discussion

The use of X-rays in science, technology and for society is very widespread. The list of fields and applications is large and diverse: biology, material science, security, palaeontology, etc. The development of XPCi in the last decade has shown the potential of this technique to change the way X-ray imaging is performed nowadays.

Clinically, a change from conventional absorption imaging to XPCi would have a huge impact on the life expectancy of patients. Diagnosis of diseases such as cancer would be made earlier. Also, absorption imaging is not suitable for some cancers because of the lack of contrast, which would be avoided with the implementation of XPCi techniques. This would lead to a reduction in the mortality rate in addition to increasing the life expectancy and patient quality of life. Impressive results have already been achieved in breast imaging using synchrotron radiation [2].

However, in a clinical environment, X-rays are not only used for diagnosis, they are used on a daily basis in other specialities such as in treatment planning. When a patient is diagnosed with cancer he/she normally undergoes a CT scan of the site where the cancer has been diagnosed. The images acquired from this scan is used by the responsible clinician (together with other diagnostic tools) to outline the volumes that will be targeted with external radiotherapy. Sometimes the lack of contrast makes this outlining process difficult. For instance, in the particular case of early prostate cancer, the clinical target volume (CTV) outlined by the clinician will be the entire prostate and seminal vesicles. The organs at risk (OARs) that need to be spared as much as possible are the bladder and rectum. However, since the differences in material density between prostate and bladder are small, in some cases it is difficult to distinguish where the bladder ends and where the prostate starts or

vice versa. XPCi would help to define the edges between these organs more clearly making the outline process easier for clinicians in addition to increasing the treatment volume accuracy while reducing the dose the OARs receive.

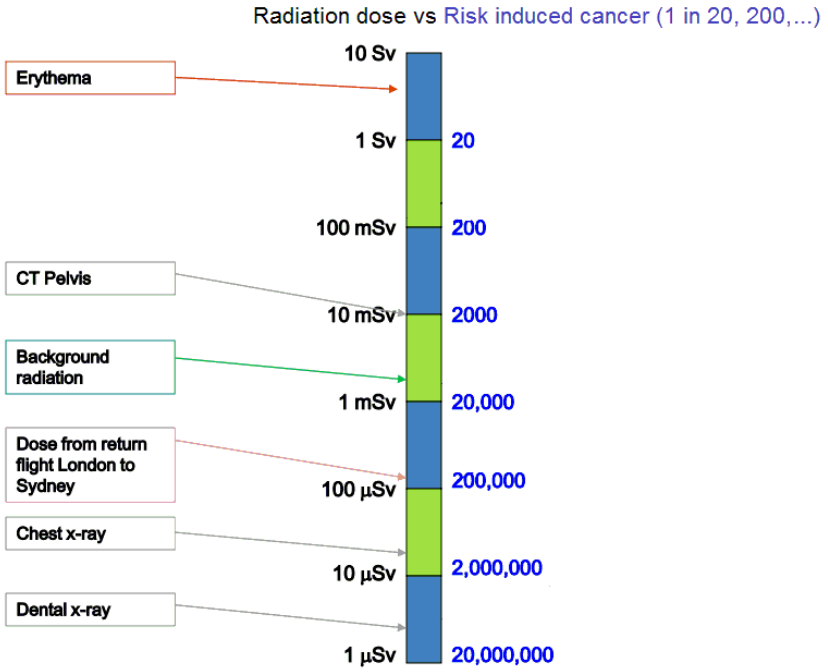

Figure 6.1. Radiation dose received by a member of the public together with the risk of induced cancer. From [3].

Another important fact is the lower dose required to achieve good contrast when using XPCi in comparison with absorption imaging. As discussed in chapter 4 (Figure 4.1) it can be seen that for certain materials and energy the dose required to achieve a similar contrast can be up to 4 orders of magnitude lower in XPCi than in conventional absorption imaging. This has important implications in term of radiation protection and radiation risks. Although the risk is low and the diagnostic benefits clearly overcome the radiation risks involved, there is increased concern in the amount of diagnostic X-ray tests being performed, and the proportion of cancer induction of those tests. Figure 6.1 gives a summary with an estimation of the risk of dying from cancer induced by different radiation exposure common situations.

The numbers increase if children are involved since they are more sensitive to radiation than adults plus the fact that the CT scan settings tend to remain similar independently of whether an adult or child is being scanned. There have

been long term studies assessing these risks [4, 5]. An XPCi based CT scan would significantly reduce these Figures. Even if the dose reduction was only of one order magnitude, the number of cancer cases induced by scans would be significantly reduced.

Many technical and engineering challenges need to be overcome before XPCi can be used in a clinical environment. As shown in this work, free space propagation XPCi is an ideal candidate because it avoids expensive optical elements. However, the current state-of-the-art X-ray sources prevents this from clinical implementation. Therefore, the research and development of new and innovative X-ray sources, such as those based on LWFA, are required for clinical XPCi.

Although the progress in LWFA technology in the last decade has been huge, in reality, the current state of this technology only allows the use of plasma accelerators for small imaging applications [6-8]. The development of the LWFA has always been linked to progress of high power laser technology. A decade ago only a few research groups in the world had access to tens of TW laser systems. Today, table-top high power lasers systems of hundreds of TW are becoming more and more available and this progress is expected to continue in the next decades.

The key parameter that needs be improved significantly in order to use LWFA for the above-mentioned potential applications is the repetition rate. At the moment, the state of the art laser plasma accelerators work at a repetition rate between 0.03 and 1 Hz even though 10 Hz laser systems are currently available. This limitation comes from the inability of the current turbo vacuum pumps to keep the interaction chamber under vacuum at high repetition rates in addition to the compressor gratings that currently cannot support very high repetition rates without being damaged.

As an example, this repetition rate is several orders of magnitude smaller than the repetition rate achieved by third-generation light sources. It is clear that increasing the repetition rate from 1 Hz to the kHz range is not a trivial task,

and will require significant engineering and development effort in the photonics and laser physics fields.

The following question that arises is: assuming all the technical challenges are overcome and both the repetition rate and the reliability of laser plasma acceleration scale to the required standards for clinical imaging applications, are the benefits big enough to completely change the procedures and the way X-ray imaging is done in current clinical environments? In the authors opinion the answer is yes because of the wide variety of applications that could be done.

It does not seem very efficient to install a LWFA only for medical imaging applications in a clinical environment, especially with the development of other technologies such as the MR-Linac [9] or even the edge illumination technique [10] for XPCi.

But the strong point of the LWFA is the incredible amount of applications that could be done using a high power laser. Laser plasma accelerators could potentially provide all kinds of treatment modality for radiation therapy together with all the imaging applications. These include conventional and very high energy electron beams, conventional flattened and non-flattened flattening filter free bremsstrahlung photons and even proton and heavy ion beam therapy [11]. The production of medical radioisotopes using the LWFA is also currently under development [12] and the scalability in the repetition rate of the laser plasma accelerators will take this medical application several steps further.

Financially speaking, a small size radiotherapy department will have around 4 medical Linacs and probably a dedicated CT scanner. A state of the art Varian Truebeam costs around £2.1 million [13]. The price of a conventional CT scanner varies but this can be £0.1 million on average. This would make a total of around £9 million. A state of the art high power laser costs around £2 million pounds. Since laser beams are transported using optics, a single laser system could be used to deliver radiotherapy in several bunkers in the same way as

several target areas share the same laser in state-of-the-art high-power laser facilities such as the Vulcan or Astra-Gemini lasers at the RAL and SCAPA at Strathclyde. Moreover, betatron X-rays could be used in the same way as a CT scanner with improved contrast due to XPCi. Assuming that, in a more realistic scenario, two independent laser systems would be required (in order to have a back-up laser system so the clinical service is not interrupted in case one of the laser system develops a problem) this would make a total of £4 million, £5 million less than 4 medical linacs and a CT scanner together with a bigger variety of applications and treatment modalities. Moreover, scaling up the requirement of such laser systems will reduce their production costs.

To conclude, the development of high power laser systems working at very high repetition rates will soon allow the construction of research laboratories capable of producing bright compact X-ray sources useful for real imaging applications which could potentially be translated to a hospital clinical setting. At the moment, the most promising alternative to large conventional accelerators is the LWFA. Although the technical and engineering challenges are still huge, the increasing demand of this table-top compact radiation sources for every day applications represent a vast scope for future research in this interesting field.

Chapter references:

1. Cipiccia, S., *Compact Gamma-ray Sources Based on Laser- Plasma Wakefield Accelerator.* Ph.D. thesis, University of Strathclyde.
2. Castelli, E., et al., *Clinical mammography at the SYRMEP beam line.* Nuclear Instruments and Methods in Physics Research Section A: Accelerators, Spectrometers, Detectors and Associated Equipment, 2007. **572**(1): p. 237-240.
3. *www.bcu.wales.nhs.uk/*
4. Brenner, D., et al., *Estimated risks of radiation-induced fatal cancer from pediatric CT.* AJR Am J Roentgenol, 2001. **176**(2): p. 289-96.

5. Pearce, M.S., et al., *Radiation exposure from CT scans in childhood and subsequent risk of leukaemia and brain tumours: a retrospective cohort study.* The Lancet. **380**(9840): p. 499-505.
6. Cole, J., et al., *Tomography of human trabecular bone with a laser-wakefield driven x-ray source.* Plasma Physics and Controlled Fusion, 2015. **58**(1): p. 014008.
7. Wenz, J., et al., *Quantitative X-ray phase-contrast microtomography from a compact laser-driven betatron source.* Nature Communications, 2015. **6**.
8. Ben-Ismaïl, A., et al., *Compact and high-quality gamma-ray source applied to 10 µm-range resolution radiography.* Applied Physics Letters, 2011. **98**(26): p. 264101.
9. www.royalmarsden.nhs.uk
10. Olivo, A. and R. Speller, *A coded-aperture technique allowing x-ray phase contrast imaging with conventional sources.* Applied Physics Letters, 2007. **91**(7): p. 074106.
11. Subiel, A., *Feasibility Studies on the Application of Relativistic Electron Beams from a Laser Plasma Wakefield Accelerator in Radiotherapy.* Ph.D. thesis, University of Strathclyde, 2014.
12. Leemans, W., et al. *Radio-isotope production using laser Wakefield accelerators*. in *Particle Accelerator Conference, 2001. PAC 2001. Proceedings of the 2001*. 2001. IEEE.
13. www.varian.com/en-gb/oncology/products/treatmendelivery/truebeam-radiotherapy-system